CHEMICAL REVIEWS

pubs.acs.org/CR Review

Advances in Bioresorbable Materials and Electronics

Published as part of the Chemical Reviews "Wearable Devices".

Yamin Zhang,[#] Geumbee Lee,[#] Shuo Li,[#] Ziying Hu,[#] Kaiyu Zhao, and John A. Rogers*

Cite This: https://doi.org/10.1021/acs.chemrev.3c00408 Read Online

ACCESS | Metrics & More | Article Recommendations

ABSTRACT: Transient electronic systems represent an emerging class of technology that is defined by an ability to fully or partially dissolve, disintegrate, or otherwise disappear at controlled rates or triggered times through engineered chemical or physical processes after a required period of operation. This review highlights recent advances in materials chemistry that serve as the foundations for a subclass of transient electronics, bioresorbable electronics, that is characterized by an ability to resorb (or, equivalently, to absorb) in a biological environment. The primary use cases are in systems designed to insert into the human body, to provide sensing and/or therapeutic functions for timeframes aligned with natural biological processes. Mechanisms of bioresorption then harmlessly eliminate the devices, and their associated load on and risk to the patient, without the need of secondary removal surgeries. The core content focuses on the chemistry of the enabling electronic materials, spanning organic and inorganic compounds to hybrids and composites, along with their mechanisms of chemical reaction in biological environments. Following discussions highlight the use of these materials in bioresorbable electronic components, sensors, power supplies, and in integrated diagnostic and therapeutic systems formed using specialized methods for fabrication and assembly. A concluding section summarizes opportunities for future research.

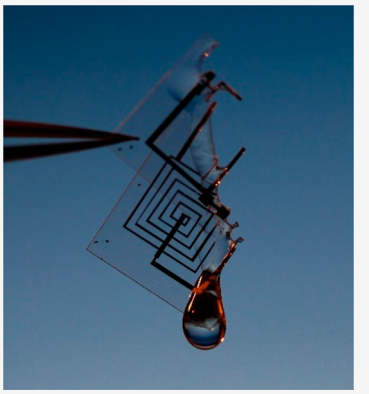

CONTENTS

Received: June 16, 2023

https://doi.org/10.1021/acs.chemrev.3c00408
Chem. Rev. XXXX, XXX, XXX−XXX

1. INTRODUCTION

Transient electronics represents an emerging class of technology with a range of unique and important applications.[1−4] Unlike conventional electronic systems, where the engineering emphasis is on long-term operational and physical stability, transient devices consider the opposite goal, via constituent materials that fully or partially dissolve, resorb, or otherwise physically disappear through chemical or physical processes at programmed rates or at triggered times after a defined period of operation. Uses of this type of technology complement those of traditional electronics, for applications in environmentally degradable consumer gadgetry or monitors/sensors that reduce solid waste streams, in hardware-oriented secure platforms that remove sensitive information in military or proprietary industrial systems, and in bioresorbable medical electronics that eliminate surgical extraction procedures needed for temporary implants.[3,5]

Bioresorbable electronics is one of the most compelling areas of opportunity, wherein bioresorbable (or, equivalently, bioabsorbable) materials react in a controlled manner with a surrounding biological environment through a range of possible metabolic (i.e., enzymatic), hydrolytic or other processes, sometimes in parallel with mechanisms of physical disintegration or fragmentation.[6−8] The term biodegradable indicates an ability for chemical bonds to break naturally in the environment (ecoresorbable) or in the body (bioresorbable). This review article focuses on bioresorbable examples of reported biodegradable electronics. For temporary implants used with human patients, the body absorbs, metabolizes and/or discharges the biocompatible end products without adverse responses or side effects. The result eliminates associated costs and risks of pain, infection, or immune responses associated with secondary surgeries that would otherwise be required for device removal.[9−11]

Bioresorbable mechanical devices such as sutures,[12] stents,[13] scaffolds,[14] and release vehicles for drug delivery[15] have long, successful histories of clinical use. These technologies establish the broad value of nonelectronic implantable technologies that do not require surgical removal. Bioresorbable electronic functionality qualitatively expands the range of possibilities. The first examples of such types of devices involved ultrathin transistors and logic gates embedded in films of silk fibroin, as partially resorbable systems that incorporate semiconductor components.[10] Subsequent research defined broad classes of bioresorbable materials for conductors,[16,17] semiconductors,[18,19] and insulators,[20,21] as the basis for advanced, integrated systems with wide ranging diagnostic and therapeutic functions.[22−24] Combining such platforms with wearable sensors and wireless controllers enables closed-loop, multimodal operation.[25]

This review summarizes advances in materials chemistry that underpin these technologies. The article begins with an overview of bioresorbable inorganic and organic compounds, hybrids, and composites for semiconductors, conductors, and insulators, with an emphasis on their chemistries and mechanisms for reactions in biological environments. Subsequent content summarizes uses of these materials in components, sensors, and power supplies formed from these materials using associated assembly and fabrication techniques. Descriptions include integrated systems that address clinical opportunities in brain and blood monitoring,[9,26] cardiac pacing,[22,27] nerve regeneration,[24,28] pain relief,[11,23] and programmed pharmacological treatment.[29,30] A concluding section summarizes the current state of the field and highlights opportunities for future research.

2. MATERIALS FOR BIORESORBABLE ELECTRONICS

The development of bioresorbable electronic systems begins with a detailed understanding of essential aspects of the chemistry of the constituent materials. Realistic applications involve timeframes dictated by clinical use cases, with different requirements on these materials. The two most important time scales are those associated with the periods of operational stability and of complete bioresorption. In most examples, the former is much shorter (typically days or weeks) than the latter (typically several or many months). An ideal design minimizes these differences, sometimes based on a triggering event that initiates fast bioresorption, but in all cases with biocompatible materials that avoid any adverse reactions within the body at any stage throughout the life of the device. In general, bioresorbable systems consist of functional, supporting (i.e., substrate), and encapsulating components. The permeation of biofluids due to the erosion of the outermost encapsulating layer or permeation through it can lead to degradation of enclosed functional components, ultimately leading to a deterioration of the operational performance. Thus, the degradation kinetics and the permeability of the encapsulating layer, and often also the supporting substrate, are critical factors in determining the functional lifetime of the overall platform, as it is often the rate-determining step.

The rapidly growing literature on bioresorbable electronics uses various forms of nomenclature to describe the materials and their interactions with biological surroundings. In the following, biocompatibility refers to the capability of a material or device to interact with a living system without eliciting harmful responses or reactions. The term bioresorbable is commonly interchangeable with biodegradable and bioabsorbable, as a description of a substance that can be consumed through a series of metabolic (i.e., enzymatic), hydrolytic, or other reactions, sometimes in parallel with mechanisms of physical disintegration or fragmentation, that occur in a biological environment. The terms dissolution or degradation refer generally to these processes. The human body absorbs, metabolizes, and/or discharges the biocompatible end products without any abnormal responses.

The following subsections summarize various advances in the most successful and promising bioresorbable electronic materials, including representative chemistries and reaction kinetics (in solutions that approximate physiological conditions or *in vivo*) associated with both inorganic and organic

https://doi.org/10.1021/acs.chemrev.3c00408
Chem. Rev. XXXX, XXX, XXX−XXX

conductors, semiconductors, and insulators that have demonstrated uses in fully or partly bioresorbable devices and electronic systems.

2.1. Bioresorbable Conductors

2.1.1. Inorganic Conductors. The main options include alkali-earth (e.g., magnesium [Mg], calcium [Ca]) and transition metals (e.g., molybdenum [Mo], tungsten [W], zinc [Zn], iron [Fe]), and alloys of these materials (e.g., AZ31B; Mg-based alloy) in the form of thin films (tens to hundreds of nanometers), foils (tens of micrometers), particles (micrometers), wires (tens of micrometers), or their composites with bioresorbable polymers. The degradation of such metals follows from a series of anodic and cathodic reactions to produce, in general, a complex collection of products.[31−33] Upon immersion in water/biofluids, these metals (M) undergo electrochemical oxidation to generate metal cations (M^{n+}) and electrons (e^-) (i.e., anodic reaction; $M \rightarrow M^{n+} + ne^-$) and other reaction products such as hydroxide ions (OH^-), hydrogen gas (H_2), metal hydroxides ($M(OH)_n$), and/or phosphates (i.e., cathodic reaction) (Figure 1).[31,32] For example, electrons generated via

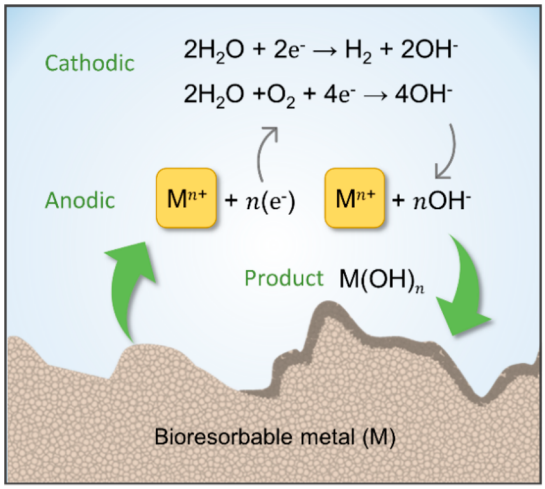

Figure 1. Schematic illustration of chemical reactions associated with dissolution of bioresorbable metals (M) in aqueous environments.[31−33] A series of anodic and cathodic reactions produce hydrogen gas and hydroxide ions. In some cases, solid fragments generated during this process can be absorbed into the body through phagocytosis.

anodic reactions of Mg and Zn participate in water reduction ($2H_2O + 2e^- \rightarrow H_2 + 2OH^-$), resulting in the production of hydrogen gas along with a corresponding metal hydroxide (i.e., $M(OH)_n$), typically as surface layers. Erosion of these layers by chloride or other reactive ions, or by biochemical species in body fluids such as proteins, lipids, and amino acids, leads to continuous dissolution of the underlying metal. By contrast, Fe, Mo, and W produce a related protective layer through the reduction of dissolved oxygen ($2H_2O + O_2 + 4e^- \rightarrow 4OH^-$), without formation of hydrogen gas. A particularly compact layer, consisting mainly of $Fe(OH)_2$, $Fe(OH)_3$, and Fe_2O_4, forms in the case of Fe, which hinders further dissolution of metal, resulting in a slow rate of degradation rate compared to that of the other metals.[32] Fundamental studies indicate that the overall kinetics of these processes depend strongly on the specific properties of the surrounding aqueous solution. The following chemical reactions apply for each material:[34]

$$Mg + 2H_2O \rightarrow Mg(OH)_2 + H_2$$

$$Zn + 2H_2O \rightarrow Zn(OH)_2 + H_2$$

$$2W + 2H_2O + 3O_2 \rightarrow 2H_2WO_4$$

$$2Mo + 2H_2O + 3O_2 \rightarrow 2H_2MoO_4$$

$$4Fe + 3O_2 + 6H_2O \rightarrow 4Fe(OH)_3$$

Thin films of Mg, Zn, Mo, W, and Fe are attractive as electrodes for active or passive electronic components and as interconnects between such components due to their high electrical conductivity (Mg, 2.3×10^7 S m^{-1}; Zn, 1.7×10^7 S m^{-1}; Mo, 2.0×10^7 S m^{-1}; W, 2.0×10^7 S m^{-1}; Fe, 1.0×10^7 S m^{-1} at 20 °C) and relative ease in deposition and processing.[1] Figure 2a,b represent sequences of dissolution of patterned traces of Mg (50 nm thick) and Zn (400 nm thick) immersed in phosphate buffered saline (PBS) at physiological pH (~7.4) and room and body temperature (~37 °C).[35,36] Additional examples are Mo (300 nm thick) and W (100 nm thick) as electrodes for electrochemical capacitors and as interfaces to light-emitting diodes (LEDs) (Figure 2c,d).[16,17] The rates of dissolution of thin films (deposited using electron evaporation to a few tens or hundreds of nanometers in thickness) of Mg, Zn, W, Mo, and Fe are 480, 300, 20, 0.7, and 7 nm day^{-1}, respectively, as evaluated in Hank's Balanced Salt Solution (HBSS) (pH 7.4 at 37 °C).[16,17,37] Similarly, the dissolution of foils (50 μm thick) of Mg, Zn, W, Mo, and Fe as substrates have rates of 4000, 3500, 150, 20, and 5−80 nm day^{-1}, respectively, in PBS (pH 7.4 at 37 °C).[9,38] Figure 4a summarizes dissolution rates of inorganic conductors in various biofluids at physiological conditions (pH 7.4 at 37 °C).

Bioresorbable metal alloys can be exploited in structural implants for orthopedic medical applications (e.g., scaffolds, stents, screws) due to their tunable mechanical properties and degradation rates. As representative examples, bioresorbable Mg-based alloys involve Mg with relatively low content of other metals, such as Ca, Zn, aluminum (Al), lithium (Li), zirconium (Zr), and rare earths (RE) elements; Mg-0.8Ca, AZ31 (Mg-3Al-1Zn), ZX11 (Mg-1Zn-1Ca), ZEK100 (Mg-Zn-RE-Zr), LAE442 (Mg-4Li-4Al-2RE), MgYREZr (MAGNEZIX).[32] In the Mg−Al−Zn alloys (e.g., AZ31, Mg-3Al-1Zn; AZ91, Mg-9Al-1Zn), incorporation of Al contributes to the mechanical strength and the corrosion resistance. These alloys produce insoluble aluminum oxide (i.e., Al_2O_3) as a degradation product, thereby resulting in a reduced degradation rate compared to pure Mg (typically 3 times slower under pH 7.4 PBS at 37 °C).[34,39] High concentrations of Al can, however, cause harmful biological effects and specific diseases (e.g., Alzheimer and dementia). As an application example, Mg−Zn−Ca alloys (Mg-1Zn-5Ca) fixed to the bone as screws completely disappear after 12 months in human evaluations.[40]

Certain applications require printable and/or thick conductive layers, as inks/pastes that consist of micro/nanoparticles of bioresorbable metals dispersed in a matrix of a bioresorbable polymer. Physical contacts between the conductive components in these materials establish percolation networks that support electrically conductive pathways. Well-studied composites include Zn/poly(ethylene oxide) (PEO),[41] Fe/polycaprolactone (PCL),[42] and Mg/polylactic acid (PLA).[43] A disadvantage of these systems is that surface oxides on the metals can increase the contact resistances to reduce the conductivity of the networks. In this context, Mo and W microparticles are attractive alternatives because their relative reactivities, as

https://doi.org/10.1021/acs.chemrev.3c00408
Chem. Rev. XXXX, XXX, XXX−XXX

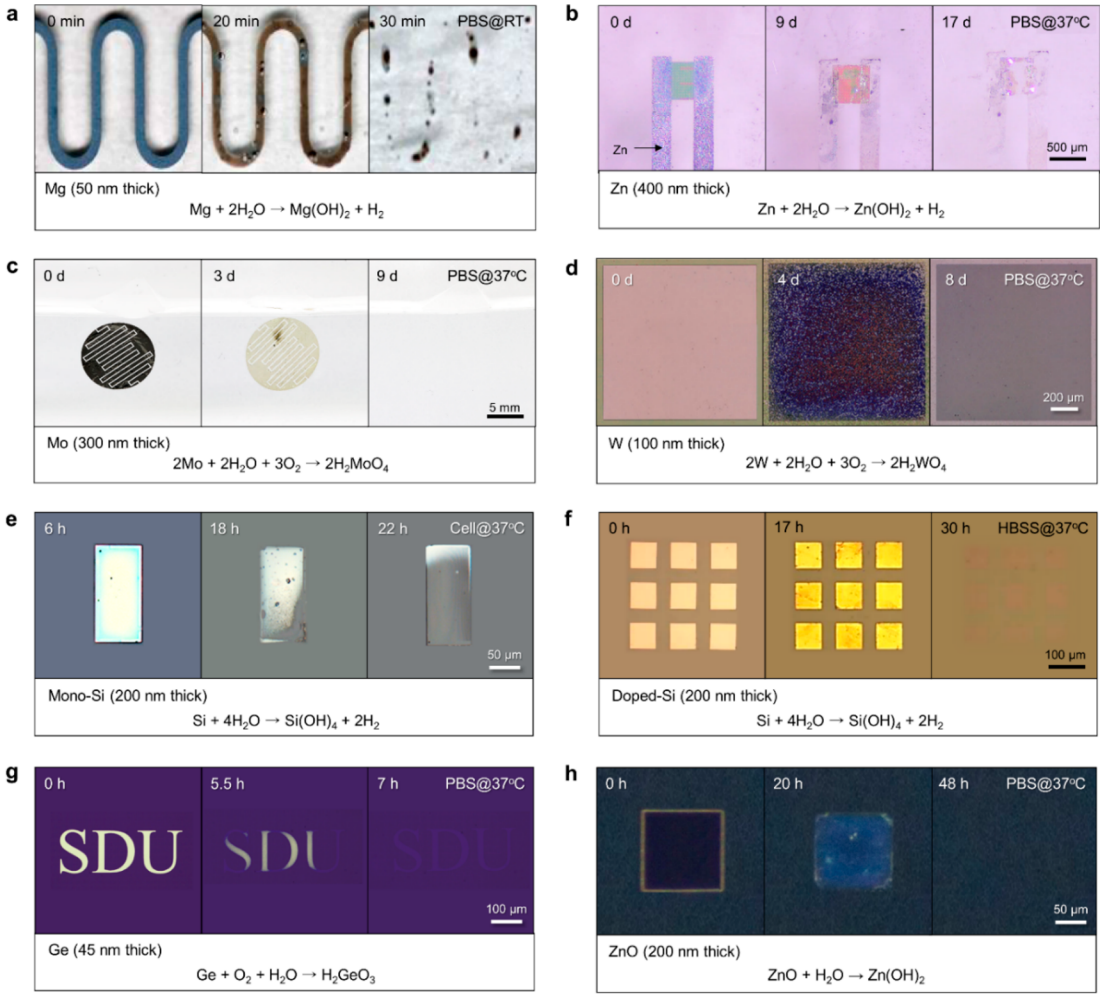

Figure 2. Chemical reactions associated with the dissolution of bioresorbable inorganic conductors and semiconductors. (a–d) Sequence of images showing the dissolution of patterns of conducting materials (top) and associated reactions (bottom). (a) Mg (50 nm thick).[35] Reproduced with permission from ref 35. Copyright 2016 American Chemical Society. (b) Zn (400 nm thick).[36] Reproduced with permission from ref 36. Copyright 2019 Springer Nature. (c) Mo (300 nm thick).[16] Reproduced with permission from ref 16. Copyright 2017 Wiley-VCH. (d) W (100 nm thick).[17] Reproduced with permission from ref 17. Copyright 2019 Wiley-VCH. (e–h) Sequence of images showing the dissolution of patterns of semiconducting materials (top) and associated reactions (bottom). (e) Mono-Si (200 nm thick).[87] Reproduced with permission from ref 87. Copyright 2018 American Chemical Society. (f) doped-Si (200 nm thick).[20] Reproduced with permission from ref 20. Copyright 2017 American Chemical Society. (g) Ge (45 nm thick).[19] Reproduced with permission from ref 19. Copyright 2022 Springer Nature. (h) ZnO (200 nm thick).[17] Reproduced with permission from ref 17. Copyright 2019 Wiley-VCH.

defined by their Pauling electronegativity, are much higher (Mo, 2.16; W, 2.36) than for Zn (1.65), Fe (1.83), and Mg (1.31), lead to a relative resistance to the formation of thick oxides. A composite composed of Mo microparticles (1–5 μm in diameter) in a matrix of the bioresorbable polymer poly-butanedithiol 1,3,5-triallyl-1,3,5-triazine-2,4,6(1*H*,3*H*,5*H*)-trione pentenoic anhydride (PBTPA) has a conductivity of 1000 S m^{-1} at a volume fraction of 0.35 of Mo/PBTPA.[44] Penetration of water molecules into the matrix triggers degradation in interfacial adhesion between the Mo particles and the PBTPA, thereby leading to gradual loss of conductivity, as evaluated in PBS (pH 7.4 at 37 °C). Similar studies based on W micro/nanoparticles in bioresorbable polymers such as beeswax (W particles with diameters of 500 nm),[45] candelilla wax (W particles with diameters of 5 μm),[46] and PEO (W particles with diameters of 4–6 μm)[41] show conductivities of ≈6400 S m^{-1} at 27 vol %, ≈ 4200 S m^{-1} at 35 vol % and 5200 S m^{-1} at a weight ratio of W:PEO:methanol = 40:2.5:10, respectively, as expected due to percolation effects. Both composites retain excellent conductivity in PBS at 37 °C for 4–5 days, significantly longer than that achieved with PBTPA (~1 day).

Advanced composites of these general types exploit sintering processes at the junctions between metal microparticles, to eliminate the surface oxide layer. In one example, laser-induced thermal sintering fuses Zn particles (1–5 μm in diameter) to form percolating conductive paths.[47−49] The resulting sintered Zn/poly(vinyl alcohol) (PVA) films (8–16 μm thick) offer conductivities of 2 × 10^6 S m^{-1}, which are 10 orders of magnitude higher than that of an otherwise similar, but nonsintered, film. Electrochemically sintering Zn particles with acidic solution is also possible.[50] The ink formulation in this case consists of Zn particles (<10 μm in diameter) mixed with polyvinylpyrrolidone (PVP) as a binder in isopropyl alcohol (IPA) (Zn:PVP:IPA = 30:1:10 by weight) to yield a printable ink. The sintering chemistry begins with dissolution of native oxides on the microparticles by a diluted acetic acid ($CH_3COOH:H_2O$, 1:10 by volume), followed by electrochemical self-exchange of Zn and Zn^{2+} at the Zn/H_2O interface.

https://doi.org/10.1021/acs.chemrev.3c00408
Chem. Rev. XXXX, XXX, XXX−XXX

Rapid (within several minutes), direct deposition of Zn from Zn^{2+} provides conductive contacts between adjacent Zn particles. Electrochemically sintered films of this composite (50 μm thick) show an increase of 8 orders of magnitude in conductivity compared to the nonsintered case, from 10^{-3} to 10^{5} S m^{-1}.

2.1.2. Organic Conductors. Conducting polymers (CPs) are an attractive alternative to the traditional metals described above, given their attractive processing options and their favorable mechanical properties. Preparation of CPs typically involves doping of conjugated polymers that have delocalized π-electrons along their backbone. Examples include polypyrrole (PPy) ($\approx 1.0 \times 10^{2}$ S cm^{-1}; doped with iron(III) chloride [$FeCl_3$]),[51] polyaniline (PANI) (2.8×10^{-2} S cm^{-1}; doped with sulfuric acid),[52] and poly(3,4-ethylenedioxythiophene) (PEDOT, 4.6×10^{3} S cm^{-1}; doped with polystyrene sulfonate).[53] The dopants increase the density of charge carriers, thereby leading to high levels of electrical conductivity. These same materials also support forms of ionic conductivity that can be important in biointerfaces. The following focuses mainly on electrical conductivity.

Although most CPs are chemically stable under physiological conditions (i.e., nondegradable), innovative designs and fabrication methods provide routes to various levels of degradability. Previous studies rely on mainly three approaches; (I) blends of CPs in insulating bioresorbable polymer matrices; (II) chemical modifications of CPs or their chemical integration with bioresorbable polymers; (III) polymerization with electroactive segments (i.e., mainly conducting oligomers), and degradable segments via cleavable linkers. The following presents examples of each approach. A subsequent subsection summarizes chemical aspects of the electrically insulating bioresorbable polymers mentioned below.

The first scheme yields partially bioresorbable conductors via combinations of CPs directly with bioresorbable insulating hosts, as percolating composites analogous to those described with traditional metals in the previous subsection. Examples include combinations of PPy, PANI, and PEDOT with various bioresorbable polymers such as poly(lactic-*co*-glycolic acid) (PLGA), poly(D,L-lactic acid) (PDLLA), poly(L-lactic acid) (PLLA), PCL, and silk fibroin (SF). Loading of 3 wt % PPy nanoparticles doped with $FeCl_3$ into PDLLA yields a material with an electrical conductivity of 1.0×10^{-3} S cm^{-1}.[54] Alternatives involve electrochemically deposited coatings of PPy on PLGA or PLLA fibers as supporting scaffolds, to increase the conductivity from less than 1.0×10^{-16} S cm^{-1} to as high as 1.0×10^{-4} S cm^{-1}, with a weight loss of 14−24% after 12 weeks under physiological conditions (PBS, pH 7.4 at 37 °C).[55,56] Besides synthetic bioresorbable polymers, natural polymers (e.g., silk fibroin) can also serve as bioresorbable hosts. Coating PPy directly on a substrate of silk fibroin creates a material in which the PPy disintegrates upon bioresorption of the silk, with an overall weight loss of 82% in PBS at 37 °C for 15 days.[57] PEDOT and PANI can be exploited in analogous ways. For instance, loading of 10 wt % PEDOT doped with hyaluronic acid (PEDOT-HA) into PLLA yields a conductivity of 4.7×10^{-3} S cm^{-1}. The rate of bioresorption of PEDOT-HA/PLLA is higher than that of PEDOT-PLLA, likely due to increased water penetration as a result of the hydrophilic HA domains.[58] An additional instance of PEDOT-based composites relies on PLGA microfibers (i.e., core) coated with PEDOT (sheath).[59] The weight ratios of PEDOT to PLGA decide the diameters of the microfibers, 3.7 ± 0.9 μm for 3:10, 2.9 ± 0.96 μm for 5:10, and ∼10 μm for 1:10. Here, the PEDOT sheath maintains its thickness of 500 nm regardless of type of microfibers, because PEDOT depends only on the amount of oxidant that can diffuse into the core for oxidative polymerization. The conductivity of this composite can reach from 0.2×10^{-1} to 2.8×10^{-1} S cm^{-1}. Examples of PANI doped with camphor sulfonic acid rely on coelectrospinning with gelatin[60] or poly(L-lactide-*co*-ε-caprolactone)[61] to yield fibrous sheets, with conductivities that range from $1.4-2.1 \times 10^{-2}$ S cm^{-1} at 30 wt % PANI.

The second approach involves modification of CPs with ionizable groups or incorporation/integration of modified CPs with degradable polymers. One study focuses on modification of the pyrrole monomer itself.[62] The reaction begins with introduction of functional groups (e.g., acid group for ionizable degradation; ester group for hydrolyzable degradation) such that subsequent oxidative electrochemical and ferric-chloride-mediated chemical reactions initiate polymerization of these modified monomers (i.e., modified PPy). Films (500 μm thick) based on this modified PPy-based material exhibit sheet resistances of 300 Ω sq^{-1} and mass loss of 100% within 24 h (pH 8.2) and 27% over 80 days (pH 7.2) at 37 °C, respectively. Another scheme[63] incorporates poly(ammonium(3-thienyl) ethoxypropanesulfonate) (SPT, conductive material) and poly(ethylenimine) (PEI, water-soluble material) into a fully bioresorbable CP. The negatively charged SPT and the positively charged PEI assemble into multilayer films (SPT-PEI) via layer-by-layer deposition techniques. The resultant multilayers exhibit conductivities as high as 2.76×10^{-2} S cm^{-1}, adjustable according to the number of cycles for coating of each film. Importantly, these multilayers fully degrade over 83−130 days in a physiological environment (pH of 7.4 and temperature of 37 °C).

The third approach involves polymerization of electroactive oligomer units (e.g., pyrrole-thiophene-pyrrole oligomers and aniline oligomers; aniline trimer, aniline tetramer, and aniline pentamer) and bioresorbable polymeric segments (e.g., PLA, PCL, PLLA, polyurethane [PU], poly(ester amide), glutaraldehyde, polyphosphazene, and polyglycerol sebacate) that include resorbable functional groups such as ester bonds, which hydrolyze to a carboxylic acid and an alcohol.[64−69] A recently reported, bioresorbable conductive form of PU (BCPU) is a representative example of this strategy. BCPU consists of copolymers of aniline trimers as an electroactive element and PCL as a bioresorbable element. The content of the trimer defines the electrical conductivity, ranging from 5.5×10^{-5} to 1.2×10^{-5} (in a dry state). *In vitro* dissolution tests reveal that the BCPU undergoes degradation by hydrolytic (in PBS at 37 °C) and enzymatic (with a lipase in PBS at 37 °C) reactions, with a mass loss of 12−14% after 8 weeks and 25% after 14 days, respectively.[70] In addition to aniline trimers, tetramers and pentamers can also bond with poly(ester amide) and PLA via cleavable linkages. Polymerization between aniline pentamers as an electroactive segment, glycine ethyl ester as a bioresorbable segment and phosphazene as a chemical linker (i.e., poly[(glycine ethyl ester) (aniline pentamer) phosphazene]) (PGAP) yields a material with an electrical conductivity of ∼2×10^{-5} S cm^{-1}.[69] Films of PGAP (100 μm thick) undergo hydrolytic degradation of ester bonds with a weight loss of 50% over 70 days under *in vitro* conditions (0.1 M PBS; pH 7.4 at 37 °C).

Table 1 provides an overview of the degradability of bioresorbable organic materials (conductors, semiconductors,

https://doi.org/10.1021/acs.chemrev.3c00408
Chem. Rev. XXXX, XXX, XXX−XXX

Table 1. Characteristics of Bioresorbable Organic Conductors, Semiconductors, and Insulators for Bioresorbable Electronic Devices[a]

materials	type	weight loss	degradation time	ref
Conductor				
modified PPy	synthetic	100% (thin film; pH 8.2)	24 h	62
		6−27% (pellet; pH 7.2)	80 days	
PEDOT:PSS	synthetic	100% (in protease solution)	4 weeks	71
DCPU	synthetic	12−14%	8 weeks	70
PGAP	synthetic	50%	70 days	69
PHAT	synthetic	50%	5 days	65
HPLAAT	synthetic	40−45%	3 days	68
SPT/PEI	composite	100%	12−18 weeks	63
PPy/PLA	composite	14−24%	12 weeks	56
PPy/SF	composite	82%	15 days	57
PANI/gelatin	composite	50−60%	7−14 days	72
Semiconductor				
melanin*	natural	100%	8 weeks	73
PDPP−PD	synthetic	100% (pH 4.6)	40 days	74
DDFTTF	synthetic	100% (pH 4.0)	80 days	75
Insulator				
SF	natural	100% (in protease solution)	4 weeks	71
candelilla wax*	natural	0.3 μm/day	0.3 μm/day	46
PLLA/PCL	synthetic	100%	100 days	76
PLA	synthetic	64%	12 months	77
PCL	synthetic	3%	5 weeks	78
PA	synthetic	100%	3−4 days	79
hydrophobic PA	synthetic	100% (for 1 mg)	42 days	80
PLGA (50:50)	synthetic	100%	30 days	81,82
PLGA (65:35)			40 days	
PLGA (75:25)			50 days	
PVA	synthetic	100%	30 min	83
POMaC	synthetic	77%	10 weeks	84
POC	synthetic	20%	21 days	85

[a]Results from degradation tests involve immersion in PBS at a pH of 7.4 and temperature of 37 °C. Asterisk marks (*) correspond to measurements in *in vivo* conditions.

insulators), expressed as weight loss (%) dissolved per day in PBS (pH 7.4) at 37 °C.

2.2. Bioresorbable Semiconductors

2.2.1. Inorganic Semiconductors. The discovery of chemical processes that lead to natural dissolution of monocrystalline, device-grade silicon (Si) under physiological conditions represents a major milestone in the development of realistic classes of bioresorbable electronic systems. Although silicon wafers are considered nonbiodegradable due to their large thicknesses (in the millimeter range) and the native oxides on their surfaces, various forms of silicon nanostructures (e.g., nanowires, nanoribbons, nanomembranes) can dissolve completely in relevant biofluids on time scales relevant for practical applications, i.e., several days or weeks, depending on the geometrical and surface chemical characteristics.[20] Previous studies suggest that bioresorption of silicon involves reactions with surrounding water to generate orthosilicic acid (i.e., $Si(OH)_4$) and hydrogen gas as products; $Si + 4H_2O \rightarrow Si(OH)_4 + 2H_2$.[86] Experiments show that monocrystalline silicon (mono-Si, 100 nm thick) exhibits rates of dissolution of ∼2−5 nm day^{-1} in PBS (0.1 M, pH 7.4 at 37 °C)[18] and complete resorption of mono-Si (200 nm thick) in cell culture environments at body temperature without adverse impact on cell metabolism (Figure 2e).[87]

The hydrolytic reactions of silicon nanostructures depend on the type and level of doping of the silicon.[2] Doping of Si nanomembranes (NMs, 70 nm thick) with phosphorus- and boron- for n- and p-type behavior, respectively, lead to a strong reduction of the dissolution rate from 3.1 and 2.9 nm day^{-1} (at a doping level of 10^{17}−10^{19} cm^{-3}) to 0.4 and 0.2 nm day^{-1} with dopant concentrations that exceed a certain level (i.e., ∼10^{20} cm^{-3}),[88] as measured by immersion in PBS (0.1 M, pH 7.4 at 37 °C). Studies of wet-etching of silicon in alkaline (i.e., high pH) solutions reveal that these differences follow partly from electrical effects associated with concentrations of electrons and holes, rather than the chemical effects of the dopants themselves.[88,89] The etching behaviors can be separated into two regimes; a constant etching rate (R) and a sharply decreasing rate, both of which depend on the concentration of dopants (C). The intersection of the asymptotes of these regions defines a critical dopant concentration (C_0). When $C_0 \gg C$ (below C_0), R is independent of the dopant concentration (C). For $C_0 \ll C$, R is inversely proportional to the fourth power of C, as described by the following equation at high pH: $R = R_i/(1 + (C/C_0)^4)$.[88,89] Another factor that contributes to doping dependent rates of dissolution arises from differences in the densities of the oxide layers (i.e., silicon dioxide, SiO_2) that spontaneously form on the silicon surface. Highly doped silicon exhibits stable and dense SiO_2 layers when immersed in water or biofluids.[90] Lightly doped silicon, by comparison, forms porous SiO_2 layers.[91] The dissolution rate of SiO_2 is much slower than that of silicon, thus providing a rate limiting step for dissolution of the underlying silicon.

The chemical composition of the surrounding solution (e.g., type of solution, additive species, pH level) can also strongly affect the rates of dissolution.[2,88,92] For example, dissolution of Si NMs (boron-doped, 10^{15} cm^{-3}) occurs at a rate of 58 nm day^{-1} in HBSS (pH 7.6 at 37 °C) and 21 nm day^{-1} in bovine serum (pH 7.4 at 37 °C) (Figure 2f).[20] Higher concentrations of anions (e.g., chloride [Cl^-] and phosphate [PO_4^{3-}] ions) and cations (e.g., sodium [Na^+], potassium [K^+], calcium [Ca^{2+}], and magnesium [Mg^{2+}] ions) in solutions can accelerate the degradation of Si.[20,92,93] Presence of divalent cations (i.e., 1 mM Ca^{2+} and Mg^{2+}), which are common in biological fluids and in HBSS increases the rate to 66 nm day^{-1}.[20] HBSS at enhanced basic conditions (i.e., pH 8.2) further accelerates the rate, consistent with results obtained at pH 7.6; 178 and 129 nm day^{-1} with and without Ca^{2+} and Mg^{2+}, respectively. Similarly, the presence of K^+ ions enhances the dissolution more than Na^+ ions under the same concentration of anions.[92] Phosphate solutions lead to faster dissolution than chloride solutions under the same concentrations of cations. By contrast, addition of protein (e.g., albumin, 6−35 g L^{-1}) in solution (i.e., PBS) decreases the rate by ∼30%, due likely to reduced transport kinetics associated with adsorption on the silicon surface (to a thickness of 0.5−1.5 nm).[20] The underlying chemical mechanism is related to the nucleophilic attack of surface bonds of Si that can cause weakening of interior bonds, thereby leading to accelerated formation of $Si(OH)_4$ as a degradation

https://doi.org/10.1021/acs.chemrev.3c00408
Chem. Rev. XXXX, XXX, XXX−XXX

product.[92,93] Interestingly, mechanical stirring in solution leads to decreases or increases in dissolution rate depending on the type of dopant, resulting from changes in the surface charge status with ion distribution at the interface between the silicon and the surrounding solution (i.e., interruption of the local enrichment of ions on the silicon surface).[93] For instance, stirring reduces the rate of dissolution of p-type Si NMs likely due to reduced enrichment of ions at the interface. Similar effects may explain experimental observations in p-type Si NMs that indicate decreases in lateral dimensions do not lead to increased rates. This effect largely disappears under stirring as a result of reductions in surface enrichment. By contrast, the surfaces of n-type Si NMs exhibit reduced adsorptive concentration of phosphate ions due to effects of electrostatic repulsion. Therefore, the dissolution rates of n-type Si show little dependence on lateral dimensions, but stirring can accelerate dissolution by removing reaction products from the near surface region. Therefore, geometrical design can be considered as an additional method for tuning the dissolution behavior of Si NMs.[93] Experimental studies show that square, pad-type Si electrodes (p-type: 10^{17} cm^{-3}; 300 μm long, 300 μm wide, 200 nm thick) dissolve faster than otherwise similar electrodes patterned into mesh geometries.

Silicon nanorods (NRs), nanowires (NWs), and/or nanoneedles (NNs) can also be considered for uses in bioresorbable platforms, particularly for minimally invasive and long-term sustained drug delivery due to their nanoscale size, low toxicity, and slow degradation rate (<20 nm day^{-1}).[94,95] These materials follow identical degradation chemistry with Si NMs (i.e., hydrolysis), where Si bonds at the surface undergo nucleophilic attack by OH^- groups in water.[92] Examples of porous Si NNs (900 nm in diameter and 60 μm long) gradually resorb over 2 months when embedded in 1.4% agarose gel with 1 mL of simulated tear fluid at 37 °C.[96] An increase in the surface porosity from 0 to 60% accelerates the dissolution rate from 3.5 to 16.6 nm day^{-1}. Conformal coatings can extend the stability of these and other silicon nanostructures (i.e., decrease in degradation rate) in physiological environments.[96,97] For example, Si NWs (30 nm in diameter) coated with 0, 5, and 10 nm thick aluminum oxide (Al_2O_3) shells (annealed for 1 min at 400 °C) degrade in 1× PBS at 37 °C over 10, 50, and 100 days, respectively.[97]

In addition to mono-Si, additional forms of silicon (e.g., amorphous silicon [a-Si]; polycrystalline silicon [poly-Si]), along with other materials such as germanium (Ge), Si−Ge alloys, zinc oxide (ZnO), aluminum zinc oxide (Al: ZnO), and indium−gallium-zinc oxide (IGZO, indium [In], gallium [Ga]) can be used as fully or partially bioresorbable inorganic semiconductors. For instance, a-Si (100 nm thick) and poly-Si (100 nm thick) dissolve at rates of 4.1 and 2.8 nm day^{-1} in PBS (0.1 M, pH 7.4 at 37 °C), respectively, with qualitatively similar dissolution chemistries.[18] Even at similar pH and temperature, bovine serum leads to dissolution rates that are 30−40 times higher than those of the PBS, corresponding to 130 and 100 nm day^{-1} for a-Si and poly-Si, respectively.[18] The lower density of a-Si compared to that of poly-Si results in an increase in the rate of water diffusion and reaction, leading to an accelerated rate.[37] As another example, Ge (45−100 nm thick) undergoes similar mechanisms of hydrolysis to those with silicon ($Ge + O_2 + H_2O \rightarrow H_2GeO_3$), dissolving at a rate of 3.1, 6.5, and 30 nm day^{-1} in 0.1 M PBS, 10 M PBS, and bovine serum (pH 7.4 at 37 °C), respectively (Figure 2g).[18,19] Alloys of Si and Ge (Si−Ge, 100 nm thick) are important for applications in high speed electronics. Si−Ge dissolves at a rate of 0.1 nm day^{-1} in PBS (0.1 M, pH 7.4 at 37 °C), which is ∼30 times slower than those of mono-Si and Ge. The rate for Si−Ge is strongly accelerated (∼185 times) in bovine serum.[18]

Studies of ZnO show that it is also soluble to forms of hydroxide or ions according to $ZnO + H_2O \rightarrow Zn(OH)_2$ and $ZnO + H_2O \rightarrow Zn^{2+} + 2OH^-$. Such materials can be exploited as bioresorbable n-type semiconductors for p−n junctions in diodes (including light emitting diodes) or as semiconductor layers in thin-film transistors (TFTs).[17,98] Simple sputtering techniques can form high quality films. Pulsed laser deposition yields ZnO films (200 nm thick) on Si(111) that dissolve at rates of 4 nm day^{-1} in PBS (pH 7.4 at 37 °C) (Figure 2h).[17] Related work shows that amorphous IGZO (35 nm thick) can be deposited by sputtering, also for use in TFTs.[99] Here, the processes of dissolution begin with formation of indium and gallium oxides (In_2O_3, Ga_2O), and $Zn(OH)_2$ through hydrolysis. Next, each oxide and hydroxide reacts with water to produce biproducts according to $In_2O_3 + 3H_2O \rightarrow 2In(OH)_3$ or $In_2O_3 + H_2O \rightarrow 2InOOH$;[37,99] $Ga_2O + 4(OH) \rightarrow 2GaO(OH) + H_2O$;[100] $ZnO + H_2O \rightarrow Zn(OH)_2$,[98] but the resultant gallium oxide forms insoluble metal hydroxides.[99,100]

Transition metal dichalcogenides (TMDs) as semiconductors of the type of MX_2, where M corresponds to a transition metal (e.g., Mo or W) and X is a chalcogen atom (e.g., sulfur [S], selenium [Se], or tellurium [Te]), can in certain cases exhibit dissolution behaviors via hydrolysis. Cases of particular interest include molybdenum disulfide (MoS_2, band gap [E_g] = 1.88 eV for monolayer) and tungsten disulfide (WS_2, E_g = 2.03 eV for monolayer) due to their direct bandgap, strong spin−orbit coupling and favorable electronic and mechanical properties.[101,102] Nanosheets of MoS_2 (80−160 nm thick) and WS_2 (40−64 nm thick) synthesized by hydrothermal methods dissolve at rates of 1.4−2.8 and 0.7−1.1 nm day^{-1} in PBS at 37 °C, following two steps, $2MoS_2 + 7O_2 \rightarrow 2MoO_3 + 4SO_2$ and $MoO_3 + 2OH^- \rightarrow MoO_4^{2-} + H_2O$; $2WS_2 + 7O_2 \rightarrow 2WO_3 + 4SO_2$ and $WO_3 + 2OH^- \rightarrow WO_4^{2-} + H_2O$, respectively. Recent results demonstrate the biocompatibility and nontoxicity of MoS_2 and WS_2, suggesting their potential suitability for bioresorbable electronic implants.[103−106]

Figure 4b summarizes the dissolution kinetics of inorganic semiconductors in various biofluids at physiological conditions (pH 7.4 at 37 °C).

2.2.2. Organic Semiconductors. Bioresorbable semiconductors based on organic polymers are of interest as alternatives to the inorganic materials described above. Attractive features are in low-temperature synthesis and processing, flexible/robust mechanical characteristics, versatile options in modification for sensing capabilities, and chemically tailored rates of dissolution. Many of these materials follow from natural dyes or pigments, such as indigo, melanin, β-carotene, and perylene diimide (PDI). Their semiconducting characteristics originate from π-conjugated structures, similar to those described previously in the context of CPs, thereby enabling efficient charge transport. One early example is in the use of a layer of indigo (40 nm thick) as a p-type channel material for an ambipolar field-effect transistor (FET).[107] The high crystallinity of indigo (E_g = 1.7 eV) can be favorable for interfacial charge transport, with a hole mobility of 5×10^{-3}−1×10^{-2} cm^2 V^{-1} s^{-1}. PDI (E_g = 2.02 eV for monomer; E_g = 1.95 eV for polymer) is a high-grade dye that acts as an n-type organic semiconductor,[108,109] attractive due to strong stacking of π-conjugated structures with high electron affinity, long excited

https://doi.org/10.1021/acs.chemrev.3c00408
Chem. Rev. XXXX, XXX, XXX−XXX

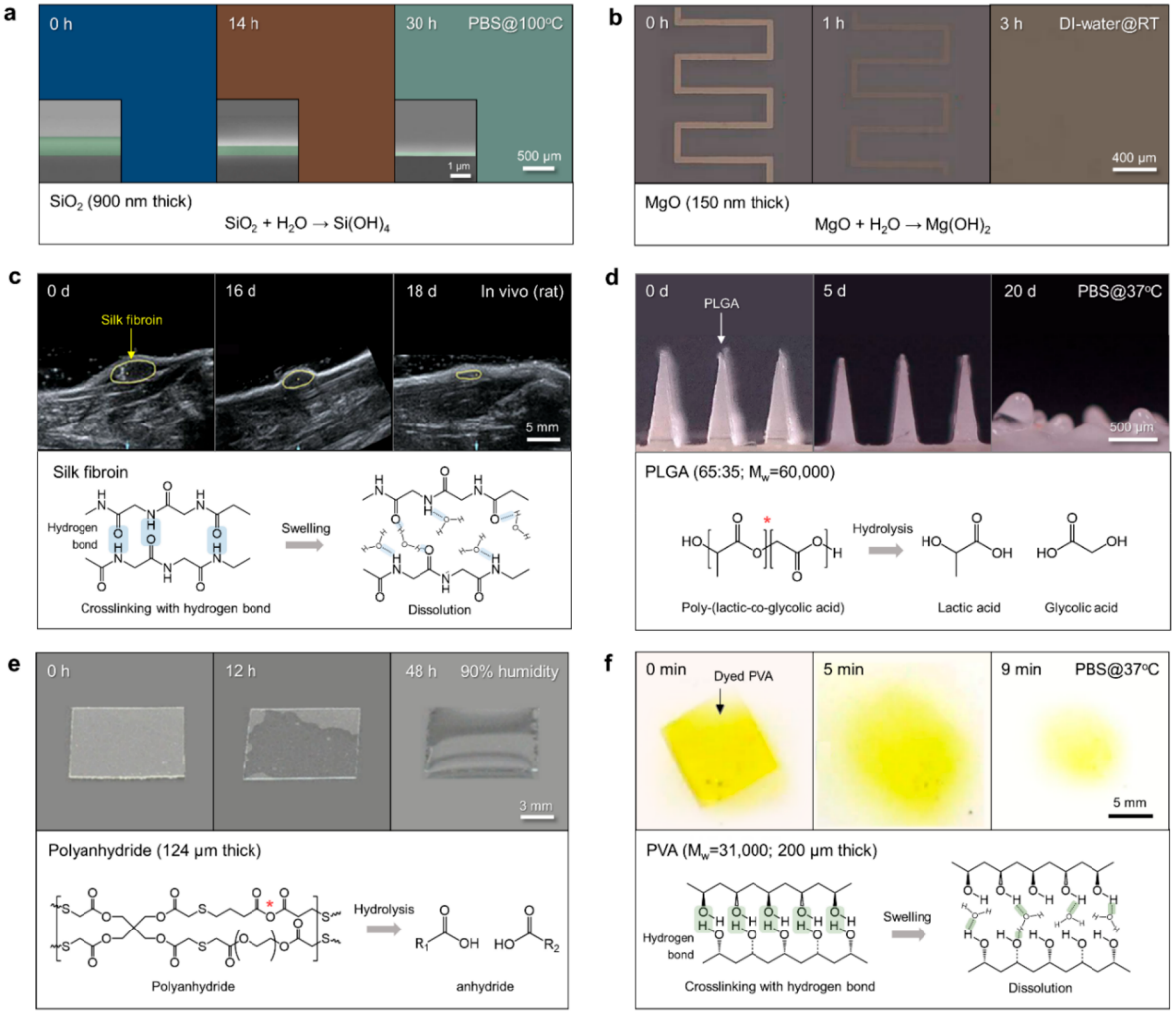

Figure 3. Chemical reactions associated with the dissolution of bioresorbable inorganic and organic insulators. (a,b) Sequence of images showing the dissolution of patterns of inorganic insulating materials (top) and associated reactions (bottom). (a) SiO_2 (900 nm thick). Inset, cross-sectional scanning electron microscope images.[128,129] Reproduced with permission from ref 128. Copyright 2017 American Chemical Society. Reproduced with permission from ref 129. Copyright 2016 United States National Academy of Sciences. (b) MgO (150 nm thick).[86] Reproduced with permission from ref 86. Copyright 2012 American Association for the Advancement of Science. (c–f) Sequence of images showing the dissolution of patterns of organic insulating materials (top) and associated reactions (bottom). (c) Silk fibroin hydrogel.[130] Reproduced with permission from ref 130. Copyright 2018 BioMed Central. (d) PLGA (65:35, M_w = 60 000).[131] Reproduced with permission from ref 131. Copyright 2022 American Chemical Society. (e) PA (124 μm thick).[4] Reproduced with permission from ref 4. Copyright 2017 American Association for the Advancement of Science. (f) PVA (200 μm thick, M_w = 31 000).[132] Reproduced with permission from ref 132. Copyright 2020 American Chemical Society.

state lifetime, strong visible light absorption, and high fluorescence quantum yield. These properties allow for use of PDI in bioresorbable TFTs, solar cells, or photodetectors. The presence of C–C and C–N chemical bonds in the backbone, however, prevents complete dissolution. Incorporating these π-conjugated molecules in bioresorbable polymeric matrices (e.g., coating on PLGA (40 nm in diameter); copolymerization with PCL) contributes to improved bioresorption under physiological conditions.[110,111]

Purely synthetic organic semiconductors are also of interest. A fully degradable semiconductor of this type (e.g., PDPP–PD) involves polymerization between diketopyrrolopyrrole (DPP) and phenylenediamine (PD) via imine chemistry.[74] The imine bonds form a stable conjugated linker at neutral pH, but they undergo rapid hydrolysis with a catalytic acid. Studies of films of PDPP–PD suggest that degradation occurs in two steps: (I) hydrolysis of imine bonds under acidic catalysis and (II) further degradation of DPP monomers due to reaction with water and the lactam rings. Through this chemistry, thin films (40 nm thick) completely disappear after 30 days in aqueous buffer solution (pH 4.6). Additional examples are thiophene-based materials, 5,5′-bis(7-dodecyl-9*H*-fluoren-2-yl)-2,2′-bithiophene (DDFTTF), deposited by thermal evaporation to yield p-type thin film semiconductors. Although not fully understood, reactions of DDFTTF are likely similar to those for melanin, a bioresorbable and biocompatible amorphous semiconductor. In particular, melanin formed from 5,6-dihydroxyindole monomer degrades to pyrrole-2,3,5-tricarboxylic acid and pyrrole-2,3-dicarboxylic acid. Full bioresorption of melanin thin films (100 μm thick) occurs in 8 weeks *in vivo*.[73] Thin-film transistors that include DDFTTF as semiconducting layers deposited by thermal evaporation completely disappear after 70 days in citrate buffer (pH 4.0 at 37 °C).[75]

Studies over the past decade indicate that a number of other synthetic organic semiconductors (e.g., *N*,*N*′-ditridecylperylene-3,4,9,10-tetracarboxylic diimide (P13, n-type) and ω-

https://doi.org/10.1021/acs.chemrev.3c00408
Chem. Rev. XXXX, XXX, XXX–XXX

dihexyl-quaterthiophene (DH4T, p-type),[112] hexadecafluorophthalocyanine copper ($F_{16}CuPc$, n-type) and pentacene (p-type),[113] poly(3-hexylthiophene): polystyrene (P3HT: PS, p-type),[114] poly[4-(4,4-dihexadecyl-4*H*-cyclopenta[1,2-*b*:5,4-b′]-dithiophen-2-yl)-*alt*-[1,2,5]-thiadiazolo-[3,4-*c*]pyridine] (PCDTPT, p-type)[115]) can be considered as bioresorbable candidates for organic field effect transistors (OFETs). In many cases, however, detailed studies of their dissolution behaviors in water or biofluids at physiologically relevant conditions remain to be performed.

Carbon nanotubes (CNTs) in arrays or networks can serve as an organic thin film type semiconductor or a conductor depending on the electronic nature of the CNTs. Although the CNTs are not degradable, blending them into a bioresorbable matrix (e.g., polybutylene succinate, PCL, PLA, PEO)[116−119] or directly coating them on a bioresorbable supporting substrate (e.g., PVA, cellulose)[120,121] lead to transience through partial disintegration and dissolution of the matrix. The strategies (II) for fabricating organic conductors, previously mentioned in the subsection of 2.1.2, can be exploited with CNTs. Promising examples involve chemically functionalized CNTs with degradable segments (e.g., poly(L-lactide-*co*-ε-caprolactone), PLLA) for improved degradability as well as biocompatibility.[122,123]

2.3. Bioresorbable Insulators

Bioresorbable insulating materials (e.g., metal oxides, metal nitrides, and polymers) can serve as gate dielectric layers in transistors, as isolation layers between conductive traces or electrodes, as passivating coatings, as encapsulation structures, or as supporting substrates. The following subsections summarize recent progress on materials for these purposes, divided into inorganic and organic types, as in the previous subsections.

2.3.1. Inorganic Insulators. Recent work on inorganic insulators includes SiO_2, silicon nitride (Si_3N_4), and magnesium oxides (MgO), along with examples of the use of lightly doped mono-Si as an encapsulant. These materials are compatible with a range of growth and deposition techniques, and with associated patterning options, thereby enabling selective application to desired regions of a substrate. Previous studies demonstrate uses of such materials in capacitors,[24,86] transistors,[8,124] interlayers,[125,126] passivation coatings, and barriers against water permeation.[20,21,127] Bioresorption occurs under physiological conditions via hydrolytic processes. Silicon oxide and silicon nitride deposited by plasma-enhanced chemical vapor deposition (PECVD) represent good choices for inorganic materials-based encapsulation.[127] Multilayer structures reduce the effects of pinholes and defects. Atomic layer deposition (ALD) is also attractive option for forming encapsulation layers.[127]

SiO_2 dissolves via the reaction $SiO_2 + 2H_2O \rightarrow Si(OH)_4$, similar to the chemistry associated with Si (Figure 3a). The rate of dissolution in PBS (pH 7.4 at 37 °C) is, however, much slower than that of Si, depending on the methods for deposition or growth and their effect on the density or stoichiometry. For example, SiO_2 films (100 nm thick) show dissolution rates of 0.005, 0.01, 0.1, 0.44, and 10 nm day^{-1} in PBS (pH 7.4) at 37 °C when formed by thermal growth in O_2 (tg-dry) and H_2O (tg-wet) vapor, by PECVD, by magnetron sputtering deposition and by electron beam physical vapor deposition (EBPVD), respectively.[17,127,128] The tg-dry and PECVD oxides typically have ideal stoichiometry (i.e., SiO_2), while EBPVD oxides are rich in oxygen (i.e., $SiO_{2.2}$). Relatively higher density (2.31 g cm^{-3}) and favorable stoichiometry (Si:O = 1:2) for tg-dry oxides contribute to their very low rates of dissolution, by comparison to those for the relatively lower density (1.9 g cm^{-3}) and nonstoichiometric chemistry (Si:O = 1:2.2) that results from EBPVD.[127] Reduced density can improve the diffusion of aqueous solutions into the materials, thereby accelerating the hydrolysis reaction by increasing the reactive surface area. As for materials described in other subsections, the chemistry of the aqueous environment affects the rates. In artificial cerebrospinal fluid (ACSF, pH 7.4 at 37 °C) the kinetics of SiO_2 films deposited by PECVD are faster by up to ∼82 times (i.e., 0.1−8.2 nm day^{-1}).[125]

Si_3N_4 dissolves in two steps, (I) oxidation into silicon oxide ($Si_3N_4 + 6H_2O \rightarrow 3SiO_2 + 4NH_3$) and (II) hydrolysis of silicon oxide into silicic acid ($SiO_2 + 2H_2O \rightarrow Si(OH)_4$). As with SiO_2, the methods for deposition affect the hydrolysis kinetics. In PBS (pH 7.4 at 37 °C), Si_3N_4 films (100 nm thick) deposited by low-pressure chemical vapor deposition (LPCVD), PECVD-low frequency (LF) and PECVD-high frequency (HF) exhibit rates of dissolution of 0.16, 0.85, and 0.85 nm day^{-1}, respectively.[127] LPCVD nitrides have higher densities (3.1 g cm^{-3}) and favorable stoichiometries (Si:N = 3:3.9) compared to PECVD-HF nitrides (densities, 2.5 g cm^{-3}; stoichiometries, Si:N = 3:3.3).[127] In ACSF (pH 7.4 at 37 °C), the rate of dissolution for PECVD nitride is 6 times higher than that in PBS, i.e., 0.85 to 5.1 nm day^{-1}.[125]

Another option is MgO, which is known to form naturally on the surfaces of Mg-based bioresorbable implants. EBPVD and sputtering deposition can also yield films of MgO on various substrates. When exposed to physiologically relevant fluids, water molecules initiate a reaction to produce an associated hydroxide, according to $MgO + H_2O \rightarrow Mg(OH)_2$ (Figure 3b). Exposure to chloride ions (Cl^-) or an acidic environment can accelerate the rate, releasing Mg^{2+}, according to $MgO + 2H^+ \rightarrow Mg^{2+} + H_2O$.[133] A 130 nm-thick layer of MgO deposited by EBPVD dissolves in PBS (pH 7.4 at 37 °C) within 30 min at a rate of 6.3 μm day^{-1}.

SiO_2, Si_3N_4, and MgO are useful in bioresorbable capacitors as insulators and in transistors as gate dielectrics. For fabrication of bioresorbable p- and n-type metal oxide semiconductor field-effect transistors (MOSFETs), Si NM (300 nm thick); SiO_2, Si_3N_4, and MgO (<200 nm thick); and Mg (300 nm thick) can be used for channels, gate dielectrics, and electrodes, respectively.[8,86,98,124] Bioresorbable capacitors with these materials use conventional metal−insulator−metal structures. Recent applications of inorganic dielectric materials as insulators with corresponding dielectric constants (3.7−3.9 for SiO_2; 7.5 for Si_3N_4; 9.8 for MgO) are in structures of Mg/SiO_2/Mg and Mg/MgO/Mg.[24,86]

In addition to metal oxides or nitrides, encapsulation structures can use Si NMs in undoped or lightly doped forms, as an effective insulator for such purposes. Negligible water permeation or absorption, along with rates of surface erosion in bioresorption that match many practical requirements, are some appealing characteristics.[20] As one example, mono-Si NMs (1.5 μm thick) provide robust barrier properties for days or weeks, and up to 10 months at a dissolution rate of 4.8 nm day^{-1} in 1× PBS (pH 7.4) at 37 °C. By comparison, films of PLGA formed by spin-casting (5 μm thick) and those of SiO_2 (200 nm thick) formed by EBPVD allow permeation by bulk diffusion and transport through defect layers, respectively, within 10 min.

https://doi.org/10.1021/acs.chemrev.3c00408
Chem. Rev. XXXX, XXX, XXX−XXX

Figure 4c summarizes the dissolution kinetics of inorganic insulators in PBS and ACSF at physiological conditions (pH 7.4 at 37 °C).

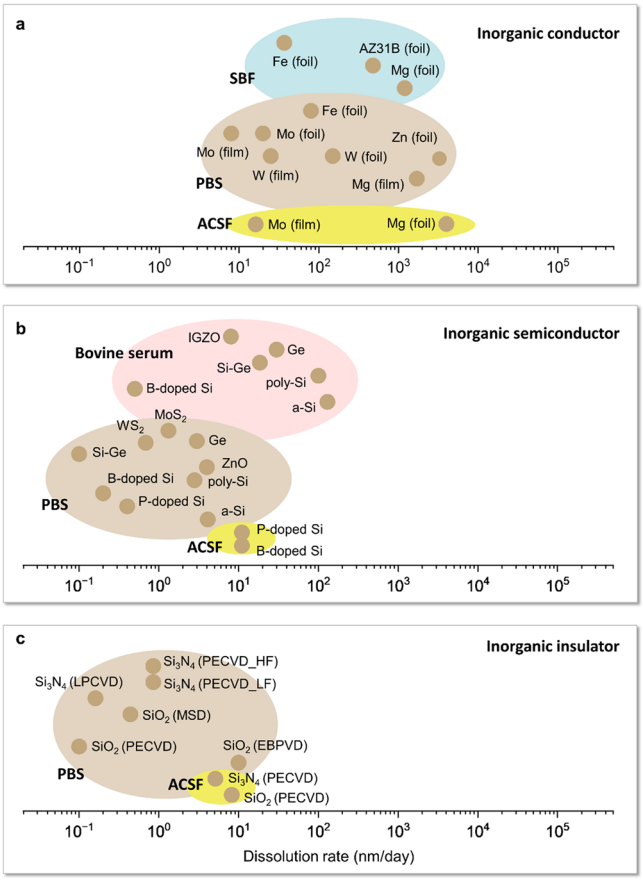

Figure 4. Plots of the rates of dissolution of inorganic (a) conductors, (b) semiconductors, and (c) insulators for bioresorbable electronic devices. These data result from tests that involve immersion in simulated body fluid (SBF), PBS, bovine serum, or ACSF at a pH of 7.4 and a temperature of 37 °C. Doping concentration of Si: 10^{20} cm^{-3} for P-doped Si and B-doped Si; data not available for poly-Si and a-Si.

2.3.2. Organic Insulators. Bioresorbable organic insulators include polymeric materials, with applications similar to those of their inorganic counterparts described in the previous subsection. Many papers report on various such materials for nonelectronic applications, in areas such as wound closure,[134] drug release/delivery,[135] temporary mechanical stents,[32] and tissue engineering.[136]

Polymers demonstrated to be useful in these contexts include naturally derived (e.g., silk, cellulose, sodium carboxymethylcellulose (Na-CMC), alginate, starch, chitosan, albumin, gelatin, keratin, shellac, candelilla wax, galactomannan, carrageenan-agar, polyhydroxybutyrate (PHB), polyhydroxyvalerate (PHV), and poly(3-hydroxybutyrateco-3-hydroxyvalerate) (PHBV)) and synthetic materials (e.g., PVA, PLGA, PLA, PCL, polyethylene glycol (PEG), polyethylene glycol diacrylate (PEGDA), polyglycolic acid (PGA), polyanhydride (PA), polydopamine (PDA), polybutylene adipate terephthalate (PBAT), poly(trimethylene carbonate) (PTMC), poly(desaminotyrosyl-tyrosine ethyl ester carbonate) (PDTEC), poly(glycerol sebacate) (PGS), and poly(octamethylene maleate (anhydride) citrate) (POMaC), pluronic). Chemistries for bioresorption follow four main mechanisms (Figure 5). (I) Dissolution: solvated polymer chains interact with water. (II) Enzymatic reaction: enzyme-catalyzed depolymerization. (III) Hydrolysis: water-induced depolymerization. (IV) Oxidative reaction: reactive oxygen (or nitrogen) species (ROS)-induced depolymerization.

Most commonly, bioresorbable polymers in film form undergo degradation in a two-step process that begins with diffusion of water into the polymer network followed by mechanism (I) (Figure 5a) of the swollen polymer by some combination of mechanisms (II), (III), and/or (IV) above. Typical natural polymers degrade via enzymatic reactions (Figure 5b), owing to the stability of their backbone structure.[137] Adsorbed enzymes on the surfaces of such polymers create an enzyme−substrate complex, capable of cleavage of the polymer chains as biological catalysts. The reaction products diffuse in the body through processes of bioaccumulation and mineralization. Natural silk is a representative example of a protein that degrades enzymatically, used

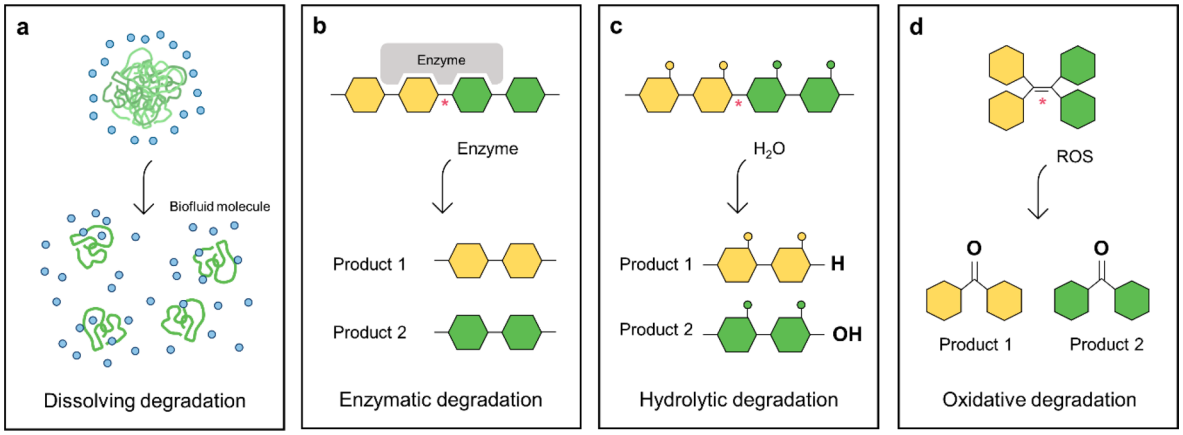

Figure 5. Schematic illustrations of representative mechanisms for in vivo degradation of bioresorbable polymers. (a) Dissolution: (i) diffusion of biofluid (mostly water molecules) into a solid polymer material, (ii) formation of a swollen state, (iii) desorption of the chains, and (iv) dispersion of solvated chains into a biofluid. (b) Enzymatic reaction: reaction with enzymes in surrounding biofluids leads to chemical cleavage of bonds in a polymer chain. (c) Hydrolysis: reaction with surrounding water molecules leads to chemical cleavage of bonds in a polymer chain. (d) Oxidative reaction: reactive oxygen species along with free radicals released by inflammatory cells cause depolymerization. Each asterisk (*, marked in red) represents hydrolyzable, enzymatic, or oxidative bonds.

https://doi.org/10.1021/acs.chemrev.3c00408
Chem. Rev. XXXX, XXX, XXX−XXX

as a substrate in early work on bioresorbable electronics.[10,71,86,138,139] One report describes that *in vitro* degradation of silk films (60 μm thick) occurs completely within 4 weeks of dissolution in PBS with protease at 37 °C.[71] Studies of the degradation of silk gel implants in rat models indicate a gradual decrease in the volume over 18 days (Figure 3c).[130] An attractive feature of silk is that its rate of dissolution depends strongly on the degree of crystallization of hydrophobic domains via β sheet formation.[140] In a highly crystalline state, the rates are slow, but silk in this form tends to be brittle and difficult to handle. In a largely amorphous state, the silk is flexible, but incompatible with aqueous processing steps due to a fast degradation rate.

Bioresorbable synthetic polymers degrade mainly via hydrolysis (Figure 5c).[137] In hydrolytic degradation, water molecules cleave hydrolyzable linkages (e.g., ester, carbonate, anhydride, amide bonds) in the polymer chain, generating oligomers or monomers that can be absorbed in the body.[32] Synthetic polymers undergo this form of degradation by bulk and/or surface erosion.[141] Rates of bond cleavage and diffusion of water or enzymes into the materials determine the relative contributions of these two modes.[32,142] In the bulk case, these species diffuse into the material and simultaneously produce degradation products (i.e., oligomers with hydroxyl and carboxylic acid groups) that gradually accumulate within the polymer. Subsequently, an autocatalytic reaction where accumulated degradation products act as a catalyst for continuous degradation leads to a decrease in the weight of polymers. In some cases, this process contributes to the disintegration of the structure, generating polymer debris, and an overall nonlinear rate of loss of mass/volume. Swelling is another associated consequence of bulk erosion, which can result in fracture of supported bioresorbable electronic materials and components prior to disintegration of the polymer.[143,144] This phenomenon can lead to failure of device performance, prior to dissolution of the constituent materials.[145] By contrast, the surface erosion case involves hydrolysis only on the surface. The degradation products diffuse away from the polymer matrix without autocatalytic effects, resulting in a linear loss in mass/volume over time. Strategies for tuning the rate of bioresorption of synthetic polymers include modulation of chemical and physical properties (e.g., composition, molecular weight, crystallinity, and hydrophilicity/hydrophobicity), blending, copolymerization, and surface modification. Typically, increasing the crystallinity, molecular weight or hydrophobicity reduces the rates.[32]

For PLA, PGA, PCL, PA, and copolymers (e.g., PLGA), the major degradation products via hydrolysis are small molecules of lactic acid, glycolic acid, and 6-hydroxyhexanoic acid.[137,146] These species can enter the tricarboxylic-acid cycle and can be eventually eliminated from the body as carbon dioxide and water. As an example, the composition of lactic and glycolic acid (i.e., lactic acid:glycolic acid; 75:25, 65:35, and 50:50 etc.) in the PLGA (undergoing hydrolytic bulk erosion) determines the rates of degradation. Increasing the ratio of lactic acid (hydrophobic unit) to glycolic acid (hydrophilic unit) reduces the rates of dissolution at physiological conditions (PBS; pH 7.4 at 37 °C); 75:25, 65:35, and 50:50 exhibit complete mass loss in 50, 40, and 30 days, respectively (Figure 3d).[81,82,131]

As with inorganic insulators, these and related organic alternatives can be valuable as encapsulating layers. Characteristics relevant to such applications are densities of surface defects, levels of hydrophobicity, rates of permeation of water, and water-induced swelling. Wax derived from natural sources (e.g., soybeans, myrica cerifera, candelilla shrubs) are of interest because of their exceptionally low water permeability, low swelling ratio, and bioresorbability (decreases in thickness by 28 $\pm$ 4 μm for 3 months *in vivo*). Brittle mechanical properties may represent drawbacks in certain instances. Soft, flexible materials such as poly(1,8-octanediol-*co*-citrate) (POC) avoid this limitation, as demonstrated in bioresorbable sensors and microfluidic coolers that can stretch to tensile strains up to 40%. These materials lose 20% of their original weight over 21 days in Dulbecco's Phosphate Buffered Saline (DPBS; pH 7.4) at 37 °C.[11,85,147] PA-based polymers also provide stable mechanical properties in flexible systems, with Young's moduli of 1−6 MPa.[80] Hydrolysis of the anhydride group generates carboxylic acid. One example describes rapid dissolution of thin PA film as a substrate (124 μm thick) in ambient air with sufficient humidity (Figure 3e).[4] Hydrolysis depends on the ratio of degradable monomer (i.e., anhydride) and the level of humidity. Adding a hydrophobic monomer such as 1,4-butanedithiol during polymerization can impart an intrinsic hydrophobic character to the PA-based materials.[80] The dissolution rate for hydrophobic PA at physiological conditions (PBS; pH 7.4 at 37 °C) is 10−15 times slower than the PA mentioned earlier. The linear, continuous decrease in thickness (1.3 μm day^{-1}) suggests that PA undergoes hydrolytic surface erosion.

In addition to hydrolysis, oxidation can represent a biologically relevant degradation mechanism (Figure 5d). Activated inflammatory cells such as macrophages and neutrophils release free radicals in the form of ROS that can initiate the depolymerization of polymers.[148] Degradable moieties for oxidative degradation include ethers, alcohols, aldehydes, amines, and carbons substituted by an aliphatic chain, aromatic cycle, or allylic carbons. PVA can serve as a bioresorbable substrate with rapid dissolution rate (<30 min) (Figure 3f).[132] Upon implantation, biofluids permeate into the polymer network, and then the PVA undergoes a cascade of reactions beginning with swelling and iterative oxidation by microbial, enzymatic hydrolysis by hydrolase (e.g., aldolase and β-diketone), eventually forming simple byproducts (i.e., acetic acid). The rate of dissolution depends on the degree of cross-linking and molecular weight. Increasing the molecular weight decreases the solubility due to inter- and intramolecular hydrogen bonds that form between the hydroxyl groups of the PVA molecules.

3. BIORESORBABLE DEVICES AND COMPONENTS

The materials described in section 2 can be combined into wide ranging classes of bioresorbable electronic components and sensors. This section highlights different categories of such devices, their operating principles and performance; examples include transistors, diodes, antennas, inductor-capacitor (LC) circuits, and different types of sensors (e.g., physical, chemical, and optical).

3.1. Bioresorbable Transistors

3.1.1. Inorganic Transistors. As a key active component in all modern electronics, MOSFET serves as the foundation for the digital age. A MOSFET comprises three terminals: an insulated gate (G), a source (S), and a drain (D). A voltage applied to the gate creates an electric field across an underlying oxide layer. This field accumulates charge carriers in an adjacent semiconductor layer to establish a conductive path between the

https://doi.org/10.1021/acs.chemrev.3c00408
Chem. Rev. XXXX, XXX, XXX−XXX

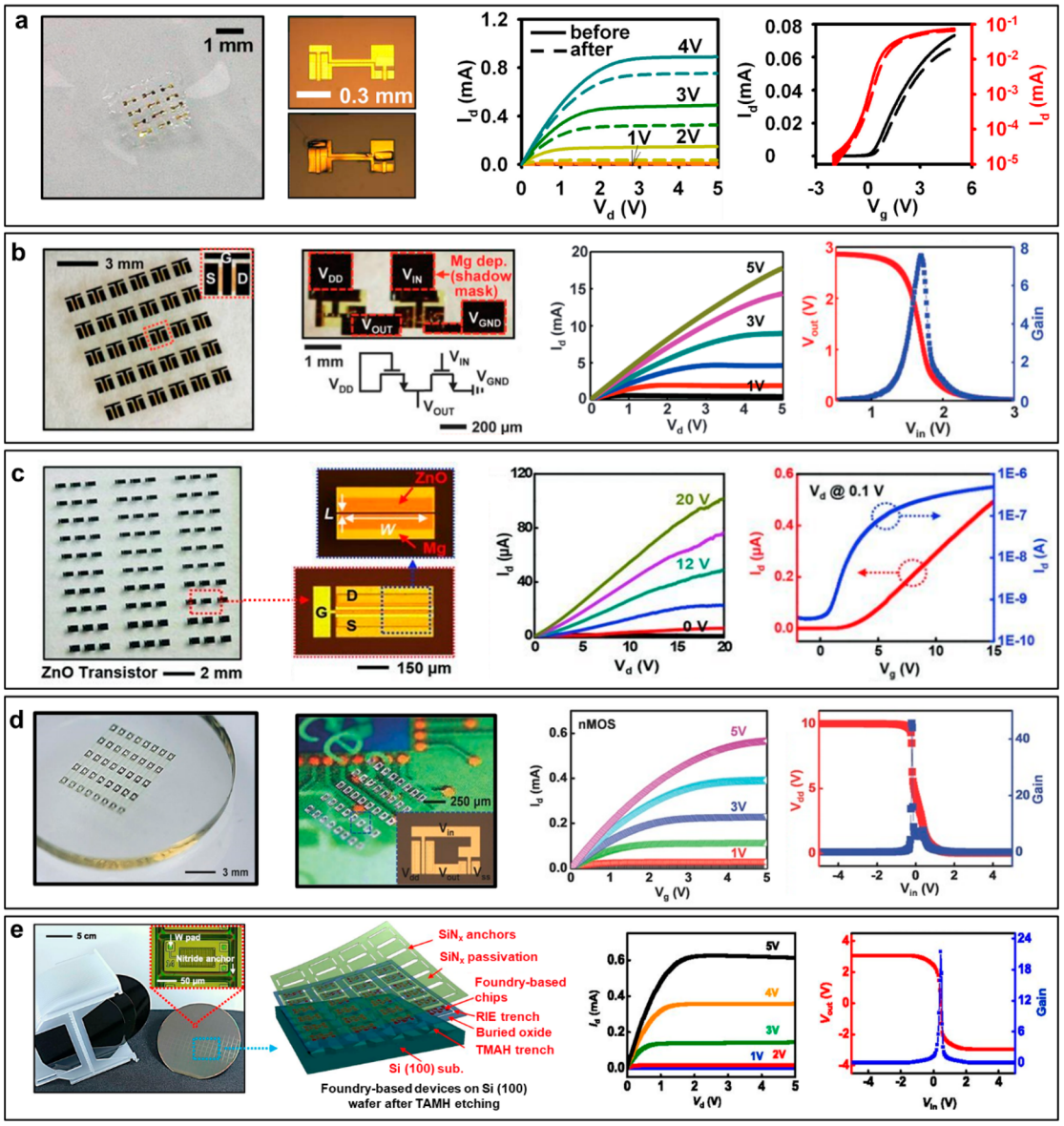

Figure 6. Representative examples of bioresorbable inorganic transistors and their electrical performance. (a) Left: Image of an array of Si MOSFETs on a silk substrate in the process of water dissolution. Middle-left: Optical micrograph of Si transistor on carrier wafer (top) and silk film (bottom). Middle-right: *I*−*V* characteristics at different gate bias voltages. Right: Transfer curves before (solid line) and after (dotted line) dissolution.[10] Reproduced with permission from ref 10. Copyright 2009 American Institute of Physics publishing. (b) Left: Image of an array of ZnO TFTs on a silk substrate. Middle-left: Optical micrograph of the TFT with Mg as source, drain, and gate electrodes, ZnO as active layer, and MgO as gate dielectric. Middle-right: *I*−*V* characteristics of a ZnO TFT at different gate bias voltages. Right: Transfer curves at a drain voltage of 0.1 V.[86] Reproduced with permission from ref 86. Copyright 2012 American Association for the Advancement of Science. (c) Left: Image of an array of Si p-channel MOSFETs with Mg as source, drain, gate electrodes, Si NM as active layer, and MgO as gate dielectric; magnified view of one device (inset). Middle-left: Image of a logic gate (inverter) composed of n-channel MOSFETs, with Mg as interconnects, Au as source, drain, and gate electrodes (top), in a circuit configuration in the diagram (bottom). Middle-right: *I*−*V* characteristics of a n-channel MOSFET. Right: Transfer characteristics of the p-channel inverter.[98] Reproduced with permission from ref 98. Copyright 2013 Wiley-VCH. (d) Left: Image of an array of Si CMOS inverters on a PLA substrate. Middle-left: Magnified view and optical micrograph (inset) of CMOS inverters on PLGA coated paper. Middle-right: *I*−*V* characteristics of the n-channel MOSFET. Right: Transfer characteristics of the CMOS inverter.[145,152] Reproduced with permission from ref 145. Copyright 2014 Wiley-VCH. (e) Left: Image of foundry fabricated chips, including capacitors, and p-channel and n-channel transistors on 6 in. Si wafer, with inset showing magnified view of a releasable configuration. Middle-left: Exploded view of device arrays after undercut release. Middle-right: *I*−*V* characteristics of the CMOS at different gate bias voltages. Right: Transfer characteristics of the CMOS inverter.[154] Reproduced with permission from ref 154. Copyright 2017 United States National Academy of Sciences.

source and drain. This field-induced switching serves as the basis for amplifying and routing electronic signals. Collections of MOSFETs form the basis of microprocessors, memories, radios, and many other functional building blocks, providing functions to implement logic gates and data storage for diverse applications of integrated circuits (ICs).

Such devices can be constructed from the bioresorbable materials described in section 2, in geometries that support functions over relevant timeframes. A first attempt describes integration of ultrathin, flexible silicon-based n-channel MOSFETs on biodegradable substrates of silk fibroin (Figure 6a).[10] The transistors in this case involve Si NMs on thin, flexible

https://doi.org/10.1021/acs.chemrev.3c00408
Chem. Rev. XXXX, XXX, XXX−XXX

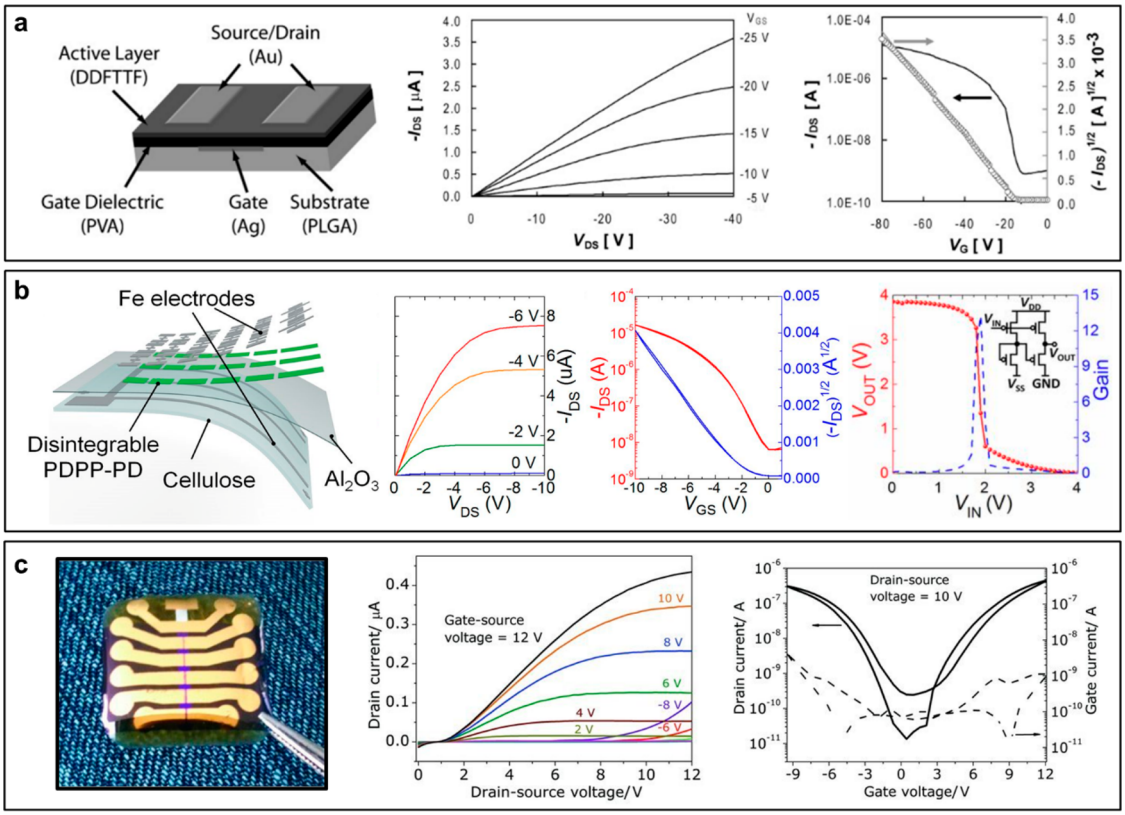

Figure 7. Representative examples of biodegradable organic transistors and their electrical performance. (a) Left: Schematic illustration of a semiconducting DDFTTF-based TFT on a PLGA substrate. Middle: $I-V$ characteristics of the transistor with cross-linked PVA dielectrics. Right: Transfer curves of the transistor with cross-linked PVA dielectrics.[75] Reproduced with permission from ref 75. Copyright 2010 Wiley-VCH. (b) Left: Exploded view of PDPP−PD polymer transistors on a cellulose film substrate. Middle-left: $I-V$ characteristics of PDPP−PD transistors. Middle-right: Transfer curves of PDPP−PD transistors. Right: Transfer characteristics of the PDPP−PD CMOS inverter in a circuit configuration in the diagram (inset).[74] Reproduced with permission from ref 74. Copyright 2017 United States National Academy of Sciences. (c) Left: Image of an ambipolar indigo transistor on shellac resin substrate. Middle: $I-V$ characteristics of the n-channel OFET. Right: Transfer characteristics of the OFET.[107] Reproduced with permission from ref 107. Copyright 2012 Wiley-VCH.

polyimide substrates, subsequently transfer printed to free-standing films of silk, to yield partially bioresorbable systems. The silk substrate not only permits rapid dissolution in water as a result of proteolytic activity,[149] but also supports mechanical flexibility as a platform for high performance Si NM-based devices. Electrical properties extracted from measurements on these devices (e.g., current−voltage [$I-V$] and transfer curves) reveal properties comparable to those formed with similar designs on silicon wafers: the mobilities, threshold voltages, and on/off ratios of ∼500 $cm^2\ V^{-1}\ s^{-1}$, ∼0.2 V, and $>10^4$. These properties remain unchanged even after dissolution of the silk (Figure 6a).

Extensions of this work reveal that both the Si NM and the SiO_2 thin films used in these devices are themselves soluble by hydrolysis over relevant time scales (days to weeks) in water and biofluids with biocompatible end products, as described in the section 2.[86] This realization forms the basis for the development of a broad range of NM-based electronic components, including p-channel MOSFETs formed with Si NMs as the semiconductors, SiO_2 as the gate dielectrics, Mg as the electrodes, with MgO for encapsulation on substrates of crystallized silk (Figure 6b). Logic gates (e.g., inverters) and more complex circuits can be formed using such types of n-channel MOSFETs, with saturation and linear regime carrier mobilities of 560 $cm^2\ V^{-1}\ s^{-1}$ and 660 $cm^2\ V^{-1}\ s^{-1}$, respectively, on/off ratios of $>10^5$, and threshold voltages of 0.1 V (Figure 6b). Other materials can be used in these and related devices that combine Si NMs with electrodes (e.g., Mg, Fe, Mo), gate dielectrics (e.g., spin-on glass [SOG], SiN_x), and substrates (e.g., Mo, Fe, W, Zn foils).[8,38,125−127,150] As an alternative to Si NMs, TFTs constructed with sputtered layers of ZnO as the semiconductor, Mg as electrodes and interconnects, MgO as gate and interlayer dielectrics, and silk as substrates and encapsulants (Figure 6c) are also possible.[98] Compared to Si NMs, thin films of ZnO offer unique properties such as transparency in the visible spectrum, piezoelectric responses, and direct bandgap behavior. The electron mobility, threshold voltage, and on/off ratio of transistors formed in this way are ∼0.95 $cm^2\ V^{-1}\ s^{-1}$, ∼1 V, and $>10^3$, respectively (Figure 6c). Other inorganic semiconductors, such as IGZO and Al: ZnO can also be used in bioresorbable transistors.[4,151]

Polymer alternatives to silk fibroin, described in section 2, can also serve as substrates for transistors and other components. Demonstrations include arrays of Si NM transistors on PLGA, PLA, PCL, rice paper, and levan polysaccharide (Figure 6d).[145,152] As before, these devices exhibit excellent performance: mobilities and on/off ratios of ∼400−500 $cm^2\ V^{-1}\ s^{-1}$ and $\sim10^5$, respectively; complementary metal-oxide-semiconductor (CMOS) inverters with gains of ∼80 and threshold voltages of ∼−1 V (Figure 6d). Other natural and synthetic biodegradable materials such as wood-derived cellulose nanofibril (CNF) and hydrolytically liable polyanhydride can also be considered.[4,153]

https://doi.org/10.1021/acs.chemrev.3c00408
Chem. Rev. XXXX, XXX, XXX−XXX

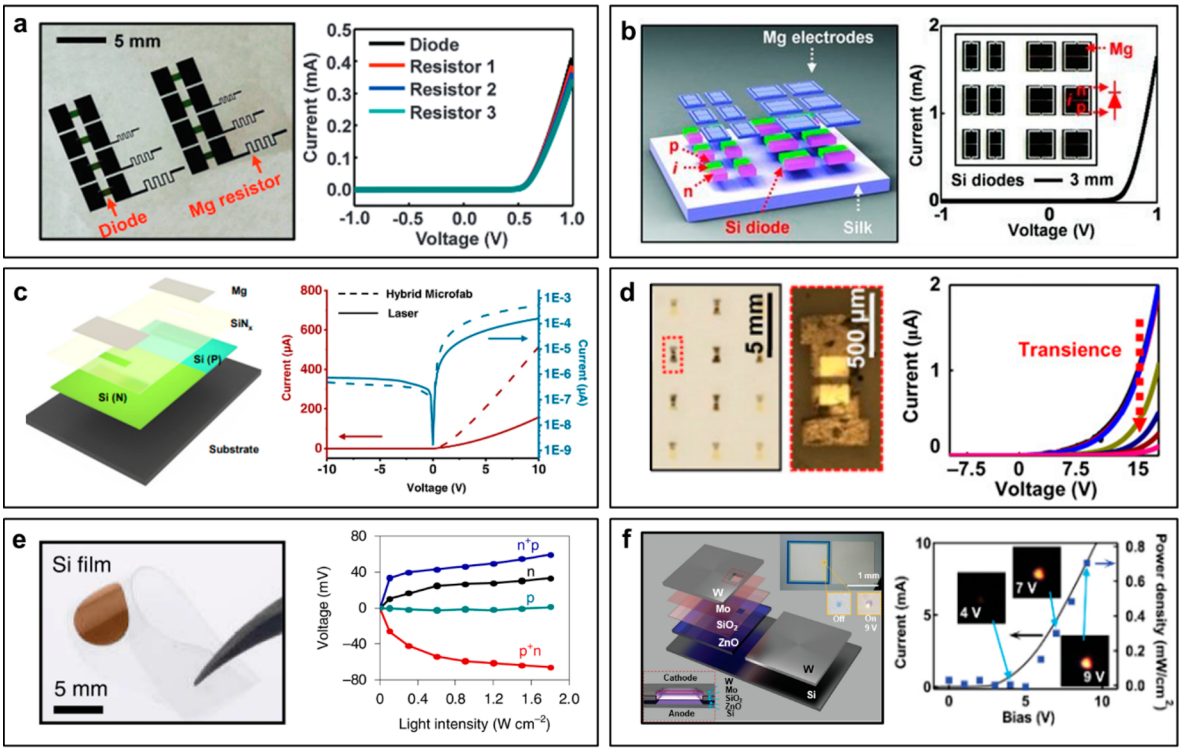

Figure 8. Representative examples of bioresorbable diodes and their electrical performance. (a) Left: Image of an array of Si NM pn diodes with serpentine Mg resistors on a silk substrate. Right: *I*–*V* characteristics of the diodes connected to three different resistors.[86] Reproduced with permission from ref 86. Copyright 2012 American Association for the Advancement of Science. (b) Left: Schematic illustration of Si NM PIN diode (rectifiers) with Mg electrodes on a silk substrate. Right: *I*–*V* characteristics of a diode with an image of the device (inset).[126] Reproduced with permission from ref 126. Copyright 2013 Wiley-VCH. (c) Left: Exploded view of a Si NM pn diode fabricated by laser ablation on a PLA substrate. Right: *I*–*V* characteristics of a laser-fabricated diode compared with that of a photolithography-fabricated diode in linear and log scale.[157] Reproduced with permission from ref 157. Copyright 2022 Springer Nature. (d) Left: Image of an array of IGZO Schottky diodes on a polyanhydride substrate (left) and magnified view of one diode (right). Right: *I*–*V* characteristics of an IGZO diode showing transience in moisture.[4] Reproduced with permission from ref 4. Copyright 2017 American Association for the Advancement of Science. (e) Left: image of a Si photodiode on a nonbiodegradable PET substrate. Right: Steady-state photovoltage versus light intensity for various types of Si pn junctions.[159] Reproduced with permission from ref 159. Copyright 2022 Springer Nature. (f) Left: Exploded view of a ZnO light-emitting diode (LED). Illustration of active components around transparent Mo window (bottom inset). Images of LEDs at on/off states (top inset). Right: Optical power density–current–voltage (*L*–*I*–*V*) curve of the ZnO LED.[17] Reproduced with permission from ref 17. Copyright 2019 Wiley-VCH.

The use of bioresorbable elastomers, such as POC, enable mechanical stretchability, often of interest in systems that require interfaces to soft tissues.[147] Specifically, patterning Si NM transistors into small regions and interconnecting them by planar serpentine and/or noncoplanar buckled electrical traces supports stable operation even under large uniaxial tensile strains (∼30%).

Similar types of Si NM transistors can be formed in foundry-compatible processes, as a step toward a scalable, manufacturable technology that leverages many aspects of the infrastructure associated with the semiconductor industry.[154] Here, p-channel and n-channel MOSFETs, inverters, and logic gates and others can be fabricated on standard silicon-on-insulator (SOI) wafers using common IC processes with certain materials substitutions (e.g., W for Cu) and configured to allow release, transfer printing and interconnection on bioresorbable substrates, such as those formed by PLGA (Figure 6e). Electrical measurements indicate expected characteristics for n-channel MOSFETs, including mobilities of ∼610−680 $cm^2 V^{-1} s^{-1}$, threshold voltages of ∼1.2 V, and on/off ratios of $\sim 10^8$. Interconnection of these transferred components is possible through photolithographic processing, provided that aqueous steps involve short times of immersion and/or protective layers to prevent unwanted dissolution of the constituent materials. Descriptions of complementary methods appear in section 5.

3.1.2. Organic Transistors. Organic and polymeric materials can also serve as the basis for diverse types of bioresorbable electronic devices. Despite relatively poor electrical properties by comparison to inorganic alternatives, organic materials are attractive for their mechanical properties, their solution processability, and their chemical diversity.[155]

Some of the earliest work describes the ability to form partially bioresorbable thin-film OFETs using a conjugated small-molecule, DDFTTF, as a p-channel semiconductor.[75] In example devices, Au, Ag, and PVA form the gate electrode, source/drain electrodes, and the gate dielectric, respectively. A film of PLGA serves as a substrate (Figure 7a). Depending on the methods for processing the PVA dielectric (either non-cross-linked or photo-cross-linked), these DDFTTF-based transistors exhibit mobilities between ∼0.06 and 0.2 $cm^2 V^{-1} s^{-1}$, threshold voltages between ∼−15.4 to −18.9 V, and on/off ratios between ∼3.2 and 5.5. Although neither the DDFTTF nor the Au/Ag electrodes are bioresorbable, these components correspond to less than 0.1% of the total mass of the device and they are all biocompatible.

A recent demonstration of fully biocompatible and disintegrable OFET involves a pseudo-CMOS inverter (Figure 7b).[74]

https://doi.org/10.1021/acs.chemrev.3c00408
Chem. Rev. XXXX, XXX, XXX−XXX

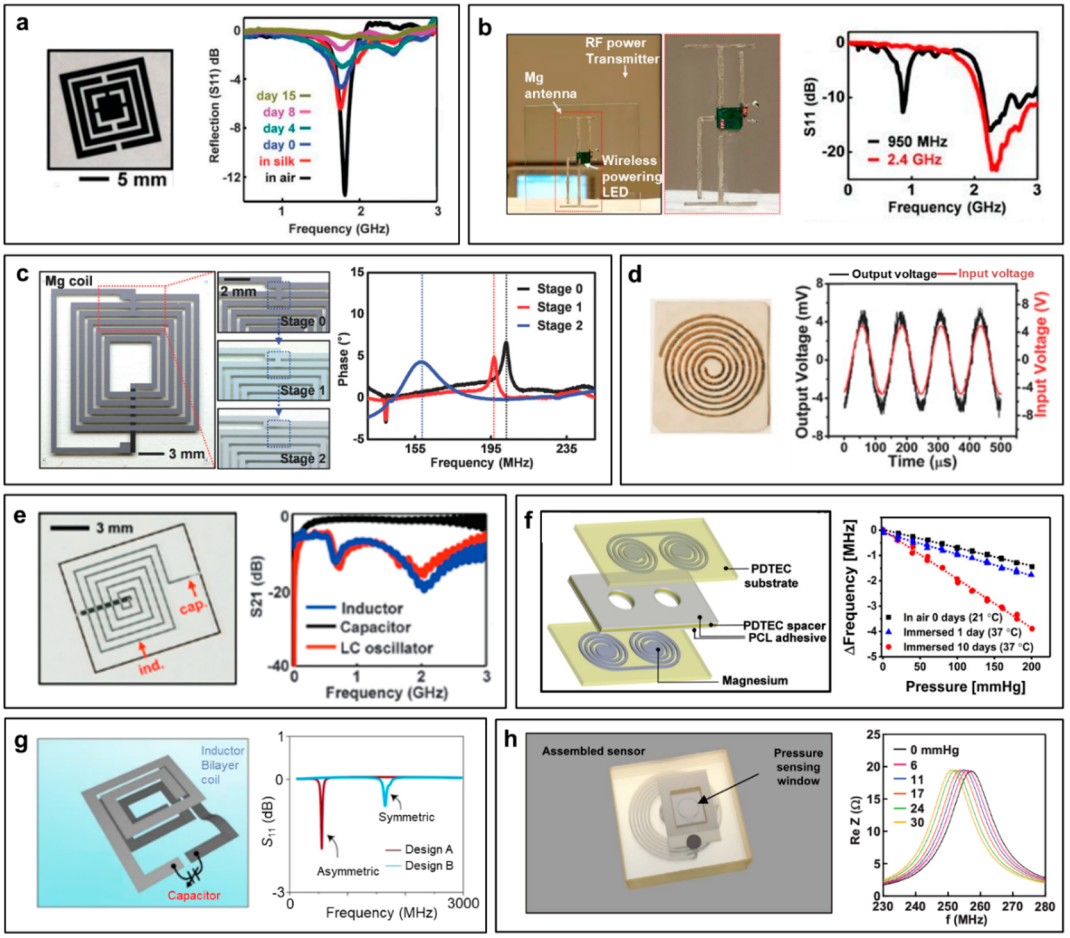

Figure 9. Representative examples of bioresorbable antenna and inductor-capacitor (LC) oscillators. (a) Left: Image of a Mg metamaterial rf antenna. Right: Resonant responses of the antenna before and after implantation.[86] Reproduced with permission from ref 86. Copyright 2012 American Association for the Advancement of Science. (b) Left: Image of a Mg antenna on a silk substrate in the process of water dissolution. Right: Measured reflection coefficient of Mg antenna operating at 950 MHz and 2.4 GHz.[126] Reproduced with permission from ref 126. Copyright 2013 Wiley-VCH. (c) Left: Image of a Mg inductor designed to transform in function via dissolution of Mg traces; magnified views of the devices at different dissolution stages. Right: Measured changes in phase response at the respective stages.[150] Reproduced with permission from ref 150. Copyright 2014 Wiley-VCH. (d) Left: Image of an antenna made of Au trace (200 nm thick) on a sugar paste substrate. Right: Output and input AC voltage when the antenna is wireless coupled to a signal generator.[162] Reproduced with permission from ref 162. Copyright 2017 Wiley-VCH. (e) Left: Image of an LC oscillator fabricated with Mg electrodes and MgO dielectrics on a silk substrate. Right: Measured scattering parameter (S_{21}) of the inductor, capacitor, and LC oscillator in 0−3 GHz.[86] Reproduced with permission from ref 86. Copyright 2012 American Association for the Advancement of Science. (f) Left: Schematic illustration of a wireless LC resonance sensor for pressure measurement. Right: Measured shifts of resonance peak in Re Z as a function of pressure.[167] Reproduced with permission from ref 167. Copyright 2020 Wiley-VCH. (g) Left: Schematic illustration of an LC oscillator that can be fabricated via one step to form a bilayer inductive coil. Right: Simulated resonate behavior (S_{11}) of two different designs.[26] Reproduced with permission from ref 26. Copyright 2018 Springer Nature. (h) Left: Exploded view of an LC circuit formed by Mg inductors/capacitor electrodes and PDTEC spacer/substrate for pressure sensing. Right: Real part of the impedance (Re Z) spectrum measured at different reading distance.[169] Reproduced with permission from ref 169. Copyright 2020 Wiley-VCH.

Specifically, a conjugated, p-type semiconducting polymer, PDPP−PD, imparts both high FET carrier mobility (~0.1−1 $cm^2\ V^{-1}\ s^{-1}$) and decomposability in acidic environments (pH 4.6) and selected solvents (e.g., chloroform, THF). Fe serves as the gate and source/drain electrodes in devices that show hole mobilities of ~0.12 $cm^2\ V^{-1}\ s^{-1}$ with on/off ratio >10^4 (Figure 7b). Directly fabricated on a cellulose film substrate, PDPP−PD based pseudo-D inverters have rail-to-rail output with sharp switching at V_{dd} = 1.9 V and large noise margins, comparable to those of conventional organic and CNT-based logic gates.

Interesting parallel efforts are in nature or food-derived organic materials for OFETs, including PBAT and hard gelatin capsules for substrates, with glucose, sucrose, lactose, adenine, or guanine for dielectrics, and perylene diimide, β-carotene, vat orange 3, vat yellow 1, or indigo as organic semiconductors.[156] Such materials can be combined to yield fully bioresorbable and even edible devices, yet their electrical properties are far from ideal, with OFET carrier mobilities in the range of ~10^{-4} to 10^{-2} $cm^2\ V^{-1}\ s^{-1}$. Subsequent results demonstrate that indigo, a highly planar but small cross-conjugated π-electron system with ambipolar charge transport characteristics and a bandgap of 1.7 eV, can yield transistors with mobilities of 10^{-2} $cm^2\ V^{-1}\ s^{-1}$ for both types of carriers (Figure 7c)[107] with threshold voltages of −1.5 to −3 V for p-channel and 4.5 to 7 V for n-channel transistors. Inverters show gains of ~105−110.

3.2. Bioresorbable Diodes

Diodes, passive two-terminal devices that only allow current to pass in one direction, can also be built in bioresorbable forms using similar materials. p−n diodes result from formation of

https://doi.org/10.1021/acs.chemrev.3c00408
Chem. Rev. XXXX, XXX, XXX−XXX

junctions between p-type and n-type semiconductors, where mismatch of their electrical potential (i.e., built-in potential) at the boundary only allows for electrons to flow from the n-type side to the p-type side upon application of a voltage (i.e., forward bias) above a threshold.

Si NM-based diodes can be achieved by patterning the introduction of p- and n-type dopants, such as those described in the previous section, into the crystal lattice. One example uses p−n junctions of this type with Mg electrodes on silk substrates (Figure 8a).[86] The $I-V$ characteristics indicate forward threshold voltages (∼0.5−0.6 V) and other properties consistent with conventional diodes formed on silicon wafers. Doping configurations that involve an intrinsic region between the n and p doped regions lead to PIN diodes, as demonstrated in silicon-based rectifiers for radio frequency wireless power transfer (Figure 8b).[126] The $I-V$ characteristics are as expected, with turn-on voltages of ∼0.7 V, forward currents of ∼1.5 mA at 1 V, and rectifying responses up to the GHz frequency range, when fabricated using modified versions of techniques developed for the semiconductor industry. Laser ablation approaches are also possible options for bioresorbable Si diodes (Figure 8c),[157] as described in section 5, but with some decrease in performance.

Additional classes of diodes, known as Schottky diodes, form at the junction between a semiconductor and a metal, to yield lower forward voltages and faster switching speeds than in many p−n or PIN devices. One example uses IGZO, Ni, and Al as semiconductor, Schottky contact, and ohmic contact, respectively,[4] on a polyanhydride substrate as shown in Figure 8d. Hydrolysis of the polyanhydride substrate in the presence of moisture generates corrosive organic acids, to trigger degradation processes for materials that are not bioresorbable under physiological conditions. These Schottky diodes show expected rectifying characteristics, and time scales for partial dissolution in the range of ∼100 h under a humidity of 75%. Related types of partially bioresorbable devices use gallium arsenide (GaAs) and Ti/Pt/Au on CNF paper substrates.[153] Bioresorbable diodes can also be formed with organic materials. As a specific example, ionic diodes composed of cationic (n-type) and anionic (p-type) cellulose nanocrystals (CNCs)-agarose gels demonstrate good rectification behavior from a fixed junction in between.[158]

p−n or PIN junctions designed to optimize their sensitivity to light can be used as photodiodes. Examples include the use of Si NM-based devices for image capture and spectroscopic characterization.[36,86] Additional opportunities are in lithographically defined silicon structures in photodiodes for neural modulation,[159] where laser irradiation can generate photovoltaic responses to regulate neural activity (Figure 8e). Forming such devices in partially bioresorbable forms on polyethylene terephthalate (PET) substrates supports extended lifetimes for *in vivo* studies. Use of PLLA−PTMC substrates allows for complete bioresorption.

Light emitting devices represent additional uses of bioresorbable diodes, of relevance in biomarker tracking, optogenetics, photodynamic therapies, and others. Organic LEDs that exploit derivatives of the vitamin riboflavin, namely riboflavin tetrabutyrate, as emissive layers, ITO/PEDOT:poly(styrene sulfonate) (PSS) as electrodes, and glass as substrates are of interest as partially bioresorbable devices with the ability to reach maximum luminance of 10 cd m^{-2} and external quantum efficiencies (EQE) of 0.02%.[160] Fully bioresorbable inorganic LEDs can be constructed using the direct bandgap semiconductor ZnO, with Mo as electrodes, and Si as a substrate.[17] Pulsed laser deposition (PLD) facilitates the growth of high-quality ZnO with both near-band-edge and defect emission, suitable for use in white LEDs (forward threshold = 5 V, Figure 8f). Bioresorbable filters based on Fabry−Perot cavities can be added to these devices as the basis of red, green and blue LEDs.

3.3. Bioresorbable Antennas and Inductor−Capacitor (LC) Circuits

3.3.1. Antennas. Antennas are among the most important, yet the simplest, components in radiofrequency (RF) systems. Such antennas effectively convert electrical signals into radio waves (and vice versa) for wireless communications and power transfer. Initial reports describe Mg-based devices on silk substrates for wireless powering and sensing,[86,126,150] as shown in Figure 9a for the case of a metamaterial RF antenna as a signal transducer.[86] A bioresorbable wideband dipole antenna that operates at ∼2.4 GHz and ∼950 MHz enables operation (with distance >2 m) of a red LED via harvesting of power from an external RF transmitter (Figure 9b).[150] Dissolution of local interconnects in an antenna can further trigger functional transformation in the form of shifts in resonant frequency (from 206 MHz at stage 0, to 196 MHz at stage 1, to 159 MHz at stage 2), as a physically tunable system (Figure 9c).[150] In addition to Mg on silk,[139] a range of other materials and designs are possible for fully or partially bioresorbable systems, including Mo on PLGA[161] and Cu on polyanhydride.[4] Another interesting example involves Au traces on a sugar paste substrate[162] (Figure 9d). Integration of these and related types of antennas with other components serve as the basis for a broad scope of wireless devices, including those for drug delivery, therapeutic stimulation, and others, as described in subsequent sections.[163]

3.3.2. LC Circuits. An LC circuit combines an inductor and a capacitor to yield an oscillator with resonant frequency (f) determined by the inductance (L) and capacitance (C) according to

$$f = \frac{1}{2\pi\sqrt{LC}}$$

Changes in either of these parameters (L or C) induce shifts in the resonant frequency, in ways that can be detected remotely in a passive wireless fashion. Figure 9e illustrates examples that use Mg inductive coils and capacitors formed by Mg electrodes and MgO dielectrics on silk substrates,[86] with operating frequencies up to ∼3 GHz. Miniaturized LC resonators can also be constructed with other bioresorbable metals (e.g., Mg, Fe, Zn, and Mg and Fe alloys) and with various polymers (e.g., PLLA−PPy and PCL−PPy).[164] In two relevant examples, Zn or Zn/Fe bilayer conductors[165,166] patterned on PLLA or PLGA substrates provide the basis for both inductive coils and capacitor electrodes. Here, a folding technique with a PCL spacer as an adhesive defines the capacitor to complete the LC circuit, with a resonant frequency in the range of tens of MHz. The Fe stimulates galvanic corrosion of Zn in saline environments, to accelerate the process of bioresorption. In related work, LC circuits as pressure sensors utilize capacitors formed by lamination of two Mg-coated films of PDTEC with a spacer of PDTEC and an adhesive of PCL (Figure 9f).[167] A more sophisticated design approach involves Mg bilayer coils insulated by a layer of PLLA (2 inductors), Mg electrodes that sandwich a PGS dielectric layer molded into microstructured arrays of pyramids as the pressure sensing component (2 capacitors connected in parallel), and 10 μm thick layers of POMaC and PHB/PHV as the packaging.[26] Different choices of

https://doi.org/10.1021/acs.chemrev.3c00408
Chem. Rev. XXXX, XXX, XXX−XXX

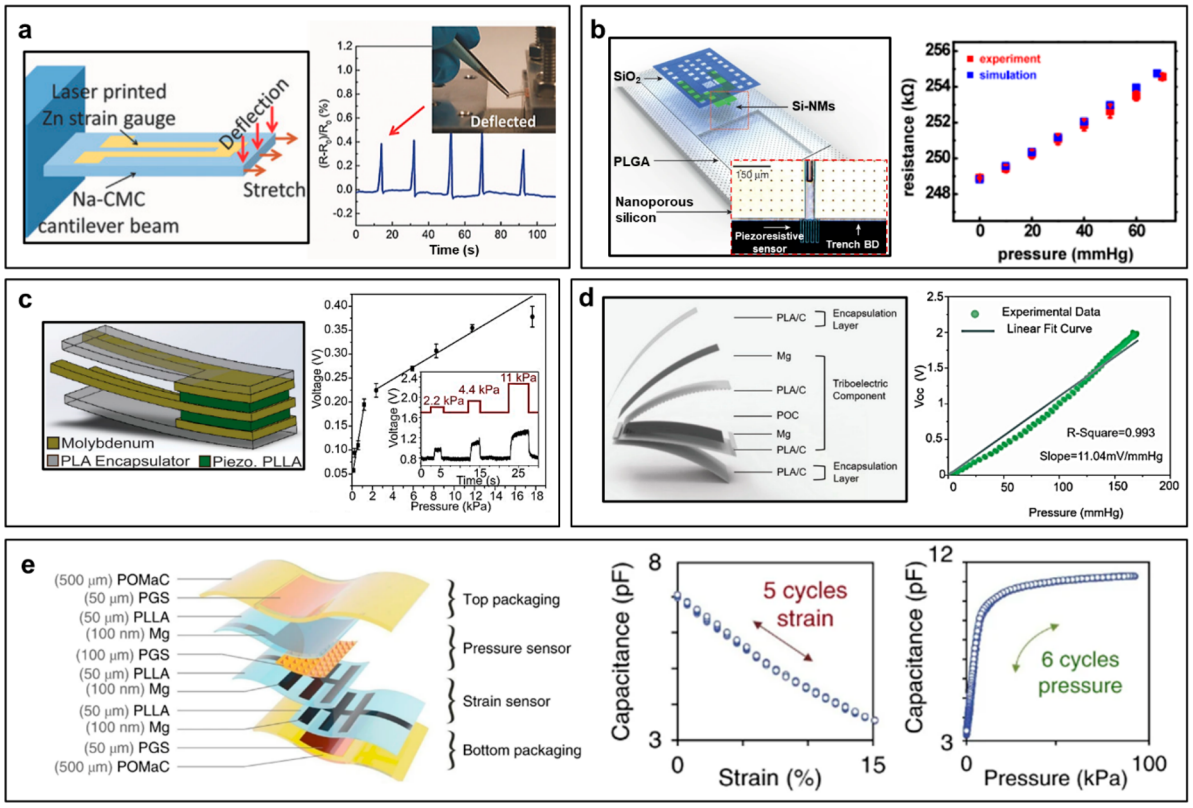

Figure 10. Representative examples of bioresorbable physical sensors (strain and pressure). (a) Left: Schematic illustration of strain measurements of laser printed resistive Zn strain gauges on Na-CMC substrate subjected to stretch or deflection. Right: Response of the resistive strain gauge under deflection (as shown in inset).[170] Reproduced with permission from ref 170. Copyright 2017 Wiley-VCH. (b) Left: Schematic illustration of a Si NM piezoresistive pressure sensor. Right: Calibration curve of the Si NM piezoresistive sensor.[9] Reproduced with permission from ref 9. Copyright 2016 Springer Nature. (c) Left: Schematic illustration of a PLLA piezoelectric pressure sensor. Right: Calibration curve of the PLLA piezoelectric pressure sensor.[174] Reproduced with permission from ref 174. Copyright 2018 United States National Academy of Sciences. (d) Left: Exploded view of a PLA-chitosan based triboelectric pressure sensor. Right: Calibration curve of the triboelectric pressure sensor.[178] Reproduced with permission from ref 178. Copyright 2021 Wiley-VCH. (e) Left: Exploded view of a multifunctional capacitive strain and pressure sensor based on bioresorbable polymers POMaC, PGS, PLLA as packaging/dielectrics, and Mg as electrodes. Right: Response curves for strain (left) and pressure (right) under cyclic loading, respectively.[181] Reproduced with permission from ref 181. Copyright 2019 Springer Nature.

designs in the Mg coils lead to a range of resonant behaviors (Figure 9g), demonstrated useful for sensing of arterial blood flow, but with fast rates of dissolution that support stable operation for only a few minutes *in vivo*.

Advanced encapsulation strategies can extend the lifetimes of bioresorbable LC circuits, and other systems, for practical use. Bioresorbable wax, as described in section 2, can serve as an effective barrier to biofluids, for stable operation over periods of several days or longer. One example reports minimal drift in baseline or sensitivity in an LC circuit for temperature sensing, over ∼4−6 days,[168] followed by rapid dissolution of constituent materials. Here, Mg forms the inductive coil and electrodes of the capacitor, and PEG serves as the dielectric. Another device integrates a barrier of Si_3N_4 (2 μm thick) over a Zn flexible electrode for a capacitive LC pressure sensor.[169] Hysteresis-free responses to applied pressure are possible via measurements of shifts in resonant frequency in the range of ∼100−300 MHz (Figure 9h).[168] Additional details related to the sensing performance, as well as their biomedical applications appear in following subsections.

3.4. Bioresorbable Sensors

Combining the electronic components described in the previous subsections with bioresorbable sensors leads to vast opportunities in temporary implants of various types, designed to monitor natural body processes of interest, and then to simply disappear without adverse effects. This subsection discusses sensors that operate on physical, chemical, and optical principles.

3.4.1. Physical Sensors. Perhaps the simplest physical sensors are strain gauges, in the form of devices with resistances that change with applied strain. Metal traces, often in serpentine geometries, on deformable substrates represent a primitive but widely used example, usually formed by some combination of cleanroom processing approaches or by advanced methods described subsequently such as in the laser sintering of Zn nanoparticle (NP) suspensions to define traces of Zn on a Na-CMC substrate.[170] The high crystallinity of the Zn formed in this way imparts high conductivity (∼1.124×10^6 S m^{-1}) and sensitivity to strain in the reported bioresorbable strain gauge comparable to those in most conventional devices (Figure 10a).

Semiconductor materials offer enhanced levels of performance in strain sensing through the piezoresistive effect, as demonstrated in devices formed with Si NMs. In one case,[9] a Si NM in a serpentine shape defines a strain gauge on the edge of a membrane that forms an air cavity (30−40 μm deep) defined by an etched feature of relief on a substrate of nanoporous Si. Deflection of the membrane due to changes in pressure (Figure 10b) can be determined through changes in resistance of the

https://doi.org/10.1021/acs.chemrev.3c00408
Chem. Rev. XXXX, XXX, XXX−XXX

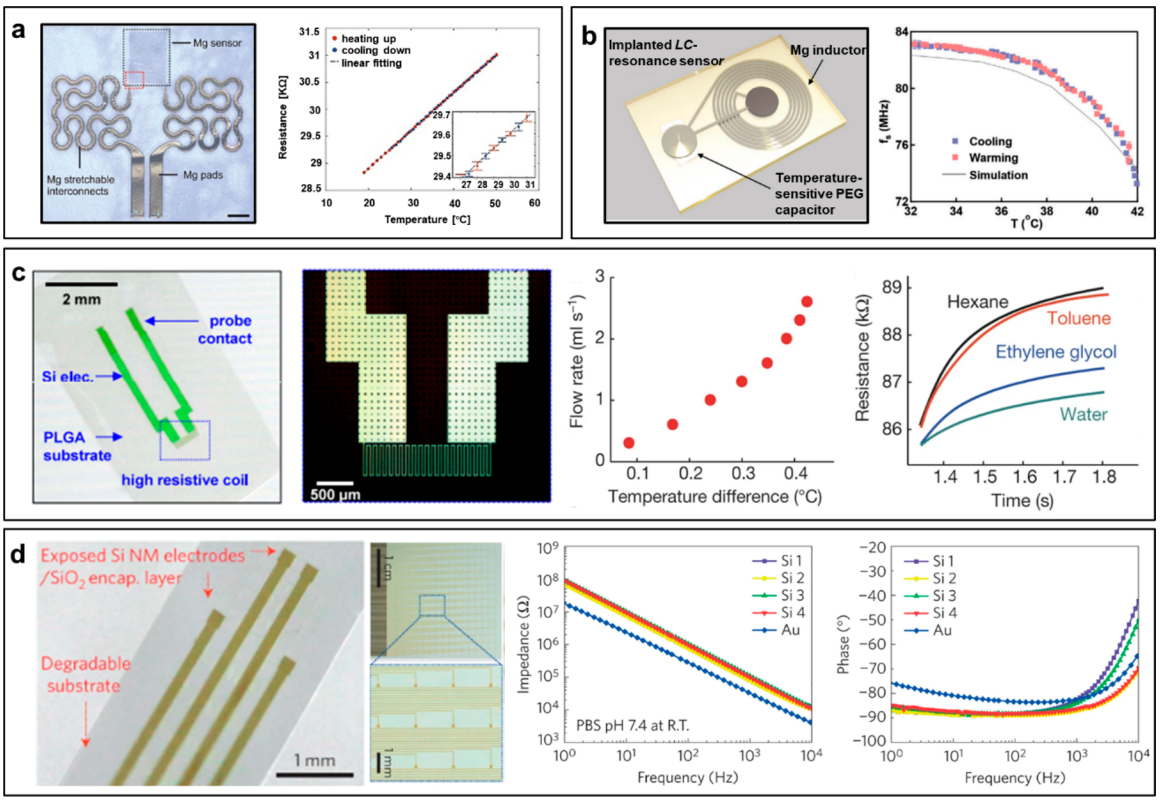

Figure 11. Representative examples of bioresorbable physical sensors (temperature, flow, and biopotential). (a) Left: Image of Mg based resistive temperature sensor with Peano fractal shaped interconnects on a PBAT substrate. Right: Calibration curve of the resistive temperature sensor.[182] Scale bar: 1 mm. Reproduced with permission from ref 182. Copyright 2017 Wiley-VCH. (b) Left: Schematic illustration of an LC capacitive temperature sensor with PEG dielectric. Right: Calibration curve of the capacitive temperature sensor.[168] Reproduced with permission from ref 168. Copyright 2020 Wiley-VCH. (c) Left: Schematic illustration of a Si NM temperature sensor. Middle-left: magnified view of a dense serpentine Si NM structure for thermally induced resistive response. Middle-right: The difference in temperature measured by two separate Si-NM temperature sensors with a Si-NM element for Joule heating placed in between, allowing assessment of flow rate. Right: Measurements of thermal conductivity and heat capacity of selected materials. The graph shows time-dependent changes in temperature upon actuation of Joule heating in devices immersed in different liquids. The coefficients of thermal conductivity (κ, measured through the rate of resistance change) of hexane, toluene, ethylene glycol, and water are 0.12, 0.13, 0.26, and 0.60 W m^{-1} K^{-1}, respectively.[9] Reproduced with permission from ref 9. Copyright 2016 Springer Nature. (d) Left: Image of a highly doped Si neural electrode array on a PLGA substrate with magnified view of the electrodes. Middle and Right: Electrochemical impedance spectra, magnitude (Middle) and phase (Right), measured at four different recording sites in an array configured for ECoG.[125] Reproduced with permission from ref 125. Copyright 2016 Springer Nature.

strain gauge. This same type of sensing principle provides the basis for other device platforms for pressure monitoring.[21,171]

Piezoelectric materials provide additional opportunities. For example, PLLA exhibits shear piezoelectricity that arises from its C═O side chains.[172] The low dielectric constant, combined with a piezoelectric response (~5−12 pC N^{1-}), enables efficient modes for physical sensing, as well as for energy conversion, with performance comparable to that of nonbioresorbable piezoelectric polymers, such as polyvinylidene difluoride (PVDF).[173] Sandwiching a thin sheet of PLLA (20 μm thick) between Mo or Mg electrodes yields a flexible and fully bioresorbable pressure/force sensor.[174] An integrated charge amplifier circuit converts the response into a voltage for data capture (Figure 10c). Advanced versions use electrospinning to form PLLA nanofibers with high crystallinity (70−88%), to reach piezoelectric constants of ~19 pC N^{1-}.[175] Other options include blends of piezoelectric β-phase glycine (d_{16} = 174 pm V^{-1}) and chitosan.[176] Sensors fabricated with this material offer high sensitivity to pressure (~2.82 mV kPa^{-1}), good tolerance to cyclic loading (~9000 cycles), and device-level bioresorbability when integrated with Mg electrodes.

Other mechanisms for pressure sensing include the triboelectric effect, achieved with bioresorbable materials. A basic device contains a pair of electrodes (Mg or Fe) and a triboelectric material (PLA−chitosan or PLA−chitosan−sodium alginate).[177,178] An air gap separates the triboelectric layer and one of the two electrodes. Contact between them generates static polarized charges due to contact electrification. Separation of these two materials by a mechanical force generates a potential drop. This mechanism converts pressure changes into electrical signals. Nanopatterning the surface of the PLA−chitosan triboelectric layer increases the surface area, leading to improved sensitivity (~11−22.61 mV $mmHg^{-1}$), service efficiency (5.95%), and durability (>450 000 cycles) (Figure 10d).

Related changes in capacitance can be measured directly, in structures that do not require contact electrification. As a specific example, an elastomeric dielectric of PGS patterned into a 2D array of square pyramids placed between Fe−Mg electrodes defines a collection of air gaps that can be compressed by applied pressure. Encapsulation in PHB/PHV yields a bioresorbable device for capacitive pressure monitoring, with a focus on measurements of pulse wave velocity at the surface of an

https://doi.org/10.1021/acs.chemrev.3c00408
Chem. Rev. XXXX, XXX, XXX−XXX

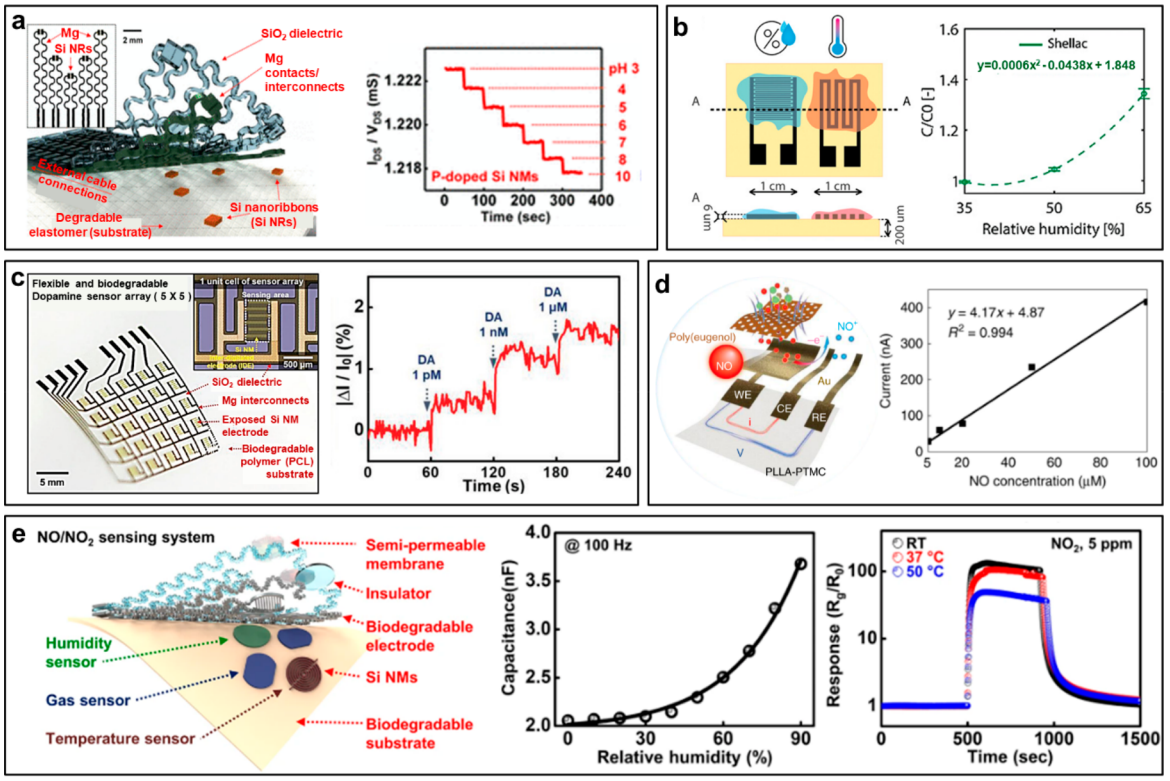

Figure 12. Representative examples of bioresorbable chemical sensors. (a) Left: Exploded view of a doped Si NR pH sensor. Right: Measurement of conductance as a function of surrounding pH for P-doped Si NMs.[147] Reproduced with permission from ref 147. Copyright 2015 American Chemical Society. (b) Left: Schematic illustration of a capacitive humidity/temperature sensor on a shellac substrate, where egg albumin is coated onto interdigitated electrodes for humidity sensing. Right: Capacitive response of the humidity sensor.[192] Reproduced with permission from ref 192. Copyright 2022 Wiley-VCH. (c) Left: Image of an array of multiplexed electrodes for mapping of dopamine concentration, with magnified view of a Si NM interdigitated electrode (inset). Right: Measured real-time conductance change of the Fe^{3+}_CPPy NP-coated electrode in response to dopamine input.[193] Reproduced with permission from ref 193. Copyright 2018 Wiley-VCH. (d) Left: Exploded view of a NO sensor, with poly(eugenol) coated working electrode on a PLLA−PTMC substrate. Right: Linear sweep voltammetry of the sensor detecting NO in PBS solution.[195] Reproduced with permission from ref 195. Copyright 2020 Springer Nature. (e) Left: Exploded view of a NO_x sensor with integrated gas, temperature, and humidity sensor on a PLGA substrate. Middle: Capacitive response of the humidity sensor. Right: Resistive response of the NO_2 sensor.[196] Reproduced with permission from ref 196. Copyright 2020 Springer Nature.

artery.[179] The sensitivity, S (defined as $S = \delta(\Delta C/C_0)/\delta p$) changes from a high value, ∼0.76 kPa^{-1} in low pressure regime (p < 2 kPa) to lower magnitude of ∼0.11 kPa^{-1} at higher pressure (2 kPa < p < 10 kPa), comparable with that in devices fabricated using nonbioresorbable counterparts (e.g., dielectric of microstructured polydimethylsiloxane (PDMS).[180] Overlaying a bioresorbable strain sensor on top of the pressure sensor imparts an additional modality in physical sensing (Figure 10e).[181] One such sensor involves a similar parallel-plate capacitor design for pressure sensing with a sensitivity comparable to that of the previous example, namely ∼0.7 kPa^{-1} in low pressure regime (p < 1 kPa) and 0.13 kPa^{-1} at higher pressures (5 kPa < p < 10 kPa). The sensor exploits thin film comb-shaped Mg electrodes, configured against each other, resulting in a uniaxial strain that is also measurable via variation in relative capacitance ($\Delta C/C_0$). The reported sensitivity is ∼50% for an applied strain of ∼15% with good linearity and durability (>20 000 cycles).

section 3.3.2 reviews examples of LC circuit-based pressure sensors that rely on the deflection of flexible diaphragm electrodes to induce changes of capacitance and thus shifts in resonant frequency. The performance of these systems depends on the details of their construction. Microfabricated sensors with Zn (or Zn/Fe bilayer) for L and C components embedded in PLGA show sensitivities of ∼40 kHz kPa^{-1} in air and saline solution, within the range of 0−30 kPa and with a baseline of ∼30−50 MHz.[165,166] Miniaturized pressure sensors for arterial blood flow monitoring exhibit two modes of operation, contact and noncontact modes, as a result of fringe-field effect in the capacitor.[26] Detailed studies indicate a maximum direct contact sensitivity (= $\Delta C/C_0$) of ∼14% (up to 20 kPa) and a noncontact sensitivity of ∼7% with a displacement of up to 800 μm) in response to objects in close proximity. Wax encapsulated LC pressure sensors support reliable long-term measurements.[169] Advanced designs offer sensitivity from 40 kHz $mmHg^{-1}$ to ∼200 kHz $mmHg^{-1}$, with a resolution of 1 mmHg.

Temperature represents another important mode in physical sensing, with broad utility in clinical medicine. Resistive sensing of temperature is one of the most straightforward approaches, given that the relationship between resistance and temperature in most metals is highly linear over a range of relevance for most applications considered here. One example uses thin layers Si_3N_4 and SiO_2 (16 μm thick) to encapsulate Mg resistive sensing elements (10 μm wide, 250 nm thick) in the neutral mechanical plane, to eliminate changes in resistance that might otherwise occur due to bending induced strains.[182] In this example, a commercially available, tear resistant bioresorbable polymer, PBAT encases the device structure to provide mechanical robustness. The Mg interconnects adopt a Peano fractal design to confer stretchability (Figure 11a).[183] The

https://doi.org/10.1021/acs.chemrev.3c00408
Chem. Rev. XXXX, XXX, XXX−XXX

resulting device exhibits a linear response over the range of ~20−50 °C, with a sensitivity of ~70 Ω K^{-1}, corresponding to ~0.2% K^{-1} in relative value, as expected based on the properties of Mg. Other examples of temperature sensing based on these mechanisms exploit Zn traces on galactomannan membranes,[184] and Mg traces on PLA substrates, the latter integrated onto a bioresorbable smart stent.[35] In addition to metals, Si based semiconductor devices can also serve as temperature sensors based on their nonlinear response to changes in temperature. One such example involves a Si NM diode, where the forward-direction voltage drop depends strongly on temperature. When measured for a given current output, such devices show sensitivity of ~−2.23 mV $°C^{-1}$,[86] consistent with the behavior of conventional, nonbioresorbable devices.[185]

Another approach to temperature sensing relies on the variable dielectric properties of insulators used in capacitors, as is common in nonbioresorbable devices.[186−188] An example of a fully bioresorbable sensor of this type exploits wireless readout from LC resonant circuit, as introduced previously.[168] In that case, PEG, a bioresorbable polymer that has a strong temperature dependent dielectric constant near body temperature (~34−42 °C), serves as the basis for a parallel-plate capacitor. Changes in temperature cause shifts in the resonant frequency, which enable sensing with an accuracy of 0.5 °C (Figure 11b). *In vivo* experiments in subcutaneous regions and the intracranial spaces of small animal models validate the capability of this type of device to track temperature wirelessly in freely behaving subjects, in real time.

Resistive temperature sensors can also be used as local sources of thermal power, through processes of Joule heating that follow from passage of electrical current. Measuring changes in resistance while operating the device as a Joule heater can yield information on the thermal transport characteristics of surrounding materials.[189] The dependence of these parameters on micro- or macroscale flow enables additional sensing opportunities. A representative study describes a flow sensor that exploits one Si NM as thermal actuator and two additional Si NMs, placed before and after the actuator along the flow direction, as temperature sensors (Figure 11c).[9] Upon generation of heat, the temperature difference between the sensors quantitatively correlates to flow; time dynamics of the temperature increase in either sensor translates to the thermal transport properties of surrounding fluid or tissue, thus yielding measurements of thermal conductivity or diffusivity (Figure 11c).

Monitoring of biopotentials associated with neural activity or other biological processes represents a final example of physical sensing presented in this subsection. As a specific case, short-term (approximately 1−2 weeks) ambulatory intracranial electrocorticography (ECoG) recording can help to localize seizures for surgical resection procedures to treat epilepsy.[190] Sensing in these and other instances can be accomplished most simply by use of conductive electrodes placed at the tissue interface. A multiplexed, fully bioresorbable system of this type using Mo electrodes enables high-speed spatiotemporal mapping of neural activity at the cerebral cortex.[125] This passive array includes 256 independent channels, in a 16 × 16 configuration, with an overall area of 3 cm × 3.5 cm (Figure 11d). Highly doped Si NMs represent additional options for sensing electrodes, with impedances similar to those possible with Au. Details related to neural recording appear in section 6.

3.4.2. Chemical Sensors. Quantitative detection of chemical substances in biological systems is of high interest. Potentiometric sensors of pH can be constructed using boron-doped Si nanoribbons (NRs), chemically modified by 3-aminopropyltriethoxysilane (APTES) for enhanced sensitivity.[147] The resulting surface presents both $-NH_2$ and −SiOH groups, which undergo protonation to $-NH_3^+$ at low pH and deprotonation to $-SiO^-$ at high pH. Measured changes in quiescent conductance (I/V) of the functionalized Si NRs in comparison to a Ag/AgCl reference electrode (nonbioresorbable) define the pH across a broad range, from 3 to 10 in a buffer solution (Figure 12a). Other studies exploit electrostatic gating associated with the surrounding solution, which alters the conductance of phosphorus-doped Si NR electrodes, for sensing in the range of 2−10,[9] and with ZnO electrodes for a range of 1−12.[162] Another report introduces a nanostructured porous silica scaffold coated with polyelectrolytes labeled with a pH-insensitive rhodamine-B fluorophore. This partially bioresorbable device returns pH via measurements of changes in fluorescence[191] that result from swelling or deswelling of the polyelectrolyte, across a range of pH from 4 to 7.5.

Humidity sensors represent another basic type of chemical sensor. Several examples rely on capacitive effects. One case involves an interdigitated carbon electrode printed on a shellac substrate for capacitive sensing of both humidity and temperature (Figure 12b).[192] Coated with egg albumin as a responsive layer, the sensor demonstrates high sensitivity (~0.011% RH^{-1}) to relative humidity (RH) from 35% to 65% with a response time of 12−100 s.

Dopamine is an important neurotransmitter that controls pathways in the motivational component of reward-motivated behavior. Detection of dopamine with bioresorbable devices can be achieved by coating NPs of Fe and carboxylated polypyrrole (Fe^{3+}_CPPy) as an active sensing element on heavily boron-doped arrays of Si NM electrodes.[193] The sensing mechanism involves absorption of dopamine molecules onto the CPPy surface of the hybrid Fe^{3+}_CPPy NPs via p−p interactions. Dopamine accumulated in this way oxidizes to form dopamine-*o*-quinone, thus generating electrons that transfer to the Si NMs to produce a measurable current (Figure 12c). Other forms of nonspecific dopamine sensors utilize electrochemical approaches in partially bioresorbable forms, with sericin protein photoresist (SPP)-doped PEDOT: PSS, Ag/AgCl, and Pt as working (WE), reference (RE), and counter electrode (CE), respectively.[71] By immobilizing the SPP-PEDOT:PSS electrode with enzymes, such as glucose oxidase (GOx), the same device can function as a glucose sensor. Exploiting similar electrochemical means of sensing, a more recent research report describes continuous glucose monitoring (CGM) using a hybrid device that comprises a wearable control circuit (nonbioresorbable) and a bioresorbable implantable sensor,[194] with screen-printed GOx coated Zn, Mo−W, and Mo as WE, RE, and CE, respectively. An additional Zn sacrificial electrode (SE) compensates effects that occur during slow biodegradation, thereby enabling accurate yet prolonged glucose sensing within a wide range of 0−25 mM (sensitivity = 0.2458 μA mM^{-1}) over 5−7 days.

Development of nitric oxide (NO_x) sensors is another area of activity, proven to be important in signaling neurotransmission, immune responses, and articular circulation. A recent study reports on ultrathin electrodes (total thickness <500 nm) formed by patterned Au NMs on PLLA−PTMC substrates with coatings of biocompatible poly(eugenol) as a selective membrane for passage of NO by hydrophobic repulsion, ionic interaction, and molecular exclusion in solution.[195] Poly-

https://doi.org/10.1021/acs.chemrev.3c00408
Chem. Rev. XXXX, XXX, XXX−XXX

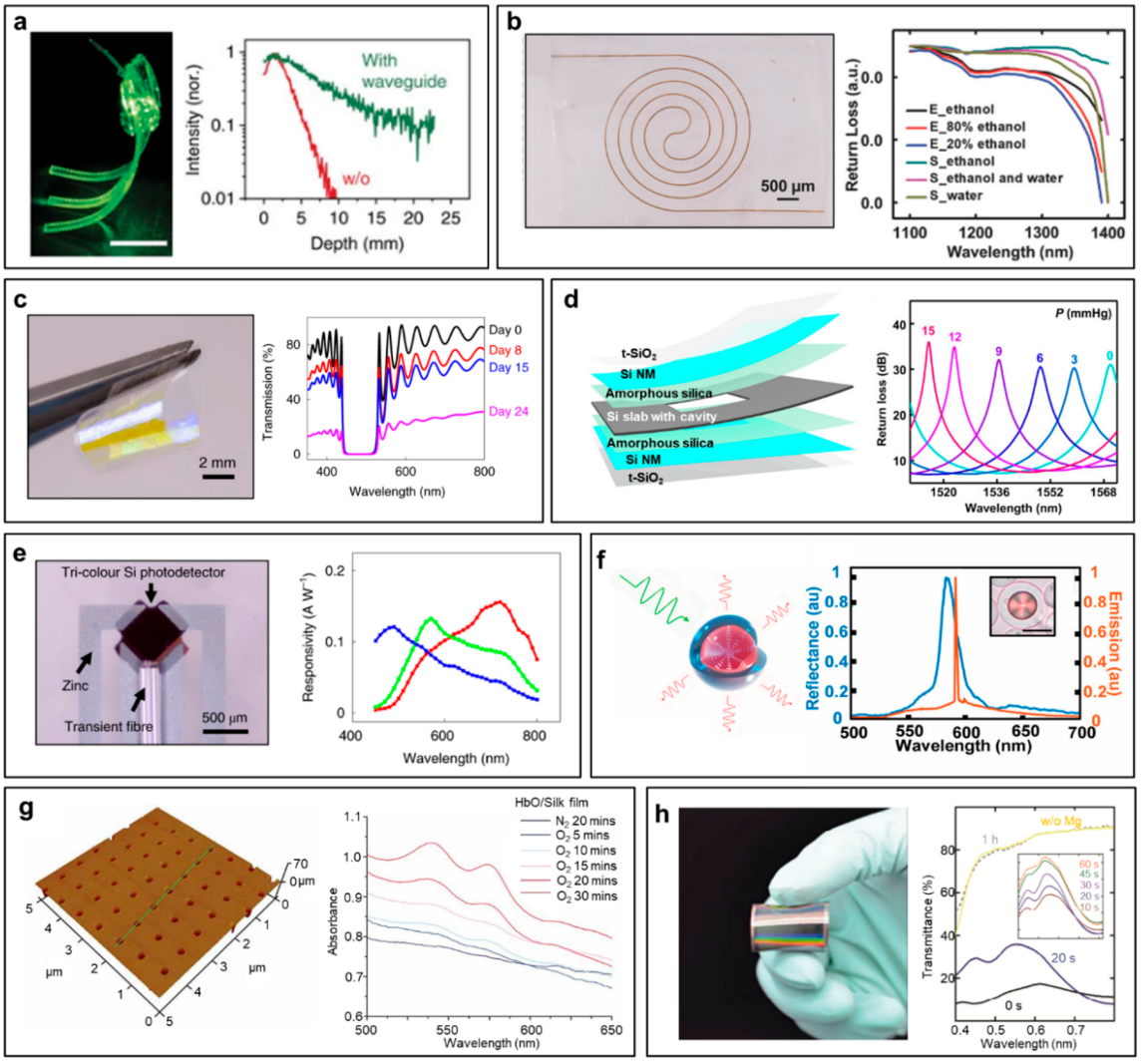

Figure 13. Representative examples of bioresorbable optical components and sensors. (a) Left: A PEG hydrogel waveguide array carrying green laser light. Scale bar = 10 mm. Right: Power loss as a function of waveguide width in different media.[198] Reproduced with permission from ref 198. Copyright 2016 Springer Nature. (b) Left: Image of an optical waveguide sensor with Si core and PLGA cladding, with Si core exposed on top and side surfaces. Right: Experimental and simulated transmission spectra of the optical sensor in water/ethanol solution.[201] Reproduced with permission from ref 201. Copyright 2018 Wiley-VCH. (c) Left: Image of an optical filter formed by layered SiO_x/SiN_y films. Right: Transmission spectra showing transience of the optical filter in PBS.[202] Reproduced with permission from ref 202. Copyright 2021 Springer Nature. (d) Left: Schematic illustration of a Fabry−Perot interferometer (FPI) composed of SiO_2 encapsulation, Si NM, amorphous silica adhesion, and silicon slab with cavity. Right: Optical spectra collected from the FPI sensor under different pressures.[203] Reproduced with permission from ref 203. Copyright 2019 American Association for the Advancement of Science. (e) Left: Image of a spectrometer that incorporates a tricolor Si NM photodetector with three separate junctions, four Zn electrodes, and a PLGA optic fiber for light coupling. Right: Measured photoresponses of the three junctions as a function of wavelength. The measured responsivity peaks are 490, 570, and 720 nm, respectively.[36] Reproduced with permission from ref 36. Copyright 2018 Springer Nature. (f) Left: Schematic illustration of a gelatin encapsulated, dye-doped LC droplet photopumped laser. Right: Bragg reflectance due to molecular helix and corresponding band-edge lasing pumped at 532 nm, with single particle under cross polarized illumination (inset).[204] Scale bar: 50 μm. Reproduced with permission from ref 204. Copyright 2021 American Chemical Society. (g) Left: AFM image of a nanoimprinted silk grating film. Right: Spectral response of silk doped with lysed red blood cells.[205] Reproduced with permission from ref 205. Copyright 2010 Wiley-VCH. (h) Left: Image of a Mg coated polyurethane nanopost array as plasmonic pad. Right: Transmission spectra showing the transience of the Mg plasmonic pad as indicator of water soaking time.[209] Reproduced with permission from ref 209. Copyright 2018 Tsinghua Press.

(eugenol) electrochemically deposited (with a proper eugenol concentration of ~10 mM) on the working electrode balances a trade-off between potential interference from associated chemicals (e.g., glucose, sodium nitrite/nitrate, ascorbic acid, uric acid, etc.) and NO sensitivity, to realize a performance of 4.17 nA μM^{-1} for NO concentrations in the range of 5−100 μM, with fast response time (<350 ms) and prolonged stability (>7 days) in PBS at 37 °C (Figure 12d). The device is partially bioresorbable, where clearance of trace amounts of Au and poly(eugenol) can occur through phagocytosis and renal metabolization. Nonspecific sensing of both NO and NO_2 is possible via direct adsorption and reaction between the NO_x gas using interdigitated P-doped single-crystalline Si NM electrodes, without additional physical or chemical treatment of the Si NM.[196] The sensing process relies on changes in electrical properties of an n-type electrode from variations in the depletion layer on its surface through adsorption and reaction with oxidizing gas molecules, such as NO_x (gas) + $e^- \rightarrow NO_x^-$ (ads).

https://doi.org/10.1021/acs.chemrev.3c00408
Chem. Rev. XXXX, XXX, XXX−XXX

The reported sensing range and sensitivity are ~0.1−5 ppm and ~20 ppb, respectively, at room temperature, with fast response (~30 s) and recovery (~60 s). Integration with temperature and humidity sensors can help compensate for effects related to ambient conditions (Figure 12e).

3.4.3. Optical Sensors and Optical Components. Optical technologies provide capabilities that complement those of physical and chemical sensors. Delivering and receiving optical signals within biological tissues requires specialized components that can transmit/collect light of desired intensity/wavelengths to targeted regions. Optical fiber waveguides are a good option, in designs that include a high refractive index (n) core surrounded by a low refractive index cladding to minimize propagation losses. One of the earliest reports of a bioresorbable optical waveguides includes two steps of mold casting to define a silk fibroin core (n = 1.54) and a silk hydrogel cladding (n = 1.34).[197] The resulting multimodal fibers (with diameters of ~2−3 mm) have average losses (~2 dB cm^{-1}) comparable to those of other polymeric waveguides (~0.02−5.00 dB cm^{-1}). Patterning synthetic polymers (e.g., PLGA, PLA, PVP, PEG, etc.) directly without a cladding can yield core-only waveguides for interfacing with skin, due to its relatively low refractive index (n = 1.38−1.44). Alternative schemes use melt processing, solvent casting, and polymer photo-cross-linking, followed by laser cutting, to fabricate slab-shaped waveguide or arrays.[198] Compatible with a portfolio of synthetic or biopolymers, including PLGA, PLA, PVP, PEG hydrogel, and silk fibroin, this scheme permits light delivery to deep tissue (>1 cm) using mm scale diameter waveguides with relatively low loss (<2 dB cm^{-1}) (Figure 13a). Other examples include thermal drawing to form PLLA and PLGA fibers from a melt,[199] thermal drawing of PLGA followed by dipping into a sodium alginate to form a core-cladding structure,[36] comolding of air hole claddings around an agarose core,[199] and coextrusion printing of DL-dithiothreitol (DTT)-PEGDA (DTT-PEGDA) and pluronic as core and cladding, respectively.[200]

Key drawbacks of polymer-based waveguides are their susceptibility to swelling and their limited contrast in refractive indices. Inorganic alternatives can be fabricated by photolithography with monocrystalline Si (n = 3.48) derived from wafer sources, to form filamentary cores subsequently laminated between sheets of PLGA (n = 1.44) as cladding layers.[201] These Si-based waveguides (with core dimensions of ~50 μm × 1500 nm and length of over 50 cm) allow for full spectral characteristics of interfacing media (Figure 13b).

Bioresorbable optical filters can be formed in reflecting or absorbing structures. In the former, multilayer stacks of SiO_x and SiN_y with controlled thicknesses selectively transmit light of different wavelengths. One such example involves deposition of such a multilayer (15 pairs of SiO_x/SiN_y nanomembranes) on a sacrificial Si substrate, then releasing it and encapsulating with PLGA.[36,202] Spectroscopic studies indicate excellent performance, consistent with expectation from optical modeling (Figure 13c). Fabry−Perot optical filters can be formed by selective thinning of the device layer Si on a SOI wafer via reactive ion etching, HF etching to remove the underlying SiO_2 layer and release to yield freestanding Si NM (<100 nm thick) that can be transferred to sheets of PLGA.[17,202] Reflections from the top and bottom surfaces of the Si NM lead to Fabry−Perot resonances with spectral characteristics determined by the thickness. Similar Fabry−Perot structures can serve as interferometers (FPIs), where a Si slab with an etched relief structure and a capping Si NM responds to changes in surrounding pressure in ways that can be determined by measurements of the reflection spectra.[203] (Figure 13d).

A spectrometer is one of the most popular analytical tools for optical sensing. A recent report describes a simple bioresorbable spectrometer that consists of a foundry-produced tricolor Si NM-based photodetector, a thermally drawn PLGA fiber optic probe for light delivery, and four Zn metal electrodes for electric readout (Figure 13e).[36] The four n-/p-doped layers of the photodetector, when vertically aligned, form three junctions that show excellent rectifying behaviors with dark currents of 3.24×10^{-2}, 1.52×10^{-1}, and 9.87×10^{-3} μA, and responsivities of 0.15, 0.15, and 0.11, respectively. The penetration depth of light (with wavelengths between 400 and 1000 nm) in Si increases with wavelength, thereby enabling peak responsivities for corresponding junctions at wavelengths of 490, 570, and 720 nm, respectively.

Advanced bioresorbable optical sensors include tunable photopumped lasers formed by gelatin encapsulated, dye-doped cholesteric liquid crystal (CLC) microdroplets with internal radial-helical molecular director.[204] The associated radially periodic variations in refractive index induce a photonic band gap/Bragg reflection for circularly polarized light, thus permitting light emission at a different wavelength (Figure 13f). Quantitative measurements of laser-induced heating yield different modes of operation for temperature and thermal transport sensing. The former relies on the temperature dependence of the molecular helical pitch, which translates to the resonant wavelength of the lasing cavity that can be tuned throughout the emission band of the fluorescent dye. The latter follows from measuring temperature transients while inducing local heating via modulating changes in excitation repetition rate at low excitation powers, analogous to methods employed in electronic systems as described in that for the bioresorbable flow sensors.[9]

Micro- and nanoimprinting of bioresorbable polymers using techniques of soft lithography can emboss these soft materials with well-defined periodic patterns of relief, with a range of examples of silk fibroin-based diffraction gratings and holograms.[205−208] These photonic components, when combined with microfluidics, yield optofluidic devices for diverse applications in biophotonic sensing. One example demonstrates spectroscopic sensing of blood oxygen, where a nanoimprinted silk grating (600 grooves mm^{-1}) doped with lysed red blood cells can be configured into microfluidic channels to capture selective binding of oxygen to the hemoglobin, via the time-dependent appearance of absorption peaks at 540 and 575 nm (Figure 13g). Similar spectral analysis further extends to nanoimprinted, large-area Mg plasmonic structures for monitoring of environmental humidity level and physiological detection of sweat loss on human skin.[209] The device is composed of arrays of nanoposts formed on a flexible polyurethane substrate supporting sputter deposited Mg nanodisks (~80 nm thick and ~300 nm in diameter). Morphological dissolution of Mg in moisture or water/biofluid at a controlled rate induces reduction in Mg thickness and thus gradual tuning of transmission spectra or simple color change, serving as indicators of water soaking time (Figure 13h). Fully bioresorbable prototypes of such plasmonic devices can also be realized by integrating Mg nanostructures with resorbable substrates.

4. BIORESORBABLE POWER SUPPLIES

Most conventional power supplies are not applicable to bioresorbable electronics because they typically rely on

https://doi.org/10.1021/acs.chemrev.3c00408
Chem. Rev. XXXX, XXX, XXX−XXX

Table 2. Performance Characteristics of Bioresorbable Batteries[a]

electrodes materials	electrolyte	voltage	specific/areal capacity	ref
Mg−Mo	PBS	0.45 V (0.1 mA cm^{-2})	276 mAh g^{-1} (0.1 mA cm^{-2})	224
Mg−Fe	0.9 wt % NaCl	0.7 V (230 μA cm^{-2})	1100 mAh g^{-1} (230 μA cm^{-2})	225
Mg−PPy	PBS	1.24 V (10 μA cm^{-2})	3.79 mAh cm^{-2} (10 μA cm^{-2})	57
Mg alloy-Au	SF-[Ch][NO_3]	1.21 V (OCV)	0.06 mAh cm^{-2} (10 μA cm^{-2})	234
Mg-MoO_3	alginate hydrogel	1.6 V (25 μA cm^{-2})	6.5 mAh cm^{-2} (25 μA cm^{-2})	227
$Mg_{100-x}Zn_x$-Fe	PBS	1.6−0.9 (OCV)	N/A	226
Mg-FeMn	body fluids	0.984 V (OCV)	N/A	28
Zn-MnO_2/CNT	gelatin−silk protein	1.55 V (61.6 mA g^{-1})	311.7 mAh g^{-1} (61.6 mA g^{-1})	218
PDA/PPy-MnO_2	body fluids	1.2 V (1000 mA g^{-1})	25.6 mAh g^{-1} (1000 mA g^{-1})	231
Zn@CS@Al_2O_3−Au	0.9 wt % NaCl	0.55 V (3.57 mA cm^{-2})	240 mAh g^{-1} (3.57 mA cm^{-2})	230
Mg−I_2	IL/aqueous	1.8 V (0.4 mA cm^{-2})	9.8 mAh cm^{-2} (0.4 mA cm^{-2})	228
Mg-MoO_3	calcium alginate gel	1.5 V (OCV)	∼1.6 mAh cm^{-2} (45 μA cm^{-2})[a]	229
Zn-(PEDOT-COOH)	gelatin−$ZnSO_4$ gel	1.2 V (0.25 A g^{-1})	31.8 mAh g^{-1} (0.25 A g^{-1})	232

[a]Note: All cutoff voltages are 0 V. N/A: not available.

nonbioresorbable materials that are also toxic. The materials outlined in section 2 and others can be used to fabricate power supplies that are fully bioresorbable, with operating parameters that are useful for practical applications in temporary biomedical implants.[82,210−215] This section reviews recent advances in bioresorbable power supplies including batteries, supercapacitors, and mechanical, radio frequency, and photovoltaic energy harvesters. They all have their own advantages and disadvantages. Batteries can provide high energy density, however, with limited power density. Supercapacitors offer high power density but suffer from fast self-discharge. Both batteries and supercapacitors can be implanted to targeted locations, to bypass the need of external power. Mechanical, radio frequency, and photovoltaic energy harvesters require external delivery of power through mechanical waves, inductive coupling, and light illumination, respectively. The advantages are in long, sometimes unlimited, operational lifetime and lightweight construction. Use in deep tissue locations is, however, limited, and they require attention to issues such as alignment, scattering, attenuation, absorption, and coupling of signals at the tissue interface. Mechanical energy harvesters can generate high output voltages, but large sizes are necessary for practical levels of power output and their operation can be intermittent and unpredictable. Radio frequency and photovoltaic energy harvesters allow high output power, but with limitations that can follow from thermal loading effects on adjacent tissues. Selection and design of power supplies must satisfy specific application requirements.

4.1. Batteries

Batteries based on lithium-ion,[216,217] zinc-ion,[218−220] and alkaline[221] chemistries are widely used energy storage systems for electronic devices of nearly all types. A battery consists of one or more galvanic cells to convert chemical energy into electrical energy through spontaneous redox reactions. The key components are anodes, cathodes, electrolytes, separators, and packaging structures.[222,223] Table 2 provides an overview of the performance characteristics of bioresorbable batteries.

The first reported bioresorbable battery design[224] uses Mg foil as the anode, with Fe, W, or Mo foils as the cathode, and PBS as the electrolyte as the basis for a primary cell. The anode, cathode, and full cell reactions are $Mg - 2e^- + 2H_2O \rightarrow Mg(OH)_2 + 2H^+$, $2H^+ + 2e^- \rightarrow H_2$, and $Mg + 2H_2O \rightarrow Mg(OH)_2 + H_2$, respectively. Reported Mg−Mo cell configurations can achieve an operating voltage of 0.45 V at a discharge current density of 0.1 mA cm^{-2} and a stable power supply for at least 24 h.[224] The associated battery delivers a specific capacity of 276 mAh g^{-1} at a current density of 0.1 mA cm^{-2}. Further, a battery that combines four such cells in series offers a stable discharge at 1.5−1.6 V for over 6 h (Figure 14a).[224] Packaging structures formed with PCL increase the specific capacity of the Mg anodes by 70% by reducing the rate of corrosion of this metal.[225] An Mg−Fe cell with a 0.9 wt % NaCl electrolyte provides an average voltage of 0.4 V and a specific capacity of 1100 mAh g^{-1} at a current density of 230 μA cm^{-2}.[225] The low voltage outputs and energy densities in these cases follow from the use of cathodes with low electrochemical potential. Mg alloys can serve as alternatives to Mg for bioresorbable anodes. Alloying Mg with Zn ($Mg_{100-x}Zn_x$ alloy) helps to mitigate the natural corrosion of Mg anodes.[226] Adding 20% to 41% Zn reduces the cell open circuit voltage from 1.6 to 1.3 V. Cells with a 34% Zn-doped alloy anode exhibit the largest areal capacity of 4.8 mAh cm^{-2} at a discharge current density of 10 μA cm^{-2} and a cutoff voltage of 0.5 V.[226]

Cathode materials such as MoO_3, offer increased electrochemical potential to mitigate the limitations of Fe, W, and Mo cathodes on voltage outputs and energy densities.[227] The cathode reaction in this case is $MoO_3 + \alpha M^{n+} + n\alpha e^- \rightarrow M_\alpha MoO_3$. A representative bioresorbable Mg-MoO_3 cell (Figure 14b, left) consists of Mg foil as the anode, MoO_3 paste as the cathode, Mo foil as the cathode current collector, and alginate hydrogel as the electrolyte, to realize an output voltage of up to 1.6 V.[227] Even a single cell of this type can power a red LED (threshold voltage ≈1.5 V) for 16 h (Figure 14b, middle). The discharge plateau (Figure 14b, right) at voltages above 1 V and below 1 V can be mainly attributed to the pseudocapacitance of the MoO_3 and hydrogen evolution reactions on the cathode, respectively. At an operating voltage of 1.6 V, the areal capacity is 6.5 mAh cm^{-2} under a discharge current density of 25 μA cm^{-2}.[227]

Bioresorbable cathode materials such as MoO_3[227] and I_2[228] ($I_2 + 2e^- \rightarrow 2I^-$) undergo dissolution in aqueous electrolytes. Replacing aqueous PBS electrolytes with alginate hydrogels improves battery performance by slowing the rate of the dissolution in the case of MoO_3 (Figure 14b, right).[227] A bioresorbable ionic liquid electrolyte can similarly address the challenge of dissolution of I_2.[228] Here, a dual electrolyte system with biofluid/PBS as the anolyte and a choline chloride/urea-based ionic liquid as the catholyte provides a balanced choice.[228] In this example, Mg and I_2 serve as anodes and cathodes,

https://doi.org/10.1021/acs.chemrev.3c00408
Chem. Rev. XXXX, XXX, XXX−XXX

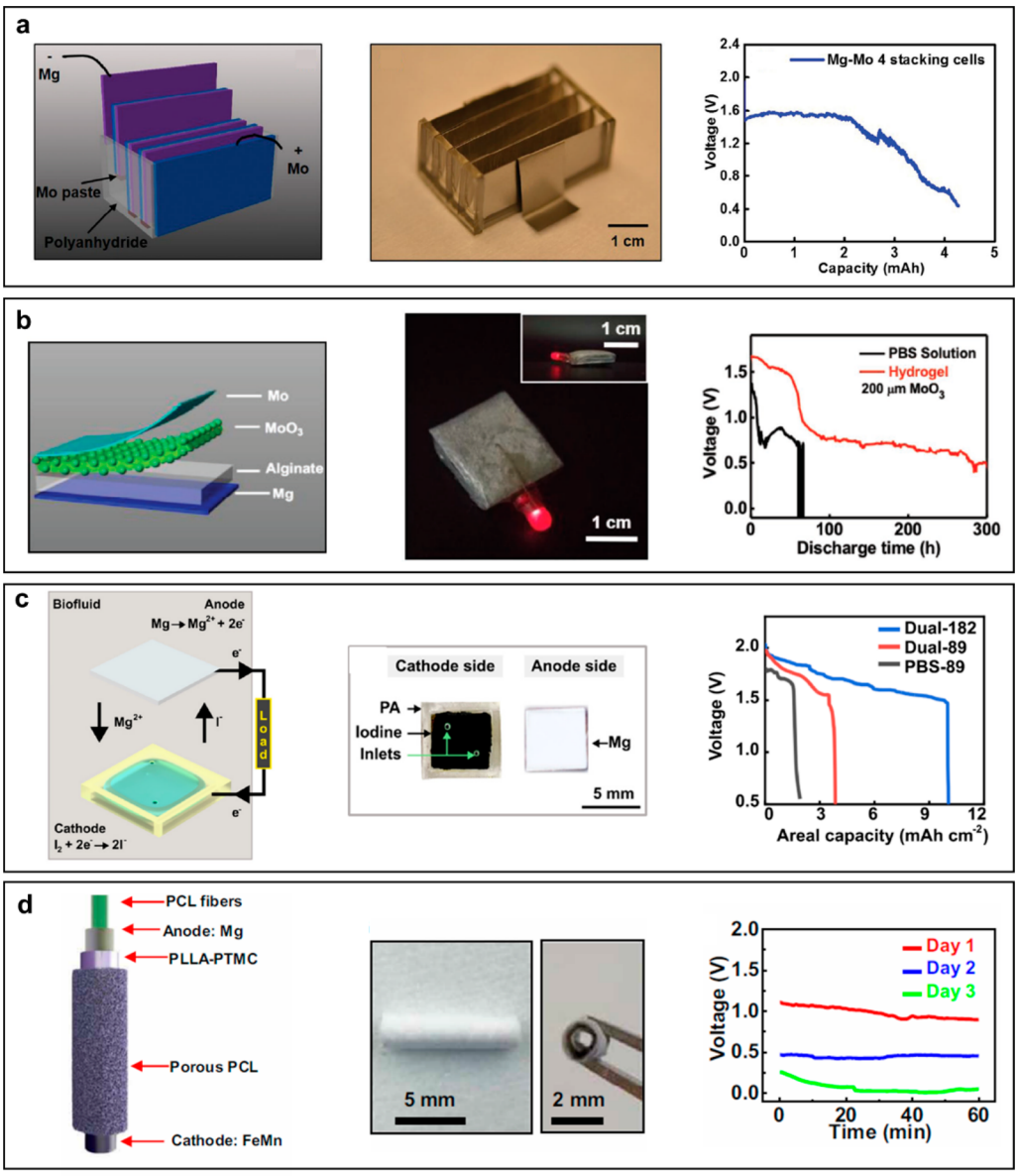

Figure 14. Examples of bioresorbable batteries. (a) Schematic illustration (left), optical image (middle), and discharging behavior (right, 0.1 mA cm^{-2}) of a battery pack that consists of four Mg–Mo cells in series.[224] Reproduced with permission from ref 224. Copyright 2014 Wiley-VCH. (b) Schematic illustration (left), optical image (middle), and discharging behavior (right, 25 μA cm^{-2}) of an Mg-MoO_3 battery with hydrogel and phosphate-buffered saline electrolytes.[227] Reproduced with permission from ref 227. Copyright 2018 Wiley-VCH. (c) Schematic illustration (left), optical image (middle), and discharging behavior (right, 0.4 mA cm^{-2}) of dual-electrolyte Mg–I_2 batteries.[228] Reproduced with permission from ref 228. Copyright 2022 Royal Society of Chemistry. (d) Schematic illustration (left), optical image (middle), and *in vivo* measured OCV (right) of an Mg-FeMn self-electrified conduit device.[28] Reproduced with permission from ref 28. Copyright 2020 American Association for the Advancement of Science.

respectively. A polyanhydride structure encapsulates the cathode and catholyte with two holes to enable ionic conduction between anolyte and catholyte (Figure 14c, left).[228] The open environment of the anolyte (biofluid) allows the release of hydrogen generated from Mg corrosion (Figure 14c, middle).[228] Batteries with these design features offer superior performance compared to that with a single PBS electrolyte (Figure 14c, right). A cell with 182 mg cm^{-2} I_2 loading delivers an areal capacity of 9.8 mAh cm^{-2} and an operating voltage of 1.8 V when discharged at 0.4 mA cm^{-2}.[228]

Strategies to achieve flexible properties involve stretchable cells[229] and filament/fibrous cells.[28,218,230,231] One approach uses kirigami patterns in Mg anodes structured by laser cutting.[229] In one such case, MoO_3 paste on Mo foil serves as the cathode, and alginate serves as the electrolyte. At a discharge current density of 45 μA cm^{-2}, this type of battery delivers a capacity of 4.7 mAh and an energy density of 1.72 mWh cm^{-2}. The cell provides a discharge voltage of 1.5 V after 900 deformation cycles to a linear strain of 20%.[229] In another example, a coaxial structure in a Mg-FeMn battery supports an electrical interface to accelerate healing of nerves (Figure 14d, left and middle).[28] The bioresorbable battery itself wraps the nerve and produces an electric field along the direction of the nerve for purposes in stimulation. The open circuit voltage decreases from ~0.98 V to ~0.07 V from 1 to 3 days, as shown in

https://doi.org/10.1021/acs.chemrev.3c00408
Chem. Rev. XXXX, XXX, XXX−XXX

Table 3. Performance Characteristics of Bioresorbable Supercapacitors[a]

electrodes materials	electrolyte	specific/areal capacitance	energy density	ref
activated charcoal	gatorade	78.8 F g^{-1} (1 A g^{-1})	N/A	245
Mo	NaCl/agarose gel	1.6 mF cm^{-2} (0.15 mA cm^{-2})	0.14 μWh cm^{-2} (61 μW cm^{-2})	16
anodized Mo oxide	NaCl/PVA gel	4.2 mF cm^{-2} (0.05 mA cm^{-2})	0.37 μWh cm^{-2} (0.8 mW cm^{-2})	242
MoO_x	sodium alginate gel	112.5 mF cm^{-2} (1 mA cm^{-2})	15.64 μWh cm^{-2} (27 μW cm^{-2})	244
ZnO	PVA/PBS gel	0.9 mF cm^{-2} (0.1 mA cm^{-2})[a]	0.15 μWh cm^{-2} (27 μW cm^{-2})	238
Zn@PPy	NaCl/agarose	2.84 mF cm^{-2} (current density not available)	0.39 μWh cm^{-2} (3.4 μW cm^{-2})	243
Zn-activated carbon	gelatin/$ZnSO_4$ gel	605 mF cm^{-2} (0.2 mA cm^{-2})	215 μWh cm^{-2} (132 μW cm^{-2})	246
Zn-MoO_3−MoS_2	gelatin/$ZnSO_4$ gel	182 mF cm^{-2} (0.5 mA cm^{-2})	30.6 μWh cm^{-2} (2.2 μW cm^{-2})	237

[a]*Specific capacitance obtained after 20 days incubation test in 37 °C PBS solution. N/A: not available.

Figure 14d (right).[28] The electrochemical reactions for these two types of batteries are the same as those described earlier.

These bioresorbable batteries operate as primary (i.e., nonrechargeable) cells. Rechargeable batteries are also of interest. One example is a Zn-(PEDOT-COOH) battery with an edible gelatin-$ZnSO_4$ gel electrolyte.[232] The anode, cathode, and full cell reactions are $Zn + SO_4^{2-} \leftrightarrow ZnSO_4 + 2e^-$, $2(PEDOT{-}COOH)^+/SO_4^{2-} + 2e^- \leftrightarrow 2(PEDOT{-}COOH)^0 + SO_4^{2-}$, and $Zn + 2(PEDOT{-}COOH)^+/SO_4^{2-} \leftrightarrow 2(PEDOT{-}COOH)^0 + ZnSO_4$, respectively. Such cells achieve energy densities of 39 mWh g^{-1} at power densities of 307 mW g^{-1} and operating voltages of 1.2 V and specific capacities of 31.8 mAh g^{-1} at current densities of 0.25 A g^{-1}. Another report describes a bioresorbable Zn-MnO_2/CNT battery with a humidity-sensitive plasticized gelatin-silk fibroin as the electrolyte.[218] The anode, cathode, and full cell reactions are $Zn \leftrightarrow Zn^{2+} + 2e^-$, $Zn^{2+} + 2e^- + 2\alpha\text{-}MnO_2 \leftrightarrow ZnMn_2O_4$, and $Zn + 2\alpha\text{-}MnO_2 \leftrightarrow ZnMn_2O_4$, respectively. At a current density of 61.6 mA g^{-1}, cells of this type exhibit an output voltage of up to 1.55 V and a specific capacity of 310 mAh g^{-1}. The capacity retention is above 90% under various deformations such as bending, knotting, and twisting, indicating the potential for use in flexible electronic systems.[218] Environmentally degradable rechargeable batteries[233] such as these may serve as useful starting points in the development of similar devices that are resorbable in the body.

4.2. Supercapacitors

Supercapacitors are electrochemical capacitors that can offer exceptionally high energy densities and long cycle lifetimes, as attractive alternatives to batteries for certain applications.[16,235,236] Bioresorbable supercapacitors that consist of optimized electrodes, electrolytes, separators, and packaging structures can power realistic devices of various types.[237,238] Electric double-layer capacitors, pseudocapacitors, and hybrid supercapacitors are three types of devices. Table 3 provides an overview of the performance characteristics of bioresorbable supercapacitors.

Electric double-layer capacitors store the charge electrostatically. The first reported bioresorbable supercapacitor is an electric double-layer capacitor involving planar electrodes of W, Fe, or Mo on PLGA substrates with agarose gel electrolytes (Figure 15a, left).[16] Cyclic voltammetry (CV) measurements indicate unchanged performance under different deformations (Figure 15a, middle), even with better reversible capacitive behaviors than those of similar devices constructed with Au (Figure 15a, right). Mo-based supercapacitors exhibit energy densities of 0.14 μWh cm^{-2} at power densities of 61 μW cm^{-2} and 0.0083 μWh cm^{-2} at 1.0 mW cm^{-2}.[16] Charging two Mo-based capacitors connected in series to 2.2 V provides power needed to operate an LED (turn-on voltage of 2.1 V) for ≈18 s.[16] In addition to planar supercapacitors, wire-shaped devices allow a range of interesting structural options, including devices that adopt fiber-shaped[239−241] and serpentine-shaped[242] layouts. Wrapping two Mo wires with oxide layers with a PVA gel electrolyte yields a serpentine-shaped stretchable bioresorbable supercapacitor[242] with an areal capacitance of 4.15 mF cm^{-2} at a current density of 0.05 mA cm^{-2} and an energy density of 0.37 μWh cm^{-2} at a power density of 0.8 mW cm^{-2}. Capacitance retention of 91% under a 30% strain after 1000 cycles of stretch/release is an example of the impressive mechanical properties of this design.[242]

Pseudocapacitors store the charge electrochemically. One bioresorbable example uses a symmetrical layer-by-layer structured design as an energy storage unit, with Fe films as the current collectors, ZnO nanoporous layers self-assembled on the Fe films as the active materials, PLA as the supporting substrates, PLA nanopillar arrays as the adhesion promotor for the Fe films, and PVA/PBS solution as the electrolyte.[238] The resulting devices exhibit areal capacitances of 0.9 mF cm^{-2} and energy densities of 0.153 μWh cm^{-2} at power densities of 27 μW cm^{-2}, with capacitance retention of 70% after 3000 charge/discharge cycles.[238] Another bioresorbable design uses a Zn@PPy structure formed by electrochemical deposition of PPy onto a screen-printed Zn film, with a NaCl/agarose electrolyte.[243] The resulting supercapacitor delivers an areal capacitance of 2.84 mF cm^{-2} and an energy density of 0.39 μW h cm^{-2} at a power density of 3.4 μW cm^{-2}.[243] These two examples have, however, the disadvantage of relatively low energy and/or power densities. Bioresorbable MoO_x supercapacitors (Figure 15b, left) with sodium alginate gel electrolytes offer improved performance.[244] Here, electrochemical oxidization of the surfaces of Mo foils forms amorphous coatings of MoO_x (Figure 15b, middle). These MoO_x supercapacitors achieve areal capacitances of 112.5 mF cm^{-2} at current densities of 1 mA cm^{-2} and capacitance retention of 86.7% after 2000 charge−discharge cycles. The quasi-rectangular-shaped CV curves (Figure 15b, right) indicate good capacitive behavior due to the large surface areas of derived dendrite flakes and oxygen vacancy defects as storage/absorption sites.[244]

Hybrid supercapacitors combine attractive features of electric double-layer capacitors and pseudocapacitors, with higher energy density than electric double-layer capacitors and higher power than batteries. A bioresorbable Zn-ion hybrid supercapacitor (Figure 15c, left) uses Zn as an anode, heterostructured MoO_3−MoS_2 as a capacitive-type cathode, and gelatin/$ZnSO_4$ gel as an electrolyte.[237] Electrochemically oxidizing the surface of a Mo foil to MoO_3 followed by a hydrothermal sulfurization (anion exchange between O^{2-} and S^{2-}) forms a MoO_3−MoS_2 composite.[237] A cell of this type can provide an areal capacitance of 181.86 mF cm^{-2} at a current density of 0.5

https://doi.org/10.1021/acs.chemrev.3c00408
Chem. Rev. XXXX, XXX, XXX−XXX

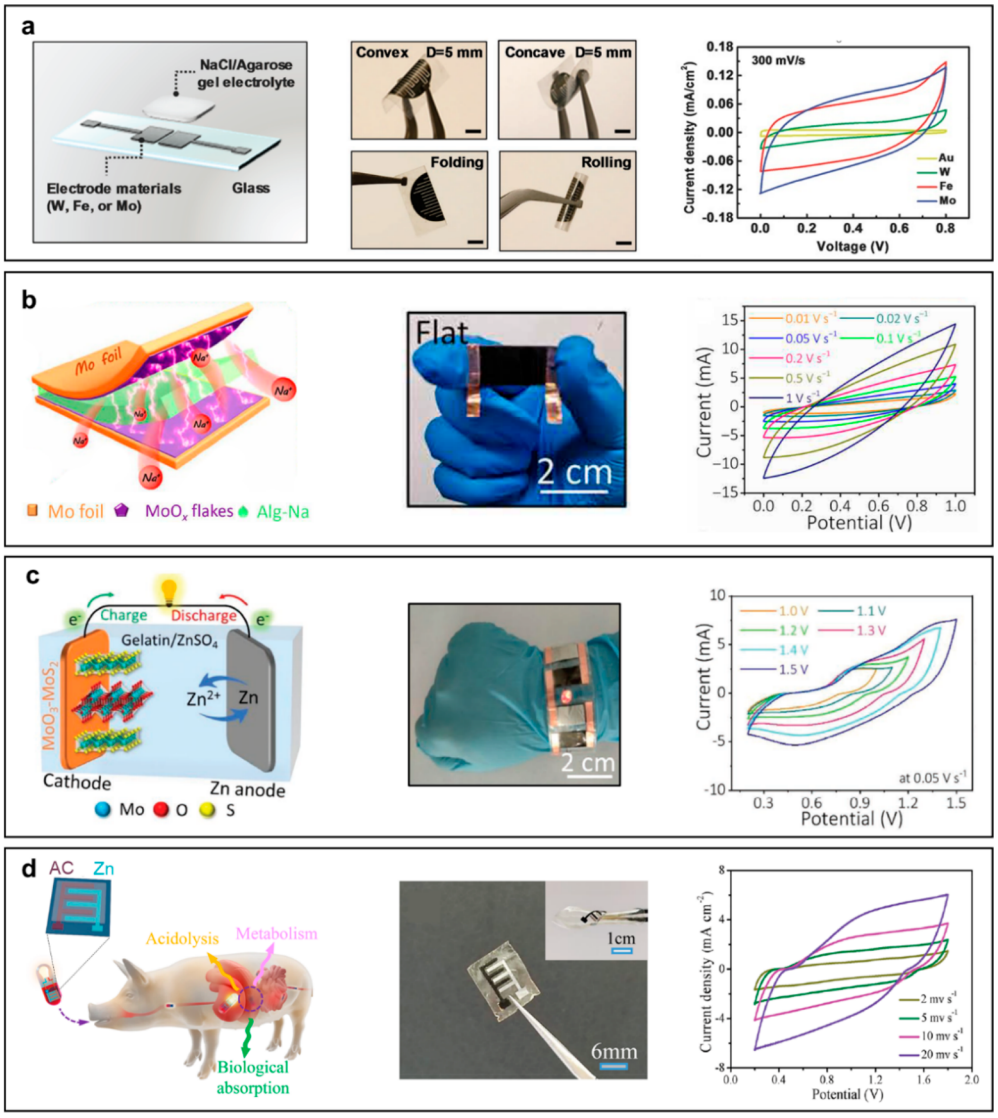

Figure 15. Examples of bioresorbable and edible supercapacitors. (a) Schematic illustration (left), optical images (middle, Mo), and CV curves (right) of bioresorbable W/Fe/Mo microsupercapacitors.[16] Scale bar: 3 mm. Reproduced with permission from ref 16. Copyright 2017 Wiley-VCH. (b) Schematic illustration (left), optical image (middle), and CV curves (right) of bioresorbable MoO_3 supercapacitor implants.[244] Reproduced with permission from ref 244. Copyright 2021 American Association for the Advancement of Science. (c) Schematic illustration (left), optical image (middle), and CV curves (right) of edible Zn//MoO_3–MoS_2 hybrid supercapacitors.[237] Reproduced with permission from ref 237. Copyright 2022 Wiley-VCH. (d) Schematic illustration (left), optical image (middle), and CV curves (right) of edible zinc-ion-based AC hybrid microsupercapacitors.[246] Reproduced with permission from ref 246. Copyright 2022 American Chemical Society.

mA cm^{-2} and an energy density of 30.56 μWh cm^{-2} at a power density of 2.2 μWh cm^{-2} (Figure 15c, right). After charged, four cells connected in series can operate a red LED (Figure 15c, middle).[237]

For completeness, this subsection concludes with a discussion of edible supercapacitors.[245,246] Even though these devices often include nonbioresorbable components, such as activated carbon, they are of interest in bioresorbable electronics for monitoring or treatment of the digestive system, such as the gastrointestinal tract.[247] One such edible example uses activated charcoal as the electrode, egg white as the binder, seaweed as the separator, polyelectrolyte beverage as the electrolyte, and cheese as the segregation layer.[245] The specific capacitance remains almost constant, from 78.8 to 72.7 F g^{-1}, after 1000 cycles of charging/discharging at a constant current density of 1 A g^{-1}, with a retention rate of 92.3%. Connecting five charged supercapacitors in series generates a voltage output of 5 V, sufficient to operate a USB camera (operating voltage of 3.3 V).[245] In addition to this type of symmetric supercapacitor,[245] another hybrid edible device[246] (Figure 15d, left) uses Zn as the anode, activated carbon as the cathode, and gelatin/$ZnSO_4$ gel as the electrolyte (Figure 15d, middle). At current densities of 0.2 mA cm^{-2}, such cells deliver areal capacitances of 605 mF cm^{-2}, energy densities of 215.1 μWh cm^{-2} at power densities of 132 μW cm^{-2} (Figure 15d, right). When fully charged, voltages can reach 1.8 V, sufficient to power a red LED.[246]

4.3. Mechanical Energy Harvesting

Mechanical energy harvesters based on piezoelectric or triboelectric effects can convert mechanical energy into electrical energy.[248] Such devices in bioresorbable forms can be paired with batteries and supercapacitors for storage, or they can be used directly to power various types of bioresorbable electronic

https://doi.org/10.1021/acs.chemrev.3c00408
Chem. Rev. XXXX, XXX, XXX−XXX

Table 4. Performance Characteristics of Bioresorbable Mechanical Harvesters[a]

materials	dimensions	energy sources	implantation depths	voltage and current outputs	generated power	energy-conversion efficiency	ref
Piezoelectric							
ZnO	~1.5 cm × 1.5 cm	cyclic bending	N/A	~1.14 V and ~0.55 nA	~10 nW/cm^2	0.28%	98
KNN/PLLA/PHBV	~2 cm × 2 cm	ultrasound (0.7 W cm^{-2})	N/A, sciatic nerve	12 V and 36 μA	0.3 mW/cm^2	N/A	254
KNN/PLA	~4.5 cm × 4.5 cm	acoustic pressure (150 kPa)	N/A, spinal cord	12.09 V and 20.8 μA	N/A	N/A	77
Triboelectric							
PLA/gelatin	4 cm × 4 cm	contact force (50 N)	N/A	500 V and 10.6 mA m^{-2}	5 W/m^2	N/A	272
PLGA/PCL	2 cm × 3 cm	compression/release (1 Hz)	N/A	~40 V and ~1 μA	32.6 mW/m^2	N/A	83
PLGA/Mg	~1.5 cm × 1.5 cm	rat's normal movements	N/A, under skin	~2 V	N/A	N/A	275
Mg/PHBV/PEG	2 cm × 2 cm	ultrasound (0.5 W cm^{-2})	0.5–1 cm	4.51 V and 27.86 μA (20 kHz)	17.24 μW cm^{-2}	N/A	276

[a]N/A: not available.

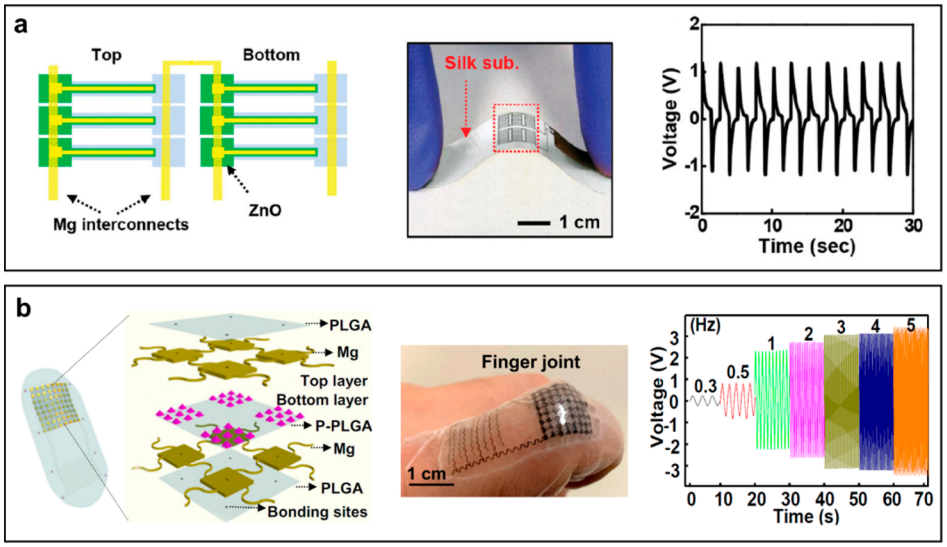

Figure 16. Examples of mechanical energy harvesters. (a) Schematic illustration (left), optical image (middle), and voltage output (right) of piezoelectric energy harvesters during cycles of bending.[98] Reproduced with permission from ref 98. Copyright 2013 Wiley-VCH. (b) Schematic illustration (left), optical image (middle), and voltage output (right) of triboelectric energy harvesters.[275] Reproduced with permission from ref 275. Copyright 2021 United States National Academy of Sciences.

systems. Table 4 provides an overview of the performance characteristics of bioresorbable mechanical energy harvesters.

4.3.1. Piezoelectric Energy Harvesters. Piezoelectric energy harvesters convert kinetic energy in the form of vibrations, shock waves, or mechanical movements into electrical energy through the piezoelectric effect, which relies on the intrinsic polarization of the active material.[249−253] Mechanical stresses induced in the piezoelectric component of an energy harvester generate charges on the surfaces of this component, which can induce the flow of electrical current when connected to the external load.

An early example of a bioresorbable device of this type (Figure 16a, left) incorporates a piezoelectric thin film of ZnO (500 nm thick) as the piezoelectric component, Mg (300 nm/500 nm thick) for the bottom and top electrodes, MgO as a dielectric, and silk fibroin as a flexible substrate (Figure 16a, middle).[98] The ZnO layer lies between the top and bottom Mg electrodes. In one embodiment, the voltage and current outputs are ~1.14 V and ~0.55 nA (Figure 16a, right), respectively, for cyclic bending. The power density is ~10 nW/cm^2 with 0.28% energy-conversion efficiency for this mode of deformation.[98]

As an alternative to mechanical deformations such as those associated with bending, ultrasound represents a form of mechanical energy that is of particular interest for applications deep within tissues. Here, power from ultrasound activates mechanical vibrations that can be converted into electrical power via piezoelectric effects. Ultrasound-driven electrical stimulation techniques based on devices designed for these purposes can accelerate repair of injuries to the peripheral nerves[254] and spinal cords.[77] A bioresorbable example for peripheral nerve injury repair[254] consists of piezoelectric materials formed by a combination of potassium sodium niobate ($K_{0.5}Na_{0.5}NbO_3$, KNN) nanowires, PLLA, and PHBV, with films of PLA or PCL as encapsulants, Mg as electrodes, and Mo wires as the wiring of nanogenerators. KNN nanowires serve as high-performance piezoelectric dopants in piezoelectric PHBV and PLLA polymer matrices, to achieve a composite with good mechanical properties and rates of bioresorption that can be selected over a wide range.[254] Such devices exhibit output voltages and currents of 12 V and 36 μA, respectively, for exposure to ultrasound at a frequency of 100 kHz, a pulse width of 50 μs, a pulse interval of 10 ms, and intensity of 0.7 W cm^{-2}.[254]

https://doi.org/10.1021/acs.chemrev.3c00408
Chem. Rev. XXXX, XXX, XXX−XXX

Table 5. Performance Characteristics of Radio Frequency Energy Harvesters[a]

antenna materials	shape	dimensions	resonance frequency	transmitted distance	source power	generated power	power conversion efficiency	ref
Mg/SF	linear dipole, two quarter wavelength arms and wideband quasi log-periodic dipoles	~4 cm × 12 cm	≈950 MHz	~2 m (air)	~20 W	54 mW	15.7%	126
Mg/PLGA	disk, 34 turns	10 mm in radius	~5 MHz	8 cm (chicken meat)	~11 V_{pp}	1 V	20% (5 cm distance)	24
Mg/PLGA	disk, 17 turns	25 mm in diameter	~13.56 MHz	10 cm (air) + skin thickness	~12 W	100 mW	5% (15 mm distance)	22
Mg/PLGA	disk, 17 turns	20 mm in diameter	83 Hz	4 mm (chicken meat)	N/A	3.26 V_{pp}	N/A	280

[a]N/A: not available.

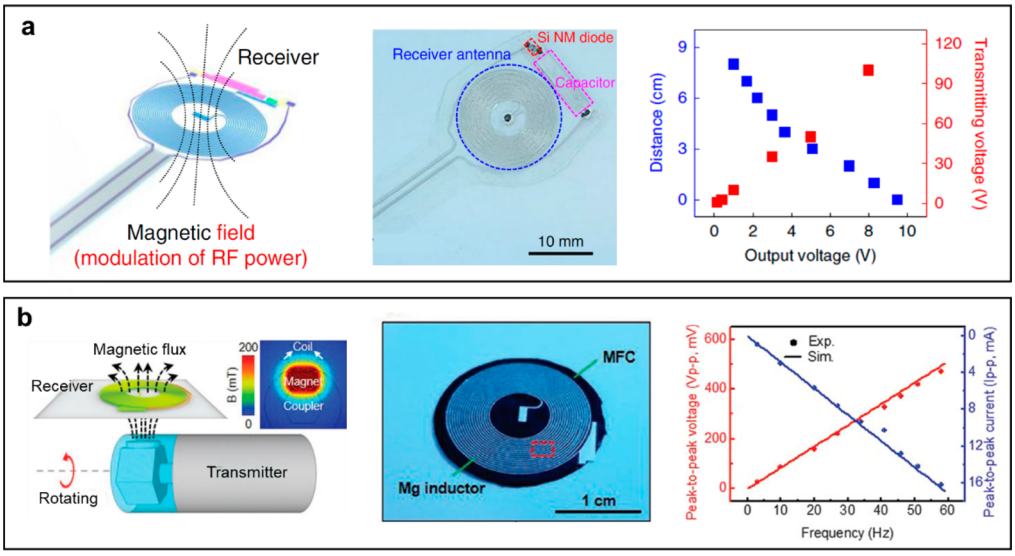

Figure 17. Examples of bioresorbable radio frequency (a) and low frequency (<200 Hz, b) inductive energy harvesters. (a) Schematic illustration (left), optical image (middle), and voltage output (right) of a radio frequency power harvester.[24] Reproduced with permission from ref 24. Copyright 2018 Springer Nature. (b) Schematic illustration (left), optical image (middle), and power output (right) of a low-frequency inductive harvesting system.[280] Reproduced with permission from ref 280. Copyright 2019 Wiley-VCH.

Alternative bioresorbable devices for application to the spinal cord consist of PLA nanofibers with KNN nanowires.[77] The output voltages and currents in this case are 12.09 V and 20.8 μA, respectively, at a frequency of 1 MHz, a pulse width of 5 μs, a pulse interval of 10 ms, and an acoustic pressure of 150 kPa.[77] Similar mechanisms appear in other bioresorbable piezoelectric energy harvesters based on PLLA[255−257] and PHB[258] for electrical stimulation of tissue,[258] cartilage,[256] and bone[255,257] for accelerated regeneration.

4.3.2. Triboelectric Energy Harvesters. Triboelectric energy harvesters also convert mechanical to electrical energy, but they avoid the need of piezoelectric materials by generating static polarized charges that result from contact between two different materials due to contact electrification, as described in section 3.4.1, the context of pressure sensing.[259−264] Separating these two materials by a mechanical force generates a potential drop that drives electrons to flow between the two electrodes built on the top and bottom surfaces of these two materials.[265−269] Two most popular examples of traditional triboelectric generators are the Wimshurst machine (invented in ~1880) and Van de Graaff generator (invented in ~1929).[270] Triboelectric generators (sometimes referred to as triboelectric nanogenerators, TENGs), can generate alternating-current electrical outputs under repeated contact-separation cycles. The basic structure of a TENG involves simply a pair of electrodes, a pair of dielectric materials typically with an air gap between them.[271]

A bioresorbable example of this type of device uses electrospun PLA and nanostructured gelatin as triboelectric materials with Mg plates as electrodes.[272] A 4 × 4 cm^2 device delivers an open-circuit voltage of up to 500 V, a short-circuit current density of 10.6 mA m^{-2}, and a maximum power density of over 5 W/m^2. Other bioresorbable TENGs include carrageenan−agar composite/PCL[273] and chitosan/HA hydrogel films[274] as triboelectric materials with Mg electrodes.

As an application, such generators can power pairs of nerve-interfaced electrodes to generate pulsed electrical fields for nerve repair. An example for this purpose consists of PLGA and PCL as triboelectric materials with thin Mg electrode layers, capable of delivering an open-circuit voltage of up to ~40 V and short-circuit current of ~1 μA, during cycles of compression/release at a frequency of 1 Hz.[83] Here, the induced field strength of 10 V mm^{-1} can lead to oriented growth of nerve cells. Pairing similar devices with two dressing electrodes yields a self-powered device for electrostimulation at the site of a bone fracture (Figure 16b, left).[275] These generators use an island-bridge Mg electrode affixed with a layer of PLGA and a micropyramid structure embossed onto its surface as the bottom triboelectric layer and another island-bridge Mg electrode as the top triboelectric layer (Figure 16b, middle). The micropyramid structure of the PLGA

https://doi.org/10.1021/acs.chemrev.3c00408
Chem. Rev. XXXX, XXX, XXX−XXX

Table 6. Performance Characteristics of Photovoltaic Energy Harvesters[a]

materials	dimensions	source power	distance	short-circuit currents, open-circuit voltages, output power	fill factor	power conversion efficiency	ref
monocrystalline Si doped B and P	~2 mm × 2 mm	N/A	N/A	~10 mA cm^{-2}, ~0.42 V, 2 mW	0.66	3%	86
array of monocrystalline Si doped B and P	~13.5 mm × 7.5 mm	NIR LED (200 mW cm^{-2})	4 mm thick porcine skin and fat	~20 μA, 4.25 V, 64.4 μW	0.733	1.29%	281
monocrystalline Si doped B and P	diameter ~5 mm (disk)	635 nm laser (0.1−1.8 W cm^{-2})	<2 mm PBS	30−60 mV	N/A	N/A	159
amorphous Si doped B and P	~15 mm × 15 mm	N/A	N/A	6.4 mA cm^{-2}, 0.81 V	N/A	2.6%	18

[a]N/A: not available.

improves the roughness of the triboelectric layer and thus the contact surface, which thus enhances the power density of such TENG.[275] The open-circuit peak-to-peak voltages increase monotonically from 0.5 to 6.8 V when characterized at frequencies of 0.3, 0.5, 1.0, 2.0, 3.0, 4.0, and 5.0 Hz (Figure 16b, right), which could be attributed to the higher displacement rate and thus more rapid charge transfer.[275]

As with piezoelectric harvesters, the triboelectric effect can be activated by ultrasound. One such device consists of an Mg electrode as the bottom triboelectric layer, a PHBV/PEG composite membrane as the top triboelectric layer, and a PHBV encapsulation.[276] Stable electrical outputs follow from exposure at low ultrasound intensities (0.5 W cm^{-2}), corresponding to voltage and current outputs of 4.51 V and 27.86 μA, respectively, at a frequency of 20 kHz. High intensities (3.0 W cm^{-2}) can be applied to trigger the mechanical disintegration of the PHBV encapsulation layer and, therefore, to accelerate the rates of bioresorption.[276] Another mechanism for triggering dissolution employs Au nanorods as optical absorbers for photothermally induced bioresorption.[277] Exposure to near-infrared light reduces the output of the device to 0 within 24 h, and complete bioresorption in 14 days.

4.4. Radio Frequency Energy Harvesting

Radio frequency electromagnetic transfer between transmission and receiver antennas provides an alternative to ultrasound for wireless power that can be directed to locations in deep tissue.[22] This transfer can occur either through near[22,24,126,278] or far[126] field mechanisms. The former involves magnetic inductive coupling for efficient transfer over relatively short distances, at RF frequencies that have minimal absorption by biological tissues. The latter relies on electromagnetic coupling, capable of operating over large distances but with high levels of sensitivity to antenna orientation and at frequencies that can be strongly absorbed in biological tissues. In both cases, key elements in this type of transfer are the antennas and, in many applications, the rectifying electronics needed to convert alternating to direct current outputs. Table 5 provides an overview of the performance characteristics of bioresorbable RF energy harvesters.

An example of a simple bioresorbable antenna involves linear-dipole shaped features of Mg (500 nm thick, two quarter wavelength arms, and wideband quasi log-periodic dipoles) on films of silk fibroin, formed by physical vapor deposition through shadow masks, as described in section 3.3.1.[126] Operating this antenna (≈ 950 MHz) in a far field mode at a distance of ~2 m allows power transfer of 54 mW, with a transmitted RF power of ~20 W.[126] An example of a near-field bioresorbable RF harvester (Figure 17a, left, a disk-shaped coil, 34 turns, 10 mm in radius) consists of a bilayer of disk-shaped Mg coils, a poly (lactic-*co*-glycolic acid) dielectric interlayer, a Si NM RF diode for rectification, and a plate Mg/SiO_2/Mg smoothing capacitor (Figure 17a, middle).[24] This harvester, with a resonance frequency of ~5 MHz, delivers power to tissue-interfaced electrodes for nerve regeneration. Transfer of power (~11 V_{pp}) over distances of up to 8 cm yields output voltages of 1 V (Figure 17a, right), sufficient for this application.[24] A low-frequency PIN diode with high parasitic capacitance provides an alternative, capacitor-free harvester design (a disk-shaped coil, 17 turns, 25 mm in diameter) with a resonance frequency of ~13.56 MHz, a standard in commercial electronics, as a power supply for cardiac pacing.[22] At a distance of 10 cm between the transmission and receiver coils yields an output power of 100 mW, with a transmitted RF power of ~12 W. In advanced embodiments, multiple receiver coils with different resonance frequencies serve the basis for frequency-selective power harvesting to different components of a single device or selective harvesting to a collection of devices in a similar space.[279] An example of this mechanism is in programmed drug release events from multiple, independently controlled drug reservoirs.[29]

Related inductive harvesting mechanisms can be realized at low frequencies (Figure 17b, left) by use of rotating magnets (<200 Hz) instead of RF powered transmitter antennas.[280] One report uses neodymium disc magnets (5 mm thick, 9 mm in diameter) mounted on a rotating stage.[280] Embedding bioresorbable iron oxide nanoparticles in PLGA forms a magnetic field concentrator (MFC) to enhance the efficiency of harvesting when placed atop disk-shaped receiver coils (17 turns, ~20 mm in diameter) of Mg/PLGA/Mg (Figure 17b, middle). Time varying magnetic fields induced by the rotating magnet leads to power output. Peak-to-peak voltages and currents depend linearly on the rotational frequency (Figure 17b, right). Operating at 83 Hz and a working distance of 4 mm yields peak-to-peak voltages of 3.26 V.[280]

4.5. Photovoltaic Energy Harvesting

Photovoltaic (PV) cells rely on electromagnetic radiation in the visible range, by use of photon induced charge carriers in p- and n-type semiconductors[281] via the photovoltaic effect.[282−284] Table 6 provides an overview of the performance characteristics of bioresorbable PV energy harvesters. Initial reports of Si NMs in bioresorbable electronics also include demonstrations of Si-based bioresorbable solar cells using bars of monocrystalline Si (~3 μm thick) with boron and phosphorus doping to define p- and n-type regions, and Mg interconnects.[86] These devices produce short-circuit currents of ~10 mA cm^{-2} and open-circuit voltages of ~0.42 V, with corresponding fill factors of 66% and overall power conversion efficiencies of ~3% under illumination

https://doi.org/10.1021/acs.chemrev.3c00408
Chem. Rev. XXXX, XXX, XXX−XXX

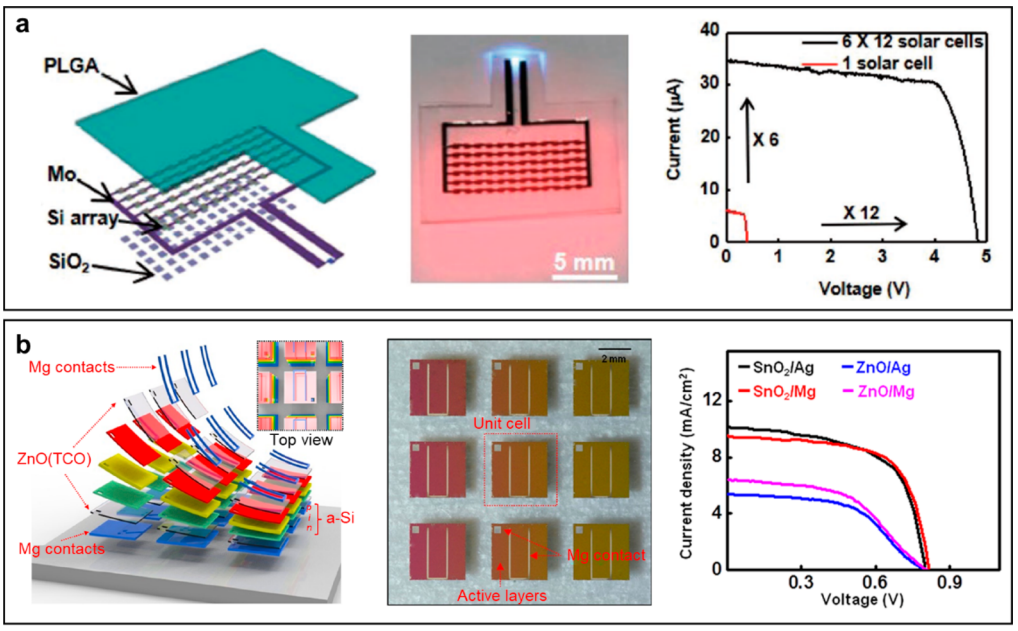

Figure 18. Examples of bioresorbable photovoltaic energy harvesters. (a) Schematic illustration (left), optical image (middle), and current/voltage characteristics (right) of monocrystalline silicon photovoltaic microcells.[281] Reproduced with permission from ref 281. Copyright 2018 Wiley-VCH. (b) Schematic illustration (left), optical image (middle), and current/voltage characteristics (right) of a-Si photovoltaic microcells.[18] Reproduced with permission from ref 18. Copyright 2018 Wiley-VCH.

using light from a solar simulator.[86] Scaled arrays of related types of solar cells (Figure 18a, left) include as many as 72 cells with 12 columns connected in series and six rows in parallel.[281] Each cell exhibits a power conversion efficiency of 1.29% with an open-circuit voltage of 0.40 V, a short circuit current density of 4.37 mA cm^{-2}, and a fill factor of 0.733 (Figure 18a, right). The array yields an open-circuit voltage of 4.84 V with a short-circuit current of 34.45 μA, and a total output power of 122 μW, sufficient to operate a blue LED immersed in PBS solution (Figure 18a, middle) under illumination from a solar simulator at a power of 100 mW cm^{-2}.[281] Illuminating an array placed under a piece of porcine skin and fat (4 mm thick) with an NIR LED (200 mW cm^{-2}) generates an output power of 64.4 μW and an open-circuit voltage of 4.25 V. Operation of a blue LED powered by the PV array implanted in the infrascapular region of a rat under NIR illumination provides a demonstration of the capabilities.[281] Mounting bioresorbable thin-film monocrystalline Si pn diodes on nerve tissue can optoelectronically modulate neural activity by delivering polarity-dependent photovoltages.[159] In this design, doping boron and phosphorus ions into n- and p-type SOI wafers forms p^+n and n^+p Si junctions. Exposing the samples with a red laser at a peak wavelength of 635 nm and with power between ~0.1 to ~1.8 W cm^{-2} induces photovoltaic responses with voltages ranging from 30 to 60 mV.[159]

As mentioned in section 2, amorphous Si dissolves more quickly than monocrystalline Si.[127] A bioresorbable thin-film a-Si solar cell (Figure 18b, left) uses a PIN-doped hydrogenated a-Si layer as the active material, an Al-doped ZnO film as a transparent conductive oxide, Mg as the electrodes (Figure 18b, middle).[18] Boron and phosphorus doping defines p- and n-type regions. Such cells deliver an efficiency of 2.6%, an open-circuit voltage of 0.81 V, and a short-circuit current density of 6.4 mA cm^{-2}, which are comparable to that of a-Si solar cells formed with nonbioresorbable materials (Figure 18b, right).[18]

5. MANUFACTURING TECHNIQUES FOR BIORESORBABLE ELECTRONICS

Specialized manufacturing techniques can form the materials described in section 2 into the devices outlined in section 3 and the power supplies in section 4. A challenge in bioresorbable systems arises from limited compatibility with wet processing steps, particularly those that involve aqueous solutions. Approaches for research purposes rely on combinations of methods in photolithography and transfer printing, physical and chemical vapor deposition through shadow masks, and in some cases additive printing techniques and other solution-based processes. Recent work demonstrates the applicability of laser ablation schemes, as additional options for materials processing and fabrication. This section summarizes these techniques, highlights their advantages and limitations (Table 7), and illustrates some examples of their application in bioresorbable electronics.

5.1. Photolithography, Etching, and Transfer Printing

Si NMs, as discussed in previous sections, or microscale versions of such membranes (i.e., Si micromembranes, or Si MMs), are essential semiconductor materials for almost all high performance bioresorbable electronic devices. Photolithography and wet/dry etching techniques can pattern Si NMs with high resolution (~1 μm) and alignment accuracy (~1 μm) using standard mask aligners available in academic cleanroom facilities and with much higher precision in industrial foundries. Combined with transfer printing for manipulating the resulting Si NM structures, this approach enables routes to a broad range of Si-based bioresorbable passive and active electrical components (refs 8, 10, 18, 38, 145, 152, 154, 159, 285, and 286) (diodes, transistors, CMOS inverters and logic gates) and devices (refs 18, 20, 125, 145, 171, 193, 201, 203, 281, 285, 287, and 288) on various types of bioresorbable polymer substrates, such as silk (ref 8), PLGA (refs 20, 125, 145, 154, 201, 281, and 286), PCL (ref 193), polysaccharides (ref 152), polyanhydride

https://doi.org/10.1021/acs.chemrev.3c00408
Chem. Rev. XXXX, XXX, XXX−XXX

Table 7. Advantages and Limitations of Manufacturing Techniques for Bioresorbable Electronics

manufacturing techniques	advantages	limitations
photolithography, etching and transfer printing	high resolution (~1 μm)	requires cleanroom facilities
	high alignment accuracy (~1 μm)	multistep dry and wet process
	mass production	
vacuum deposition through masking structures	simple process	requires cleanroom facilities
	fine resolution (~10 μm)	high vacuum and/or temperature process
		limited selection of materials
Additive printing	time/cost-effective	limited selections of materials
	mass production	requires postsintering process
		low resolution (>40 μm)
laser ablation	good resolution (~5 μm)	dependent on the absorption properties of materials
	good alignment accuracy (~3 μm)	serial process
	dry process	
	time/cost-effective	
	mass production	

(ref 5), and metal foils (ref 38) (Fe, Zn, Mo). Here, the nonsilicon parts of the devices can be processed directly by patterned deposition, by printing or by schemes analogous to those for the Si-NMs themselves, where integration occurs through a sequence of steps in transfer printing. Examples of complete functional platforms formed in this way include microelectromechanical systems,[5] electrocorticography electrode arrays,[20,125] hydration sensors,[145] pressure sensors,[171,287] temperature sensors,[203,287] electrochemical dopamine monitors,[193] neurochemical analyzers,[288] optical waveguides and biosensors,[201] thin-film solar cells,[18] and photovoltaic microcells.[281] In all cases, water barriers often processed in similar ways[20,21,129,171,203,287] (e.g., transferred layers of thermally grown SiO_2, t-SiO_2, or monocrystalline Si or various polymers or deposited inorganic films) must be included to protect the electronics from surrounding biofluids over time scales relevant to a desired operating period. Passive devices that do not require a semiconductor are also possible, including metal-based thin film devices,[280] in antennas for wireless power transfer on PLGA (Mg coils: 1 cm in diameter, 30 μm thick, 100 μm wide), inductors, capacitors, resistors, and other simple components.

Figure 19a shows a specific, simple example of these types of schemes involving the fabrication procedures for an array of highly doped Si NM structures as electrodes and interconnects for measuring electrocorticographic signals.[125] The fabrication starts with phosphorus doping of the device layer Si on a SOI (~300 nm thick device Si) wafer and removing the buried oxide layer by wet etching with concentrated hydrofluoric acid (HF) to release Si NMs. The next step involves transfer printing of the Si NMs onto a temporary Si substrate with a spin-cast bilayer of poly(methylmethacrylate) (PMMA, ~800 nm thick) and polyimide (PI, ~300 nm thick) and patterning the Si MNs to define the electrodes and interconnects using photolithography and reactive ion etching (RIE) (step 1). Depositing a layer of SiO_2 (100 nm thick) using PECVD and selectively removing this material from the electrode regions forms an encapsulation layer for the Si NM electrodes. Spin-casting a layer of PI (300 nm thick) on top and patterning this layer places the Si NMs near the neural mechanical plane. Patterning a mesh structure through multilayer stacks by RIE and buffered oxide etching (BOE) exposes the base layer of PMMA. Dissolving the PMMA in acetone then releases the system from the temporary substrate (step 2). The next step (step 3) retrieves the device onto a slab of PDMS and removes the bottom exposed layer of PI by RIE. Transfer onto a film of PLGA (~30 μm thick), facilitated by heating to temperatures close to the glass transition of the PLGA (lactide/glycolide ratio of 75:25 composition, 55−60 °C; step 4), and removal of the top layer of PI by RIE (step 5) completes the fabrication. A photograph of a device with four measurement channels, fabricated according to this process, wrapped around a cylindrical tube with a radius of 2 mm, appears in Figure 19b.

Photolithography and transfer printing can also be applied to device components formed in modified process flows executed in a foundry fabrication facility, to allow state-of-the-art integrated circuits/devices with complex structures and functions. A representative example is in bioresorbable forms of CMOS devices on bioresorbable polymer substrates.[154] The layouts involve SOI substrates with a SiN_x passivation, and anchor layer (600 nm thick), a Si device layer (Si active layer ~250 nm thick; gate oxide ~25 nm thick; W vias and metal interconnects with nonbioresorbable Ti/TiN adhesion layers ~300 nm/100 nm thick), and a buried oxide layer (1 μm thick). Scanning electron microscope (SEM) images and schematic illustrations in Figure 19c demonstrate the steps in release and transfer printing onto PLGA substrates. The process begins with CMOS devices (areas colorized with gold) on an SOI wafer formed in a foundry facility according to the specifications mentioned above (step 1). Isolation of device blocks (areas colorized with red) and formation of trenches to the underlaying Si(100) handle wafer (areas colorized with cyan) through the buried oxide layer for undercut etching occurs by photolithography and RIE. A low-stress SiN_x passivation layer (~600 nm thick) formed by PECVD also serves as the material for anchors that tether the CMOS devices to their lithographically defined locations even after undercut etching (step 2). Additional photolithography and RIE steps define the geometries of these anchors, in this example to form tethers at the four corners of each device. The undercut process follows from immersion of devices in tetramethylammonium hydroxide (TMAH; 8.3% TMAH at 85 °C) or potassium hydroxide (KOH; 18% KOH at 70 °C) to anisotropically etch the exposed silicon handle wafer. This process leaves relief structures in pyramid shapes positioned at the centers of the devices (step 3). Transfer printing devices from the source wafer onto a target PLGA polymer substrate (lactide/glycolide ratio of 85:15 composition) completes the fabrication. Figure 19d shows a photograph of bioresorbable logic gates on a thin film of PLGA, fabricated using these processes, wrapped onto a glass cylinder.

5.2. Vacuum Deposition through Masking Structures

Physical vapor deposition through shadow masks, commonly made of flexible films of PI, is a simple alternative to photolithography and etching or liftoff, with practical levels of resolution that can reach into the micrometer range (~10 μm). Bioresorbable materials that can be processed in this way include

https://doi.org/10.1021/acs.chemrev.3c00408
Chem. Rev. XXXX, XXX, XXX−XXX

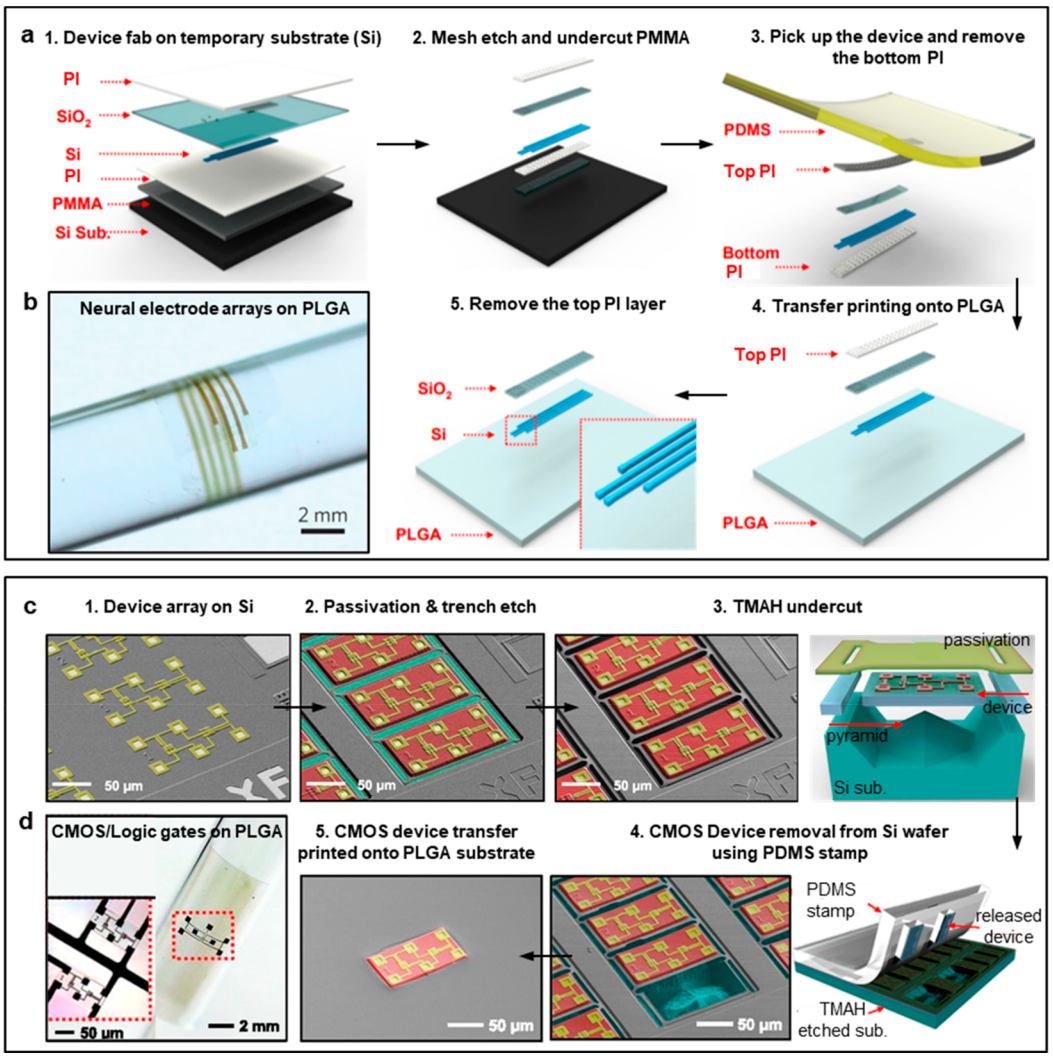

Figure 19. Photolithography, etching, deposition, and transfer printing processes. (a) Schematic illustrations of key steps in the fabrication of a bioresorbable array of electrodes for monitoring neural processes: (1) transfer printing of highly n-doped Si-NMs on a silicon substrate coated with PMMA and PI, followed by coating with SiO_2 and another layer of PI, (2) defining a mesh structure by photolithography, etching by RIE, and immersion in BOE, (3) dissolving the PMMA, retrieving the structure onto a PDMS slab, and removing the bottom PI using RIE, (4) printing the structure onto a bioresorbable substrate (PLGA), and (5) removing the top PI layer. (b) A photograph of a bioresorbable neural electrode array with four channels wrapped around a cylindrical tube with a radius of 2 mm.[125] Reproduced with permission from ref 125. Copyright 2016 Springer Nature. (c) SEM images and schematic illustrations of key processing steps in release and transfer printing of device components produced in a foundry fabrication facility on an SOI wafer to a substrate of PLGA. The colorized regions correspond to the device array (gold), the released region of individual device blocks (red), and the underlying silicon (100) handle wafer (cyan). (d) A photograph of bioresorbable logic gates on a thin film of PLGA wrapped onto a glass cylinder (inset: magnified view of the interconnected MOSFETs).[154] Reproduced with permission from ref 154. Copyright 2017 United States National Academy of Sciences.

a range of insulators[35,98,139,171] (SiO, 600 nm; MgO, 100−150 nm; ZnO, 350−500 nm; MoO_3, 1 μm) and metals[28,76,98,178,181,227,238,276,289,290] (Mg interconnections, 50−500 nm; electrodes, Mg, 3.5 μm thick, size ∼4.7 mm × 3 mm; Fe, 200 nm thick, Mo, 150 nm thick). Examples are resistors and RF coils[139,291] (serpentine Mg resistors, 200 nm thick, 50 μm wide, 100 μm distance; Mg coils, 2 μm thick, 200 μm wide, 200 μm distance, size: 8 mm × 8 mm), energy harvesters and storage units (batteries, supercapacitors, triboelectric nanogenerators),[28,98,227,238,276,290] wireless heating devices for drug delivery,[139] strain and pressure sensors,[98,178,181,291] and metal-based electrode arrays for pressure sensing.[76] Representative examples of bioresorbable devices fabricated using this technique are in ZnO-based transistors and mechanical energy harvesters.[98] In this case, processing of all of the constituent materials, including ZnO (semiconductor, active material for the transistors, and energy harvesters, 200 nm thick), Mg (electrodes, contacts and interconnects, 150 nm thick), and MgO (gate and interlayer dielectrics, 100 nm thick), involves direct vacuum deposition onto silk substrates (∼25 μm thick) through masks made of PI (12.5 μm thick) with feature sizes of 20 μm.

5.3. Additive Printing

For materials available in the form of particles, liquid inks, or pastes, direct printing methods can be attractive. Examples are in Zn and W particles[41,46,49,50,170,292−295] and PEDOT:PSS pastes[296] patterned by screen printing (feature size ∼100 μm),[46,49,50,292,294] laser printing (feature size ∼40 μm),[170] and aerosol printing (feature size submillimeter).[293] The conductivity of the resulting printed structures follows from transport through percolating networks, in some cases enhanced

https://doi.org/10.1021/acs.chemrev.3c00408
Chem. Rev. XXXX, XXX, XXX−XXX

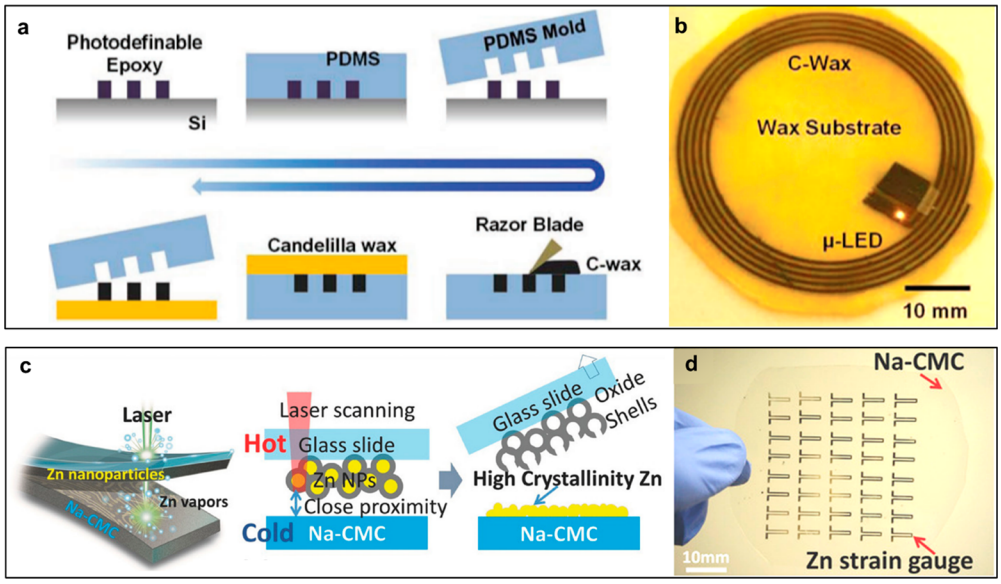

Figure 20. Screen and laser printing techniques. (a) Illustration of a screen-printing process to form a conducting-wax-based RF inductive coil on a candelilla wax substrate. (b) Wireless power delivery through the inductive coil to operate an LED.[46] Reproduced with permission from ref 46. Copyright 2018 Wiley-VCH. (c) Illustration of a laser printing process. (d) Photograph of resistive Zn strain gauges formed by laser printing on Na-CMC.[170] Reproduced with permission from ref 170. Copyright 2017 Wiley-VCH.

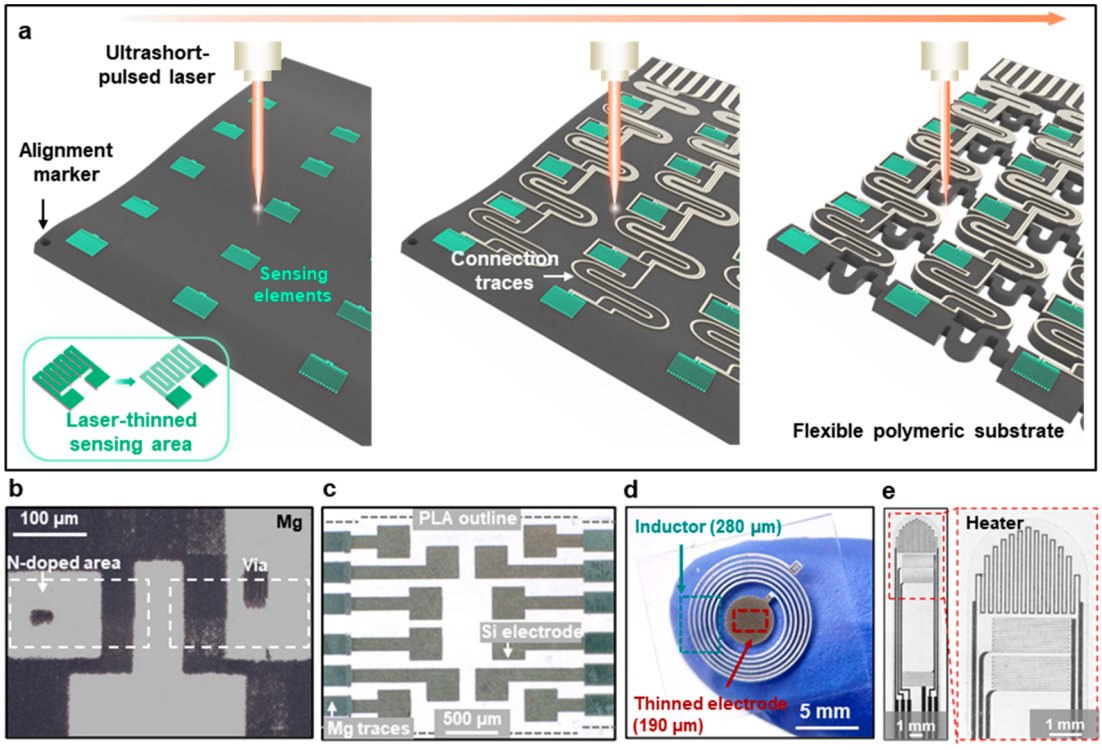

Figure 21. Laser ablation technology (combined with transfer printing and vacuum evaporation). (a) Illustration of the laser ablation process: patterning of sensing elements (area colored with green) and structuring of alignment markers (left), patterning of interconnection traces (area colored with gold; middle), and structuring substrates (areas colored with gray) into stretchable forms (right). (b) Photograph of a Si-based MOSFET. (c) Photograph of flexible Si-based electrode arrays on a PLA substrate for biopotential recordings. (d) Photograph of an Mg inductor with thinned bottom electrode for a pressure sensor. (e) Photograph of a Mg resistive flow sensor probe with a narrow, needle-shaped geometry.[157] Reproduced with permission from ref 157. Copyright 2022 Springer Nature.

by sintering processes, as described in section 2, and in other publications for cases of bioresorbable materials.[41,297] These techniques can form conductive interconnects,[49] resistors,[292] RF antenna structures,[41,46,50,170,293,294] strain gauges,[170] and others.

Screen printing is useful in the fabrication of circular RF antennas,[46] as shown in Figure 20a. The printing procedures include forming of a PDMS mold by soft lithography, casting of wax−tungsten composite inks (tungsten particles: 4−6 μm in diameter) to fill the PDMS mold, and transferring the printed

https://doi.org/10.1021/acs.chemrev.3c00408
Chem. Rev. XXXX, XXX, XXX−XXX

inductive coil on a wax substrate by drop casting of wax on top. The feature sizes of wax−tungsten lines formed in this way vary from 100 μm to 1 mm. State-of-the-art screen printing systems can reach feature sizes into the range of 30−50 μm.[297] Figure 20b shows a wax-based inductive coil (line width ∼0.7 mm, outer diameter ∼53 mm) fabricated by screen printing, integrated with LEDs for wireless power.

Another example, featured in Figure 20c, illustrates the processes of laser printing of Zn strain gauges on films of Na-CMC.[170] The fabrication begins with pressing a thin layer of Zn (2.5−5 μm thick, consisting of Zn nanoparticles) on a transparent glass slide onto a Na-CMC substrate. The output of a continuous-wave fiber laser guided by a mirror on a galvanometer passes through the glass slide to thermally evaporate the Zn as the basis for direct printing of Zn traces (line width ∼40 μm, thickness ∼submicrometer, conductivity $\sim 1.124 \times 10^6$ S m^{-1}) on the receiving Na-CMC substrate. Figure 20d shows resistive Zn strain gauges (gauge factor ∼1) formed in this manner.

5.4. Laser Ablation

Patterned laser ablation offers a simple alternative to photolithography and transfer printing, and other printing techniques. The result enables materials processing in an accurate and effective manner, without the use of wet chemistries or solvents, for patterning of multilayered structures across large-areas (a few tens of centimeters) with high throughput. Standard tools for laser ablation offer high alignment accuracy (2−3 μm) with feature sizes down to a few micrometers (∼5 μm).[157] The key parameters for ablation include average power (80−200 mW), scanning speed (100−1000 mm s^{-1}), and frequency (40−200 kHz), number of repetitions (≥1), ablation grid distance (≥2 μm) and scan path (along x-axis, y-axis, or x- and y-axis). For example, with commercial tools for laser ablation in the printed circuit board industry, Si NMs can be patterned at areal rates of ∼10−30 s cm^{-2} with optimized ablation parameters and a minimum reduction in thickness of 35 nm per pass. Such processing is compatible not only with Si NMs but with a range of bioresorbable materials because it avoids the need of any wet processing steps and limits the length of heat-affected damage zones (∼15 nm) due to the use of ultrashort pulsed lasers (∼10 ps). A broad range of materials, ranging from conductors (Mg, Mo, Zn, Fe, W, 0.1−250 μm thick),[22,23,25,26,157,168,169,225,228,275] semiconductors (Si NMs/MMs, 0.5−2 μm thick),[157] dielectrics (SiO_2, SiN_x, 100−200 nm thick),[157] to polymer encapsulants and substrates[29,157] (polylactic acid, cellulose acetate, PLGA, polyurethane, and others, 10−50 μm thick) can be processed by thinning,[157] cutting,[22,26,29,157,168,169,225] and patterning.[157,275] Demonstrations in bioresorbable device fabrication span diodes and MOSFETs,[157] batteries,[225,228] flow sensors,[26,157] temperature sensors,[157,168] pressure sensors,[157,169] strain sensors[157] to cardiac pacemakers,[22,25] electrical stimulators,[23,157,275] and wireless drug delivery systems.[29]

Figure 21a shows procedures for fabrication of bioresorbable electronic devices,[157] from the patterning of sensing elements and structuring of alignment markers (left) to the definition of connection traces (middle) and cutting of substrates into stretchable forms (right). For the example shown in Figure 21b, fabrication of a Si-based n-channel MOSFET begins with ablation to pattern a Si MM (2 μm thick) on a SOI wafer after processing to form doped regions for source and drain contacts. Deposition (PECVD) of a uniform SiO_2 dielectric layer (100 nm thick) followed by ablation of this layer defines shapes with two openings for metal interconnections. EBPVD forms a uniform Mg layer (50 nm thick) that yields, by laser ablation, three connection pads (dimension: 160 μm × 580 μm) as electrodes. Cutting the SOI substrate completes the fabrication. Tight control of the process minimizes damage to underlying materials due to patterning of overlying layers. For example, when patterning a three-layer structure consisting of top Mg layer (300 nm thick), middle Si MM layer (500 nm thick), and bottom PLA substrate layer (50 μm thick), ablating the Mg and Si leads to an ablated thickness of ∼50 nm for the underlying Si layer and ∼80 nm for the underlying PLA layer, respectively.

Similar schemes can be used to form other classes of devices, from flexible Si-based electrode arrays on PLA substrates for biopotential recordings to Mg inductors with thinned bottom electrodes for pressure sensors and Mg resistive flow sensor probes with a narrow, needle-shaped geometries, shown in parts c−e of Figure 21, respectively.[157] The fabrication of flexible Si-based electrode arrays (Figure 21c) for biopotential recording begins with pattering of the n-doped Si MM (2 μm thick) into an array of electrodes (12 electrodes) on a PLA substrate (50 μm thick), followed by ablation of the evaporated Mg layer (1 μm thick) to define connection traces and cutting the PLA substrate into a ribbon shape. Thinning of the Mg layer (280 μm thick) to reduce the thickness of the central circular area (4 mm in diameter; thickness decrease from 280 to 190 μm) for the bottom electrode, and ablation of the surrounding Mg to define a helical coil structure forms an inductor with thinned bottom electrode of a pressure sensor (Figure 21d). Ablating the Mg layer (180 nm thick, EBPVD) on a PLA substrate (50 μm thick) defines four resistive-type devices and cutting the PLA substrate complete the fabrication of a Mg resistive-based flow sensor with a narrow, needle-shaped geometry (Figure 21e).

6. BIORESORBABLE INTEGRATED SYSTEMS AND CLINICAL APPLICATIONS

Integrating bioresorbable components and sensors (section 3) and power supplies (section 4) yields bioresorbable systems that provide diagnostic or therapeutic functions for clinical applications. Figure 22 illustrates the scope of clinical applications for bioresorbable electronics. The U.S. Food and Drug Administration (FDA) currently recommends assessments of *in vivo* degradation for medical implants designed to be bioresorbable or biodegradable, according to the International Standards Organization (ISO).[32] ISO10993 standards encompass a comprehensive list of tests and protocols devised to facilitate the systematic assessment of implantable devices. Among these, key evaluations include investigation of cytotoxicity for cell damage, irritation for inflammatory responses, sensitization for allergic reactivity, systematic toxicity for effects on organs due to chemical constituents, carcinogenicity for development of cancer cells, implantation for effects on localized tissues, hemocompatibility for effects on blood, and degradation for resultant byproducts.[298] Through biological responses in accordance with these standards, some of the materials (e.g., Mg, Mg alloys, Fe, Zn, silk, PGA, PLGA, PLLA, PVA) previously noted in section 2 have been approved from the FDA. The FDA has not, however, assessed bioresorbable electronic systems, to our knowledge.

6.1. Diagnostic Platforms

6.1.1. Brain Monitoring. Monitoring the neurophysiology of the brain is important as an essential diagnostic basis for the assessment of patient health and postoperative brain disorders,

https://doi.org/10.1021/acs.chemrev.3c00408
Chem. Rev. XXXX, XXX, XXX−XXX

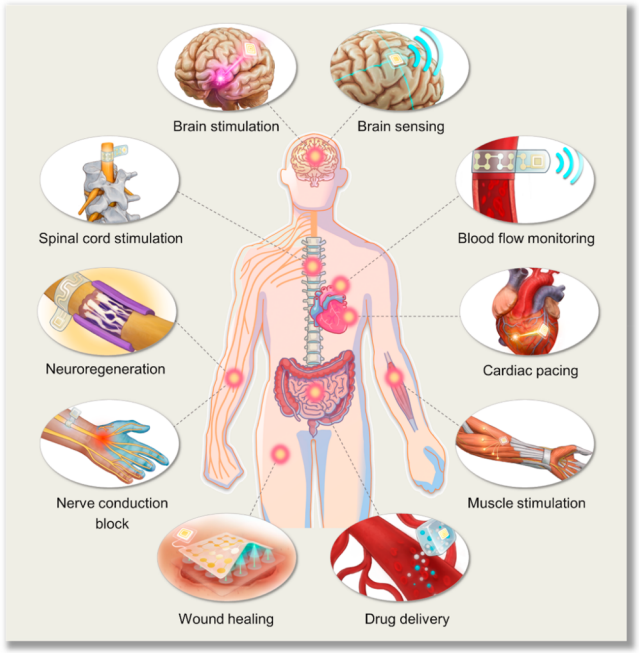

Figure 22. Illustration of the scope of clinical applications for implantable and bioresorbable electronics.

such as traumatic brain injury, glaucoma, hypertension, hyperthermia/hypothermia, and degenerative brain diseases. Recently reported bioresorbable interfaces for such purposes allow mapping of neural activity and sensing of intracranial pressure, temperature, and neurochemicals.

In a first example, actively multiplexed devices enable high resolution and high channel count (8 × 8 arrays; 64 electrodes) neural interfaces, for transient spatiotemporal mapping of electrical activity from the cerebral cortex (Figure 23a).[125] One embodiment consists includes up to 128 n-channel MOSFETs (single electrode with two MOSFETs), built with highly doped Si NMs (10^{20} cm^{-3}, 300 nm thick) for the neural interface electrodes and/or Si NMs with patterned doping regions as the active semiconducting layers, Mo (300 nm thick) for the source, drain and gate electrodes, SiO_2 (100 nm thick) for the gate dielectrics, Mo (300 nm thick) for the interconnects, trilayers of $SiO_2/Si_3N_4/SiO_2$ (300/400/300 nm thick) for the interlayer dielectrics/encapsulation structures, and PLGA (30 μm thick) for the substrate. These platforms record physiological activity in the form of ECoG and subdermal encephalography (EEG) both in acute and chronic situations. The spatial distribution of the amplitude of the evoked potentials measured at the cortical surface of rat models demonstrates an ability for high speed, high-resolution recording schemes for several days with high signal-to-noise ratio.

Si NMs are attractive for these systems not only because of their favorable electronic properties but also because of their mechanical flexibility, to allow conformal contact with the complex and time dynamic brain tissues. This flexible characteristic can also be exploited for real-time monitoring of intracranial pressure (ICP) using strain gauges, suspended membranes, and enclosed air cavities. Recently reported pressure sensors of these types show measurement accuracies that compare to those of the clinical standards through *in vivo* experiments for up to 25 days (Figure 23b).[171] The specific devices for those studies consist of four sensors based on Si NMs (200 nm thick) as strain and temperature gauges, along with thermally grown layers of SiO_2 (10 nm thick) as encapsulation. The sensing mechanism follows from gauges that partially extend over an air-filled cavity, such that fluctuations in pressure of the surrounding cerebrospinal fluid induce measurable deflections of the membrane that seals the cavity. *In vivo* studies using rodent models demonstrate excellent responses of the sensor with absolute accuracy within ±2 mmHg in the intracranial space.

Wireless operation is often an additional requirement for clinical use. Examples of temperature sensors for the brain[9,168,171] use a wireless, LC-resonant passive scheme with a detection range of ∼2 cm, a precision of <0.05 °C, and an accuracy of 0.5 °C.[168] This system consists of PLGA (10 μm thick) as the substrate, candelilla wax (200−500 μm thick) as the encapsulation, Mg foil (100 μm thick) as the electrode for an inductor, a mixture of W and natural wax (weight ratio of 15:1) as the interconnects, and Mg/PEG/Mg (100/50/100 μm thick) as the capacitor (Figure 23c). For temperatures near those of the body (i.e., 34−42 °C) changes in the dielectric constant of PEG lead to corresponding changes in the capacitance, and thus the resonant frequency of the LC oscillator, as described previously. Demonstrations include measurements of brain temperature in rat models for 4 days, with performance similar to that of a commercial temperature sensor.

Real-time monitoring of the concentration of neurotransmitters (e.g., dopamine, epinephrine, and noradrenaline) can be important for evaluating degenerative brain diseases as well as regulating essential functions in the body. Recent reported electrochemical sensors serve as neurochemical analyzers that are implantable and fully bioresorbable, for wireless detection of dopamine (related to nervous system disorders including Parkinson's disease, attention deficit hyperactivity disorder, schizophrenia).[193,288] One example employs doped mono-Si NRs (10^{19} cm^{-3}, 300 nm thick) as current collectors, 2D TMDs (i.e., MoS_2 and WS_2, 40−160 nm thick) as active sensing electrodes, Fe nanoparticles (5 nm size) as catalysts, Mg (1 μm) as interconnects, SiO_2 (100−150 nm thick) as interlayers/insulations and PLGA as the substrate (i.e., probe type) and encapsulation (Figure 23d).[288] When positively charged dopamine molecules adsorb onto the negatively charged TMDs-Fe surface by electrostatic interaction, Fe catalyzes the accumulated dopamine to its oxidized form (i.e., dopamine quinone). Electrons generated by this process transfer to the highly conductive Si NRs electrodes, leading to changes in electrical signals that depend on the concentration of dopamine. A wireless communication system consists of Mg film (1 μm) for a RF coil and interconnects, PLGA for the dielectric and substrate, and electronic components for nonbioresorbable part. The system connects to the active sensing probe and allows transmit the measured, time-dynamic responses of the neurochemicals for 2−4 weeks *in vivo*.

6.1.2. Blood Flow Monitoring. Postsurgical monitoring of blood vessel patency is critical to patient recovery after reconstructive surgeries and following discharge from the hospital. Bioresorbable devices for monitoring blood flow[26,35] can be useful in this context, with the potential to eliminate complications and costs associated with surgical extraction.

Section 3 describes various types of bioresorbable pressure sensors based on piezoresistive and LC circuit designs. One such sensor adapted for monitoring blood flow (Figure 24a, left) consists of a fringing-field capacitive component connected to a bilayer coil structure as an inductor.[26] Pulsed blood flow induces changes in vessel diameter and, thus, the capacitance to cause changes in the resonant frequency of the LC oscillator. Such

https://doi.org/10.1021/acs.chemrev.3c00408
Chem. Rev. XXXX, XXX, XXX−XXX

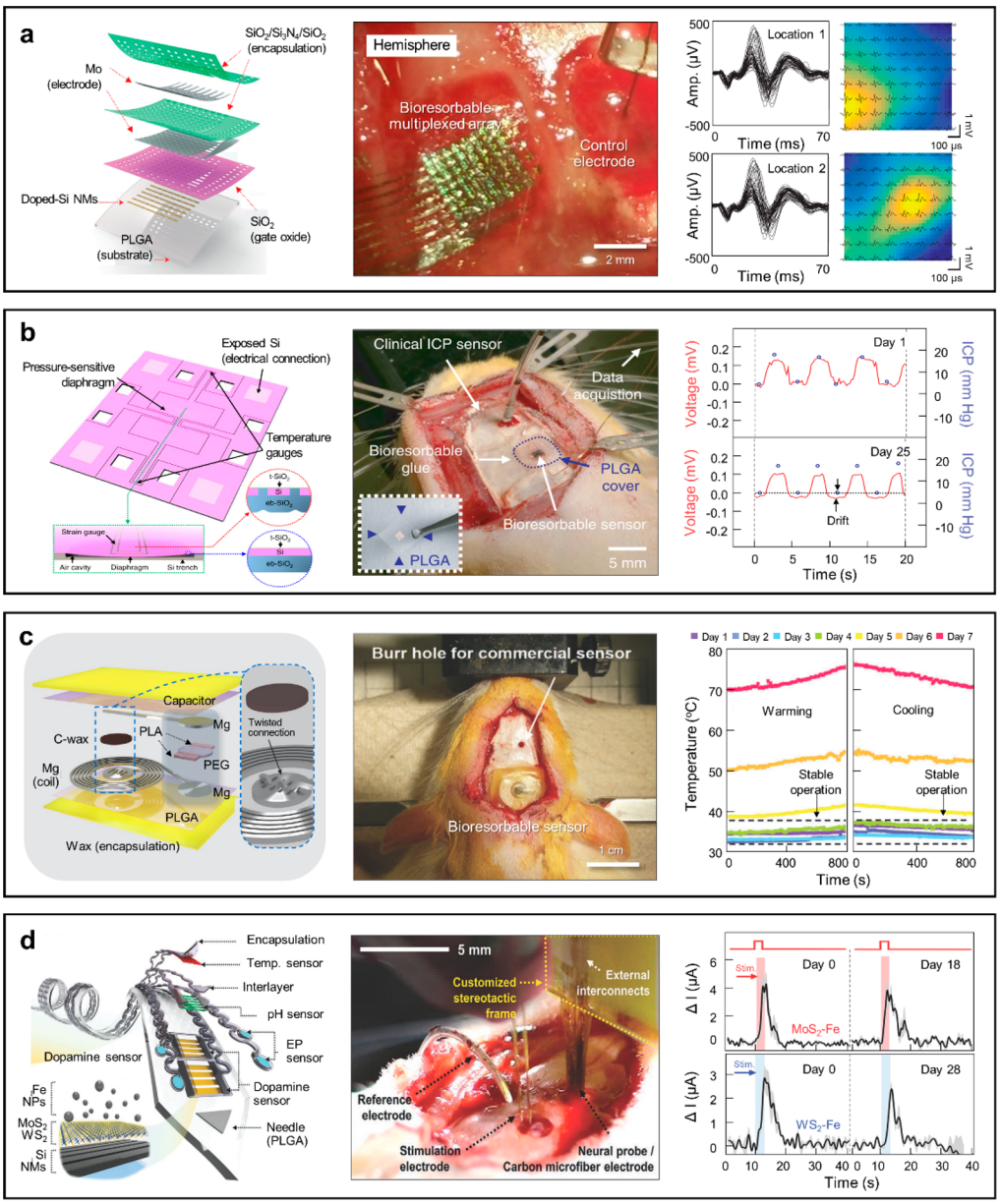

Figure 23. Bioresorbable sensing systems for the brain. (Left) Schematic exploded-view illustrations of representative devices. (Middle) Photographs showing the implantation of these devices into or onto the brain, or in the intracranial space. (Right) Experimental data collected *in vivo*. (a) An actively multiplexed neural electrode array for recording electrophysiological signals from the cerebral cortex (contact electrode, doped-Si; interconnect, Mo; encapsulation, SiO_2 and Si_3N_4; substrate, PLGA). An 8 ×8 array actively multiplexed array (64-channel) can measure the spatial distribution of potentials evoked by different stimuli.[125] Reproduced with permission from ref 125. Copyright 2016 Springer Nature. (b) A sensor composed of Si and SiO_2 for monitoring ICP. Stable operation is possible for up to 25 days postimplantation, with a negative drift of ~3 mmHg.[171] Reproduced with permission from ref 171. Copyright 2019 Springer Nature. (c) A sensor for measuring temperature in the intracranial space (inductor, Mg; capacitor, Mg/PEG/Mg; encapsulation, candelilla wax). Stable operation is possible for 4 days.[168] Reproduced with permission from ref 168. Copyright 2020 Wiley-VCH. (d) A sensor for detecting a neurotransmitter (i.e., dopamine) (electrode, doped-Si; interlayer, MoS_2 or WS_2; catalyst, Fe nanoparticles). Stable operation is possible for 2−4 weeks.[288] Reproduced with permission from ref 288. Copyright 2022 Wiley-VCH.

changes can be wirelessly monitored via inductive coupling to an external coil. The constituent materials include Mg for electrical interconnects, PGS as a dielectric layer, POMaC and PHB/PHV as packaging layers, a PLLA spacer for the bilayer coil structure, and a UV-cured bioresorbable sealant.[26] Figure 24a (middle) shows wireless operation *in vivo* with a Sprague−Dawley rat. Figure 24a (right) presents the measured changes in resonant frequency. The peaks coincide with artery expansion during cardiac cycles (3.47 bps), as a manifestation of arterial pulse waves.[26]

Section 3 also introduces designs for thermoresistive flow sensors. One example of use in sensing blood flow, shown in Figure 24b (left), includes integration as a bioresorbable electronic stent (BES) with multifunctional capabilities that also include temperature monitoring, wireless data transmission, drug delivery, and hyperthermia therapy.[35] The thermoresistive flow sensor consists of a long filamentary Mg resistor, a ZnO adhesion layer, and MgO and PLA encapsulation layers. Inserting BES in the canine aorta allows measurements of the blood fluid velocity through thermoresistive effects. Figure 24b

https://doi.org/10.1021/acs.chemrev.3c00408
Chem. Rev. XXXX, XXX, XXX−XXX

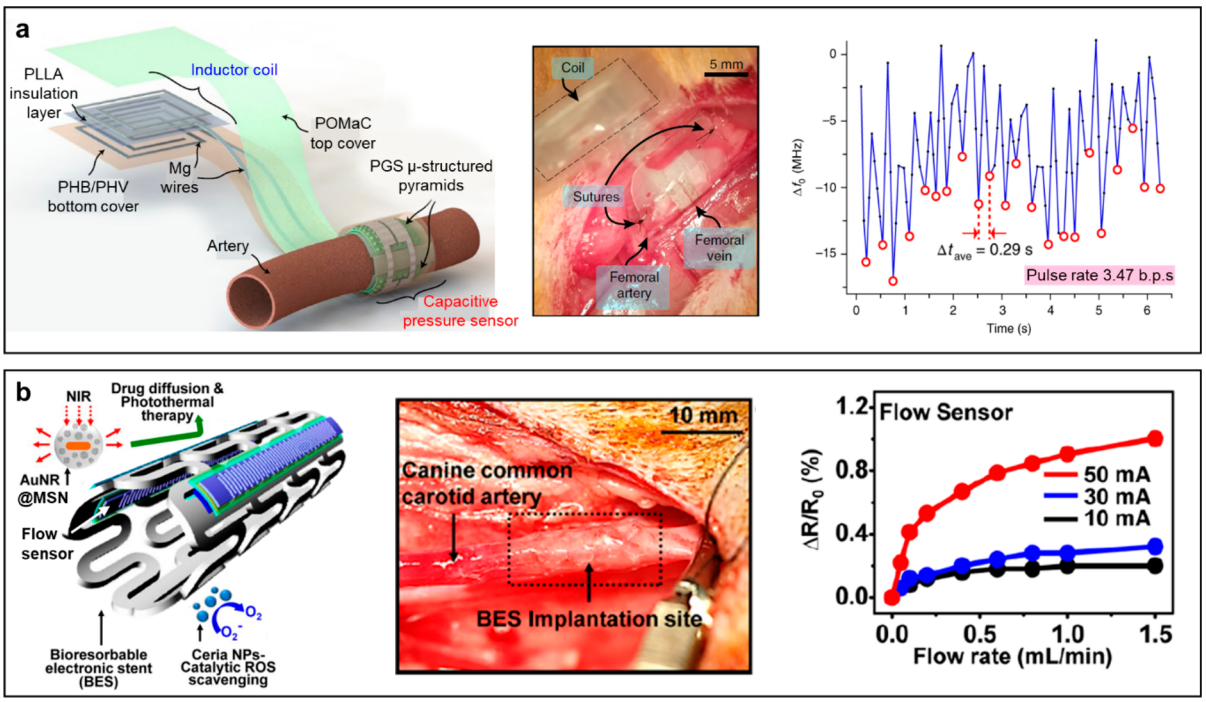

Figure 24. Examples of bioresorbable systems for blood flow monitoring. (a) Schematic illustration (left), implantation in the rat (middle, wrapped around the femoral artery), and a plot of Δf_0 measured *in vivo* versus time (right) of a wireless arterial-pulse sensor.[26] Reproduced with permission from ref 26. Copyright 2019 Springer Nature. (b) Schematic illustration (left), implantation in the canine common carotid artery (middle), and a plot of the percentage change in resistance of a flow sensor (right) of a bioresorbable electronic stent (BES).[35] Reproduced with permission from ref 35. Copyright 2015 American Chemical Society.

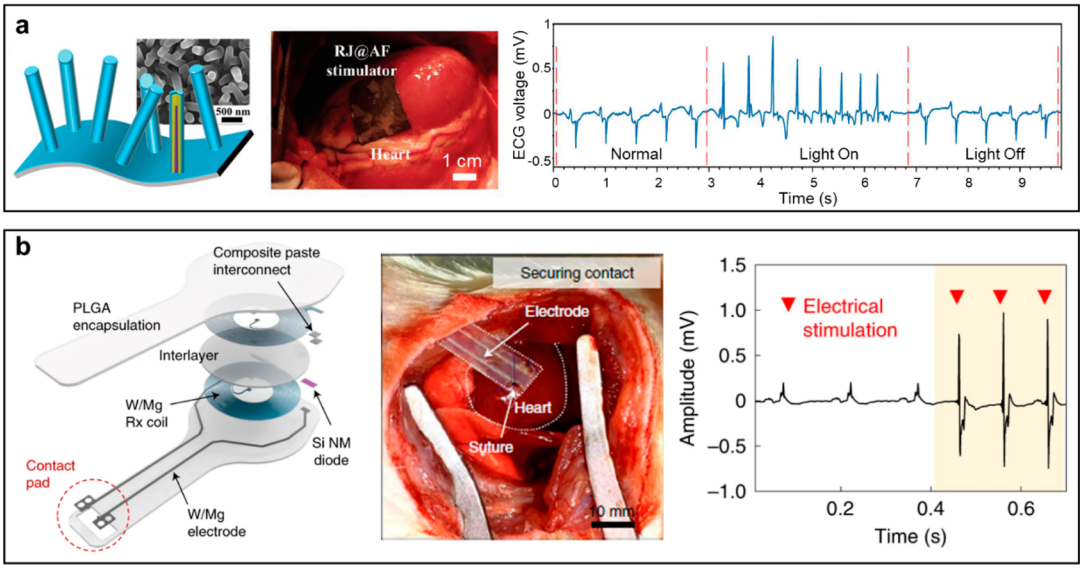

Figure 25. Examples of bioresorbable systems for temporary cardiac pacing. (a) Schematic illustration (left), implantation (middle), and ECG signals recorded before, under, and after light stimulation (right) of a photoelectric cardiac stimulator based on a-Si:H radial junctions (RJs).[27] Reproduced with permission from ref 27. Copyright 2020 Wiley-VCH. (b) Schematic illustration (left), implantation (middle), and ECG signals recorded before and during electrical stimulation (right) of an RF-powered cardiac pacemaker.[22] Reproduced with permission from ref 22. Copyright 2021 Springer Nature.

(middle) shows the device in an expanded state in the carotid artery. Figure 24b (right) plots the change in the resistance of the sensor at different flow rates.[35]

6.2. Therapeutic Platforms

6.2.1. Cardiac Pacing. Temporary cardiac pacing is necessary for patients at risk for bradycardia following an open-heart surgery, heart attack, side effects of medications, or infection.[22] Standard devices involve percutaneous leads and external wired power supplies and monitoring systems, with requirements for device extraction surgeries. This engineering approach can lead to complications such as myocardial injury and infections; it also imposes limitations on patient mobility. Bioresorbable cardiac pacemakers, particularly those that operate in a wireless fashion, can circumvent these challenges.

https://doi.org/10.1021/acs.chemrev.3c00408
Chem. Rev. XXXX, XXX, XXX−XXX

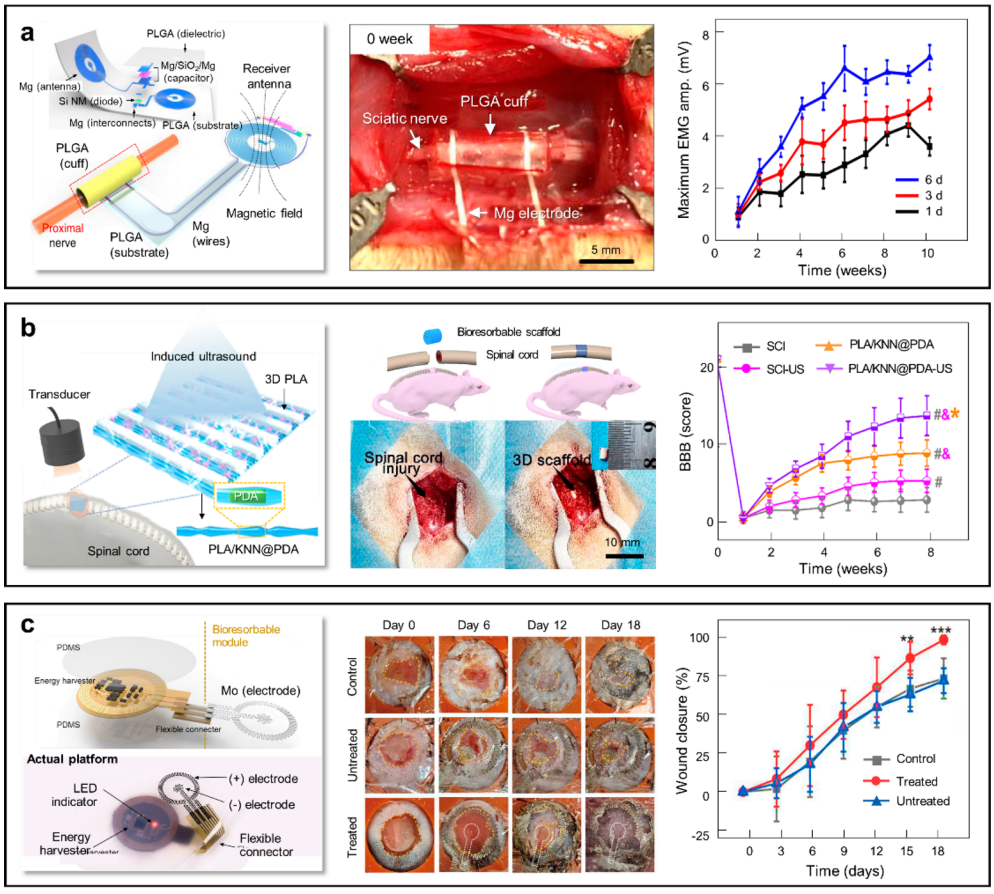

Figure 26. Bioresorbable electrotherapeutic systems for accelerated healing. (Left) Schematic illustrations of representative devices. (Middle) Photographs showing the implantation of these devices into the body. (Right) Experimental data collected *in vivo*. (a) RF-powered wireless, electrical nerve stimulator for accelerating neuroregeneation of an injured nerve (inductor, Mg; capacitor, Mg/SiO_2/Mg; diode, doped-Si; cuff electrode, Mg; substrate/cuff, PLGA). A thin, flexible cuff electrode wraps around the nerve to provide electrical stimulation (pulse, 200 μs; frequency, 20 Hz; over a minimum threshold voltage) for one hour per day for a total of 6 days. Multiple electrical stimulation events enhance the therapeutic effects.[24] Reproduced with permission from ref 24. Copyright 2018 Springer Nature. (b) Ultrasound-powered wireless, piezoelectric 3-dimensional (3D) scaffolds for promoting repair of an injured spinal cord (sheet, PLA/KNN@PDA; microchannel, PLA). Irradiation with ultrasound serves as a remote mechanical stimulus that generates electrical stimulation transduced by a piezoelectric composite structure. Treatment using 3D scaffolds for 8 weeks shows improved functional recovery.[77] Reproduced with permission from ref 77. Copyright 2022 American Chemical Society. (c) Battery-free, wireless platform for electrotherapy at wound sites (electrode: serpentine layouts of Mo). Electrostimulation (DC voltage, 1.1 V) for 30 min/day accelerates wound closure. 86%, 63%, and 66% closures on day 15 for the treated (red), untreated (blue), and the control group (gray), respectively.[300] Reproduced with permission from ref 300. Copyright 2023 American Association for the Advancement of Science.

One type of bioresorbable cardiac stimulator relies on photovoltaic effects in hydrogenated a-Si (a-Si:H) radial junctions (RJs) (Figure 25a, left) formed by growing Si nanowires on the aluminum foil.[27] Attaching the RJ@AFs to the surface of a porcine heart enables *in vivo* pacing (Figure 25a, middle) by illumination with 650 nm laser light, as indicated through electrocardiogram (ECG) signals (Figure 25a, right). In this example, illumination increases the heart rate from 101 beats per min (bpm) to about 128 bpm. Due to limitations in light penetration, implanted optical fibers must be used to deliver sufficient light for cardiac pacing.[27] Bioresorbable fibers of the type described in section 3 might provide an attractive choice for future work.

A fully implantable and wirelessly operated cardiac pacemaker based on RF inductive powering solves these challenges (Figure 25b, left).[22] A device for this purpose consists of W-coated Mg (W/Mg) dual coils as the harvesting antenna (disk-shaped coils, 17 turns, 25 mm in diameter) with a resonance frequency of ~13.5 MHz, a PLGA film as the dielectric interlayer, a Si NM PIN diode for rectification, and W/Mg electrodes for pacing. Figure 25b (middle) shows implantation of such a pacemaker as part of a chronic *in vivo* study in a rat model.[22] Figure 25b (right) indicates successful pacing as evidenced from ECG signals before and during electrical stimulation.[22] Requirements for external power supplies and ECG monitoring equipment can be eliminated by use of a soft, battery-powered device that mounts on the skin of the chest, above the location of the implanted pacemaker.[25] This combination of wireless devices enables closed-loop operation for rate-adaptive and autonomous pacing.

6.2.2. Tissue Regeneration. Similar to the example used in cardiac pacemakers, bioresorbable electrical stimulators can be applied to various forms of electrotherapy. For instance, Figure 26a shows wirelessly powered nerve stimulators for accelerated neuroregeneration of injured, peripheral nerves.[24] A typical platform consists of a collection of a diode, a capacitor, a RF receiver coil, and nerve cuff electrodes: diode−boron and phosphorus doped monocrystalline Si NMs (320 nm thick) with Mg electrical pads (300 nm thick); capacitors, SiO_2 dielectric (600 nm thick) between two Mg plates (50 μm thick); RF receiver coils, a Mg loop antenna (18 turns, 50 μm thick) with a

https://doi.org/10.1021/acs.chemrev.3c00408
Chem. Rev. XXXX, XXX, XXX−XXX

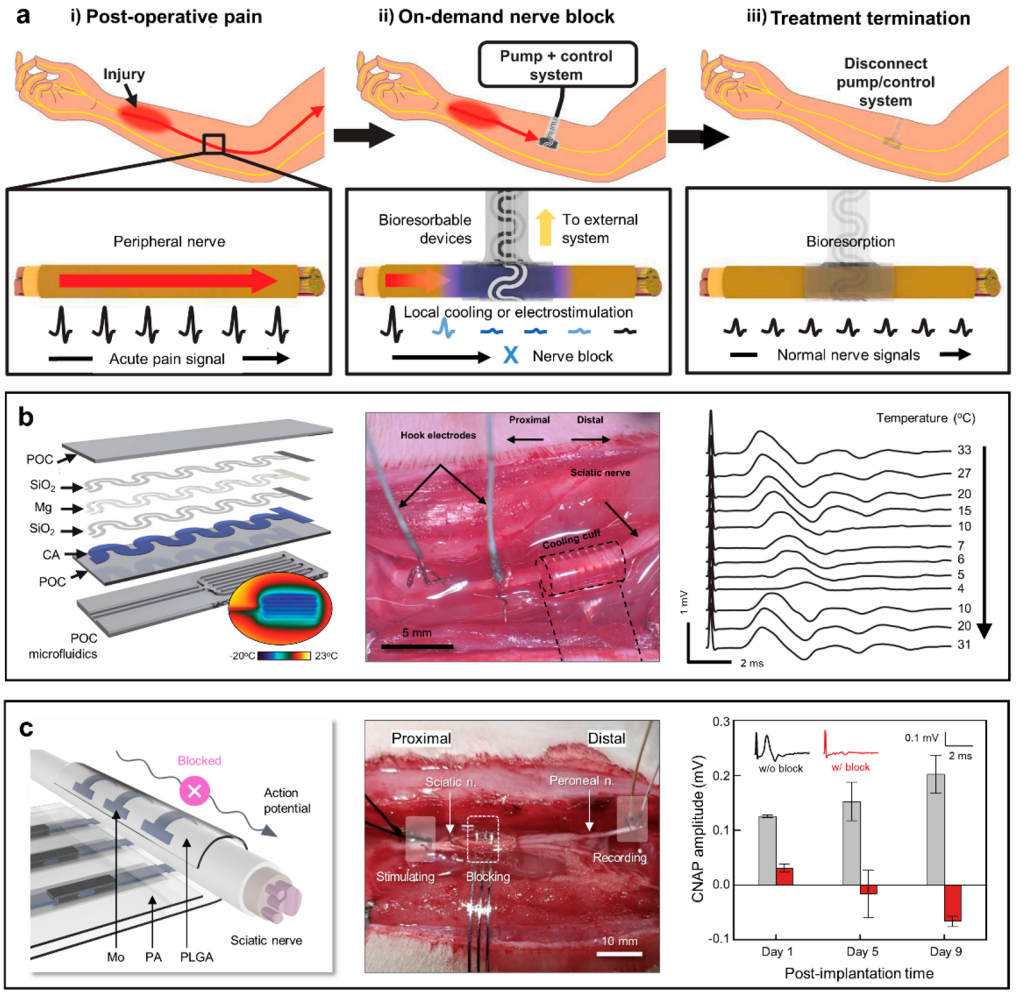

Figure 27. Bioresorbable thermal/electrical stimulators for nerve conduction block. (a) Conceptual illustration of the use, working mechanism, and bioresorption of the devices. (i) propagation of postoperative acute pain signals through peripheral nerves; (ii) local cooling or electrostimulation of peripheral nerves for on-demand nerve conduction block; (iii) treatment termination and bioresorption after completion of the healing process.[11] Reproduced with permission from ref 11. Copyright 2022 American Association for the Advancement of Science. (b) Schematic exploded-view illustration of a microfluidic/electronic system for nerve block via local cooling (left) (resistor, SiO_2/Mg/SiO_2; interconnect, Mg; microfluidics/encapsulation, POC). Experimental setup for in vivo electrophysiology studies (middle). Amplitude of CNAP decreases with reduced temperature and signal latency subsequently recovers upon rewarming (right); Nerve conduction block appears at around 4 °C.[11] Reproduced with permission from ref 11. Copyright 2022 American Association for the Advancement of Science. (c) Schematic illustration of a peripheral nerve stimulator for nerve block under kilohertz frequency alternating current (left) (electrode, Mo and Mg; encapsulation, PA; cuff, PLGA). Experimental arrangement of electrodes for in vivo electrophysiology studies (middle). Changes in CNAP amplitudes under electrostimulation (AC; frequency, 25 kHz; voltage, 10 V_{pp}) for 9 days (right).[23] Reproduced with permission from ref 23. Copyright 2022 American Association for the Advancement of Science.

bilayer, dual coil configuration; PLGA substrates (30 μm thick) with electrical interconnections (Mg, 2.5 μm thick; magnetron sputtering deposition), and PLGA (30 μm thick) or candelilla wax (300 μm thick) encapsulants. Nerve cuffs consist of two Mg electrodes and a hot-pressed, tubular-structured PLGA to facilitate surgical implantation and to ensure conformal contact with the nerve interface. Power transmission occurs via inductive coupling to an external, powered coil. This coil serves as a transmission antenna to transmit power to the RF receiver coils of the implant. The diode rectifies the received alternating current to yield a direct current that can be delivered to the nerve cuff as electrical stimulation to the interfaced region of the nerve. Multiple episodes (1 h per day for 6 days) of electrostimulation (pulse, 200 μs; frequency, 20 Hz; over a minimum threshold voltage) during the therapeutic process of a damaged peripheral nerve in rodent models demonstrates enhanced axonal regeneration and functional nerve recovery.

Not only can the devices be designed for operation over these relatively long timeframes, but they can also be configured, through appropriate materials selections, for only timeframes (typically ≥1 h) suitable for use in the immediate postoperative period.[79] One strategy involves encapsulation with two different bioresorbable formulations of PA, to enable operational lifetimes of only 3 days. Here, an inner layer (20 μm thick) releases an acidic moiety (i.e., carboxylic acid) to accelerate dissolution of the electronic materials such as the Mg-based electrodes (40 μm thick) via $2H^+ + Mg \rightarrow Mg^{2+} + H_2$. An outer layer (180 μm thick) confines intermediate degradation debris and isolates the surrounding biological tissues from the acidic environment, during a longer period of resorption. The entire device resorbs over the following 10 days. The use of this technology for a 1 h period of stimulation shortly after implantation promotes axonal regeneration after nerve injuries, as demonstrated in mouse models.

https://doi.org/10.1021/acs.chemrev.3c00408
Chem. Rev. XXXX, XXX, XXX−XXX

In addition to peripheral nervous systems, bioresorbable electrotherapeutic devices can be also exploited for the repair and regeneration of damage to the central nervous system. Figure 26b highlights an electroactive 3D scaffold in the repair and regeneration of spinal cord injury.[77] Preparation of the 3D scaffold begins with electrospinning of a mixture of PLA and PDA coated KNN nanowires. Rolling the resultant PLA/KNN@PDA in a porous, thin film form and separating PLA microstrips prepared by 3D printing together yields a 3D piezoelectric, cylindrical scaffold (2 mm in diameter) as a controllable in situ piezoelectric stimulator. Ultrasound delivered to the scaffold leads to transduction of this mechanical energy (input) to electrical energy (output), enabling on-demand, wirelessly powered stimulation for spinal cord injury. Studies of *in vitro* biodegradation of PLA microstrips and PLA/KNN@PDA show weight losses of ∼64% and 46% for 12 months with immersion in PBS (pH 7.4) at 37 °C, respectively. The application of 20 min excitation of ultrasound (100 kPa) every 2 days for 8 weeks in rat models with spinal cord injury leads to a significant improvement of recovery of musculoskeletal function.

Similarly, electrostimulation can promote healing processes following bone fractures. Recently developed bioresorbable electrical stimulators for bone regeneration uses 3D optoelectronic scaffolds.[299] These scaffolds mainly consist of lithographically patterned, boron-doped mono−Si mesh structures ($\sim 10^{15}$ cm^{-3}; 3 μm thick, 200 × 200 μm^2 in hole size) embedded into a disk-shaped (800 μm thick and 5 mm in diameter), porous collagen/PCL matrix. Responding to near-infrared illumination, the Si mesh generates electrical signals that depolarize cellular potentials and evoke intracellular calcium activity, thereby promoting the regeneration of cranial defects (5 mm in diameter) in rodent models for 8 weeks. Here, the Si mesh consists of micropillars (2−3 μm in height; 2 μm in diameter; 10 μm in pitch) and nanosized pyramids (∼200 nm in height) formed via plasma etching and wet chemical etching in potassium hydroxide solution (2 mg/10 mL at 80 °C). These structures enhance the optical absorption of the Si film, thereby resulting in improved efficiency of photoelectric conversion for electrical stimulation. Furthermore, the embedded Si film contributes to increases in the modulus of the 3D scaffold from 12 to 66 MPa, matching the mechanical properties of natural bone.

Recent advances in electrotherapy may offer additional capabilities in healing of would sites. Here, wound closure can be accelerated by application of an electric field, by restoring the electrical current that occurs when endogenous wounds undergo natural healing. In one case, a bioresorbable stimulator consists of a pair of highly conductive Mo electrodes (15 μm thick) with serpentine layouts for mechanical stability (Figure 26c).[300] An applied direct current voltage of 1.1 V for 30 min day^{-1} heals wound sites with accelerated rates compared to untreated group, ∼86% closure for treated and ∼66% closure for untreated on day 15. As a result, electrostimulation results in complete closure for would site after 18 days. Although this platform includes a nonbioresorbable electronic module that can be removed after healing, a combination with the aforementioned capabilities in bioresorbable powering components suggest possibilities for fully implantable, bioresorbable wound healing systems.

6.2.3. Pain Relief. An attractive example of a therapeutic platform that can be realized using bioresorbable electronics relates to nonpharmacological pain management via conduction block in peripheral nerve systems. Pain signals in the form of action potentials that travel along the peripheral nerves can be blocked locally by use of miniaturized implantable devices. These devices then bioresorb after a period of need to avoid load on the nerve and risk to the patient, without the requirement for an extraction surgery (Figure 27a). Thermal, electrical, optical mechanisms can be relevant in this context, as engineering alternatives to traditional pharmacological approaches such as those related to opioids. Figure 27b highlights a soft, bioresorbable system for reversible nerve conduction block via local cooling.[11] The device consists of microfluidic and electronic components. A bioresorbable elastomer, POC (425 μm thick), forms a microfluidic structure that can deliver bioinert liquid coolant (i.e., perfluoropentane) and dry nitrogen gas (N_2) into serpentine channel structures (250 μm deep) at the location of the nerve. Cooling follows from the phase transition of the liquid coolant to gas triggered by flow of dry N_2. Thin serpentine, Mg traces (25 μm wide, 72 mm long, 300 nm thick) encapsulated with SiO_2 (100 nm thick) on bioresorbable cellulose acetate substrates (50 μm thick) form an electronic layer for temperature sensing at the location of the nerve. This sensor provides feedback for control of the cooling power. Results in live animal models demonstrate possibilities in targeted neural block, with relevance across a range of clinical applications.

Another interface for nerve block involves electrical stimulation. A recent example uses a bioresorbable nerve cuff in a cylindrical geometry to deliver kilohertz frequency alternating current (KHFAC) with an amplitude of 10 V_{pp} and a frequency of 25 kHz as the optimal input.[23] This scheme can wrap circumferentially around the targeted nerve for delivery of the electrical signal, thereby leading to reliable and complete nerve block with response times less than 10 ms. The KHFAC can arrest the action potential (Figure 27c). This cuff includes two different bioresorbable metal electrodes, 15 μm thick Mo electrodes serve as a stimulating interface, and 50 μm thick Mg electrodes serve as an extension interface to external power supply. The high resistance of the Mo electrodes to electrochemical corrosion enables reliable delivery of blocking stimuli (i.e., AC; 10 V_{pp} at 25 kHz) to the targeted nerve during implantation, by comparison to Mg electrodes which corrode rapidly (within an hour) under physiological conditions (i.e., PBS; pH 7.4 at 37 °C) and electrical stimulation. The woven, interleaved interface between these two electrodes provides robust mechanical strength and electrical connection during implantation. A 40 μm thick layer of PLGA (75:25) serves as a supporting substrate for the Mo electrodes to define the overall cuff geometry, selected for its mechanical flexibility. The 200 μm-thick layers of PA encapsulate the entire device as a biofluids barrier, except at the stimulating interface. *In vivo* investigations of reversible nerve conduction block illustrate complete, high efficacy for both sensory and motor block. In particular, recordings in living rat models demonstrate consistent blocking performance for 9 days after implantation, which suggests feasibility of this platform as a bioelectronic medicine for acute pain management.

6.2.4. Pharmacological Systems. Most traditional approaches to therapy and pain medication use pharmacological approaches, typically delivered systemically through oral administration or locally via syringe injection. Concepts in actively or passively controlled release from implantable devices are attractive alternatives for many applications. Passive systems,[131,301,302] such as those based on bioresorbable polymer

https://doi.org/10.1021/acs.chemrev.3c00408
Chem. Rev. XXXX, XXX, XXX−XXX

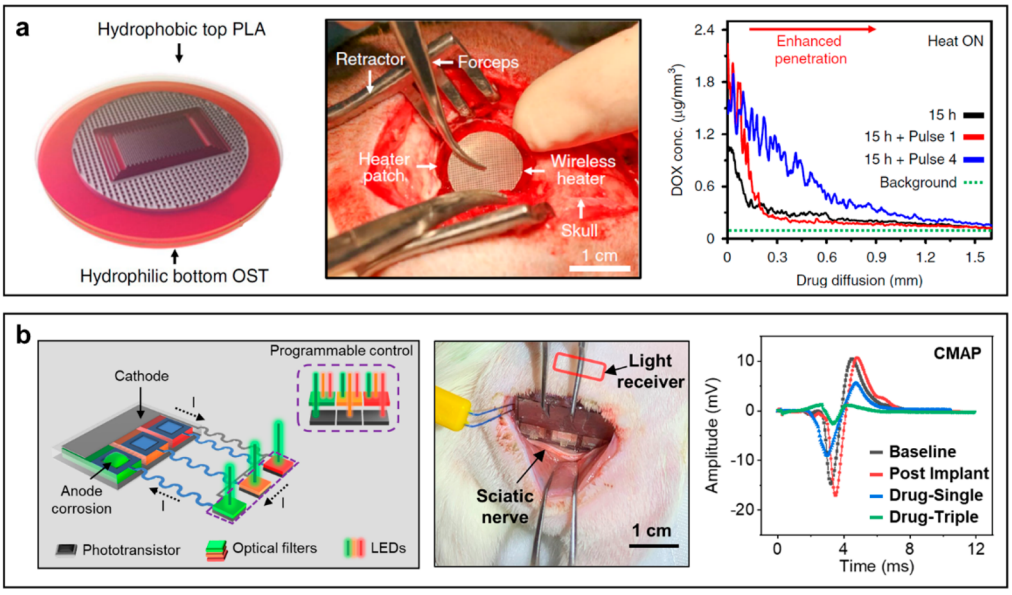

Figure 28. Examples of bioresorbable drug delivery devices. (a) Schematic illustration (left), brain craniotomy implantation (middle), and *in vivo* measurement of the DOX concentration at 15 h after implantation (right) with the pulsed mild-thermic actuation (no pulse: black; one pulse: red; four pulses: blue) of a mild-thermic actuated bioresorbable electronic patch (BEP).[278] Reproduced with permission from ref 278. Copyright 2019 Springer Nature. (b) Schematic illustration (left), implantation adjacent to the sciatic nerve of a rat (middle), and changes in CMAP associated with the programmable release of lidocaine (right) of a self-powered, light-controlled device for programmed drug release.[30] Reproduced with permission from ref 30. Copyright 2023 United States National Academy of Sciences.

matrices and porous scaffolds, allow the gradual release of drugs. Implantable devices can deliver drugs on command but require surgical procedures for extraction and/or refilling. Such devices, when constructed from bioresorbable materials, are appealing because they can naturally resorb in the body after the drug release process. Electromagnetic harvesters,[29,139,161,278,303,304] triboelectric generators,[290] or battery cells[30] can power the release process via thermal[161,278,290,303,304] or electrical[29,30] mechanisms.

Thermal schemes represent simple, robust solutions. An RF-powered bioresorbable device of this sort, based on silk fibroin, allows remotely triggered release of antibiotics for infection management at a surgical or suturing site.[139] The device consists of square-shaped Mg RF coils (5 turns, ∼5 mm side, a resonance frequency of 80 MHz), resistive heating elements constructed from Mg, and a drug-loaded silk film. Increasing the temperature decreases the crystallinity (e.g., beta-sheet content) of silk and thus enhances its bioresorption rate. Inductive coupling to an external transmission antenna supplies power to cause Joule heating in the resistors, thereby initiating release of drugs embedded into the silk. Operating a transmission coil at 80 MHz with a power of 500 mW yields a temperature increase at the heating element of ∼20 °C.[139] A lipid-based device provides an alternative to the silk for multiple release events of doxorubicin (DOX) from multiple independently controlled drug reservoirs by using multiple receiver coils with different resonance frequencies for frequency-selective power harvesting,[161] as described in section 4. Advanced examples include flexible and sticky electronic patches for intracranial drug delivery to brain tumors.[278] Here, a hydrophilic/hydrophobic bifacial design (Figure 28a, left) enables conformal adhesion to the brain tissue and targeted drug delivery with minimized release to cerebrospinal fluid. An oxidized starch (OST) patch contains an Mg bioresorbable heater, an Mg temperature sensor, a PLA encapsulation layer, and DOX loaded on the patch.[278] Applying an alternating RF magnetic field wirelessly triggers Joule heating and increases the temperature of the BEP and surrounding tissues by 5 °C, which thus enables drug release from the reservoir and accelerates intercellular drug diffusion. Figure 28a (middle) shows the implantation of a BEP during a brain craniotomy in a canine model. The higher DOX concentration after BEP implantation and pulsed mild-thermic actuation (Figure 28a, right) validates the operation.[278]

Electrically triggered release is possible by electrochemical corrosion of metal gates above sealed drug reservoirs, as a fast and energy-efficient alternative to thermal mechanisms. A wirelessly controlled drug delivery system of this type utilizes metal anode corrosion phenomenon to achieve passive drug release.[29] The device contains three RF power-harvesting disk-shaped coils (Mg, diameters of 12 mm, resonance frequencies of 5.14, 9.92, and 14.78 MHz, with 16, 13, and 8 turns, respectively), three electrochemically bioresorbable Mg metal gate valves and corresponding drug reservoirs made of PA. Delivery of RF power from transmission coils accelerates the corrosion and dissolution of the metal gate when immersed in biofluids, thus enabling diffusive drug release from the underlying reservoir. The corrosion reaction of the Mg gate is $Mg - 2e^- + 2H_2O \rightarrow Mg(OH)_2 + 2H^+$.[29] In a self-powered alternative (Figure 28b, left),[30] the metal gates (Mg foils) serve as anodes for a battery structure via electrical connections to a common cathode (a Fe or Mo foil) through a corresponding collection of phototransistors. Surrounding biofluids serve as electrolyte. Illuminating the phototransistor decreases its electrical resistance and short circuits the battery cell formed by the anode and cathode, thereby leading to fast dissolution of the gate and opening of the reservoir.[30] The gate corrosion and cathode reactions are $Mg - 2e^- + 2H_2O \rightarrow Mg(OH)_2 + 2H^+$ and $2H^+ + 2e^- \rightarrow H_2$, respectively. Optical filters with wavelength-selective responses placed atop the phototransistors enable programmability through a wavelength-division multi-

https://doi.org/10.1021/acs.chemrev.3c00408
Chem. Rev. XXXX, XXX, XXX−XXX

plexing strategy.[30] Such a design allows for compact designs, scalable to far more reservoirs and independently controlled release events compared to the RF powered analogue described above. *In vivo*, programmed lidocaine release for pain management adjacent rat sciatic nerves illustrates the functionality and programmability (Figure 28b, middle). Compound muscle action potentials (CMAPs) and sensory nerve action potentials (SNAPs) decrease after drug release, consistent with expected blocking of pain signals (Figure 28b, right).[30]

7. CONCLUSIONS AND PERSPECTIVES

This review highlights recent advances in bioresorbable electronics, with a focus on the essential materials and their underlying chemistries. The content includes examples of components, sensors and power supplies formed with these materials, using specialized fabrication and assembly techniques. A summary of integrated systems with diagnostic or therapeutic functions that address clinical needs highlights the current maturity of this field of research.

Progress in the chemistry of bioresorbable electronic materials will continue to serve as the basis for advances in this technology. An area of opportunity for further research is in chemical methods that enable precise control over the mechanisms and rates of bioresorption. For example, current materials enable applications that require operation over periods of days or several weeks; those that demand chronic stability are not possible. To address this limitation, improved materials that function as efficient barriers to biofluid penetration and that resorb via processes of surface erosion are needed. In addition to the encapsulation materials, methods that can bond biofluid barrier materials and tightly seal the bioresorbable electronics are necessary. Robust conductive composites that interconnect different electronic components in the integration process are also critical. Also, in many systems, the time scales for complete bioresorption are much longer than those associated with operational stability, as described in section 2. To minimize this difference, chemistries that support accelerated rates of bioresorption upon the introduction of an external stimulus are of interest. Previous reports on triggered transience of environmental electronics through thermal[305,306] or electric[307,308] effects may suggest strategies for activated mechanisms in bioresorption based on materials[309−311] that are responsive to chemical, thermal, electric, optical, or mechanical stimuli. An important goal is in independent, programmable control of both operational lifetimes and time scales for complete bioresorption. The long-term influences of bioresorbable devices and their degradation products on biological environment are yet to be understood. Currently, most assessments of bioresorbable electronics are performed *in vitro* in simulated body fluids and *in vivo* in small animal models. It is necessary to study the degradation behaviors and biological influences of these devices *in vivo* in large animal models.

Other opportunities are in chemistries and device designs that enhance patient experiences and outcomes. For example, highly miniaturized devices may facilitate minimally invasive surgeries for implantation. A recent report in this direction involves advanced, small-scale bioresorbable battery technologies that avoid bulky antennas needed for wireless power transfer.[29,30] Bioresorbable power supplies with high energy and power densities will facilitate further miniaturization of various devices. As described in section 4, each type of power supply (batteries, supercapacitors, and mechanical, radio frequency, and photovoltaic energy harvesters, etc.) has its own advantages and disadvantages. A hybrid power system that integrates one or multiple components for both energy storage and harvesting might be an appropriate approach. Similarly, bioresorbable components that enable wireless, external methods for controlling these implanted devices are important. Mechanisms that enable operation into the depths of tissue include light illumination, ultrasound exposure, magnetic coupling, and RF radiation. In one demonstrated case, pairing a bioresorbable RF-powered cardiac pacemaker with a skin-interfaced wireless device for ECG monitoring and for RF power transfer enables closed-loop operation for rate-adaptive and autonomous pacing.[25] Such combinations of therapeutic bioresorbable devices and diagnostic sensors offer powerful options in treating patient conditions. An attractive route to related capabilities might rely on responsive chemical/biochemical principles, to reduce or eliminate the need for electronics. Recent advances in bioresorbable stimuli-responsive materials[310,311] and chemical sensors[147] may suggest routes in this direction. Additional chemistries must be developed to realize fully resorbable versions of such sensors.[71,195] In addition to bioresorbable electronics that safely resorb in the human body, biodegradable electronic skins[312,313] that can harmlessly degrade in the environment alleviate the environmental burdens and health risks caused by solid electronic waste streams. Although outside of the scope of this review, these interesting devices provide diagnostic and therapeutic functions such as tactile sensing,[314] pressure sensing,[315] physiological signal monitoring,[316] and transdermal drug delivery.[317]

Translating bioresorbable medical devices from academic demonstrations and prototypes into platforms for routine human use will require regulatory review of these fundamentally new classes of technologies. The aspects of interest span not only those of traditional bioresorbable implants (e.g., stents, scaffolds), primarily their mechanical and chemical properties, but also various electrical, magnetic, electromagnetic, and optical characteristics commonly associated with conventional nonresorbable implants. This expanded set of considerations will require heightened regulatory review but balanced by reduced levels of risk due to the intrinsically transient nature of the devices. The diverse range of interesting research directions in these and other contexts, taken together with the potential for transformative improvements in patient care, serve as strong motivations for expanded research in this emerging field of chemistry.

AUTHOR INFORMATION

Corresponding Author

John A. Rogers − *Center for Bio-Integrated Electronics, Northwestern University, Evanston, Illinois 60208, United States; Querrey Simpson Institute for Bioelectronics, Department of Materials Science and Engineering, and Department of Mechanical Engineering, Biomedical Engineering, Chemistry, Electrical Engineering and Computer Science, Northwestern University, Evanston, Illinois 60208, United States; Department of Neurological Surgery, Feinberg School of Medicine, Northwestern University, Chicago, Illinois 60611, United States;* orcid.org/0000-0002-2980-3961; Email: jrogers@northwestern.edu

Authors

Yamin Zhang − *Center for Bio-Integrated Electronics, Northwestern University, Evanston, Illinois 60208, United States; Querrey Simpson Institute for Bioelectronics,*

https://doi.org/10.1021/acs.chemrev.3c00408
Chem. Rev. XXXX, XXX, XXX−XXX

Northwestern University, Evanston, Illinois 60208, United States; orcid.org/0000-0003-4890-1265

Geumbee Lee − *Center for Bio-Integrated Electronics, Northwestern University, Evanston, Illinois 60208, United States; Querrey Simpson Institute for Bioelectronics, Northwestern University, Evanston, Illinois 60208, United States*

Shuo Li − *Center for Bio-Integrated Electronics, Northwestern University, Evanston, Illinois 60208, United States; Querrey Simpson Institute for Bioelectronics, Northwestern University, Evanston, Illinois 60208, United States*

Ziying Hu − *Center for Bio-Integrated Electronics, Northwestern University, Evanston, Illinois 60208, United States; Querrey Simpson Institute for Bioelectronics, Northwestern University, Evanston, Illinois 60208, United States*

Kaiyu Zhao − *Department of Materials Science and Engineering, Northwestern University, Evanston, Illinois 60208, United States*

Complete contact information is available at: https://pubs.acs.org/10.1021/acs.chemrev.3c00408

Author Contributions

#Y.Z., G.L., S.L., and Z.H. contributed equally. CRediT: **Yamin Zhang** conceptualization, writing-original draft, writing-review & editing; **Geumbee Lee** conceptualization, writing-original draft, writing-review & editing; **Shuo Li** conceptualization, writing-original draft, writing-review & editing; **Ziying Hu** conceptualization, writing-original draft, writing-review & editing; **Kaiyu Zhao** writing-original draft; **John A. Rogers** conceptualization, funding acquisition, project administration, supervision, writing-original draft, writing-review & editing.

Notes

The authors declare no competing financial interest.

Biographies

Yamin Zhang received her Ph.D. degree in Chemical Engineering in 2020 from Georgia Institute of Technology. In 2016, she received a B.S. in Chemical Engineering and Technology from Tianjin University and a B.S. in Finance from Nankai University. She is currently a Postdoctoral Fellow at the Querrey Simpson Institute for Bioelectronics at Northwestern University. Her research interests include bioresorbable materials and electronics, electrochemistry, and battery technology.

Geumbee Lee received her B.S. degree in Chemistry from Duksung Women's University in 2012, and her Ph.D. in Nano-Bio-Information-Technology from Korea University in 2019. She is currently a postdoctoral research fellow within the Querrey Simpson Institute for Bioelectronics at Northwestern University. Her research interests include the development of materials, devices, fabrication techniques for energy storage systems in wearable electronics, as well as the advancement of transient bioelectronics based on eco/bioresorbable materials.

Shuo Li obtained B.S. degree in Materials Science and Engineering from University of Illinois Urbana−Champaign in 2014. He received M.S. and Ph.D. degrees from Cornell University in 2016 and 2020, respectively, both in Materials Science. He was a Postdoctoral Fellow of the Querrey Simpson Institute of Bioelectronics at Northwestern University from 2020 to 2023. He is now a Research Scientist at ETH Zurich.

Ziying Hu obtained B.S. degree in Materials Science and Engineering from Wuhan University of Science and Technology in 2011 and M.S. degree in Applied Chemistry from Beihang University in 2014. From University of California, San Diego, she received her M.S. degree in Materials Science and Engineering in 2016. In 2020, she obtained her Ph.D. degree in Chemistry from Northwestern University and joined the Rogers Research Group as a postdoctoral scholar. Her research interests include bioresorbable materials and electronics, manufacturing technologies, soft matter, biomaterials, and bioinspired interfacial materials with special wettability.

Kaiyu Zhao received his B.S. degree from Jilin University in 2022. He is now pursuing his master's degree in the Department of Materials Science and Engineering at Northwestern University. His current research interests include the synthesis of bioresorbable polymers and the design of transient devices.

John A. Rogers obtained B.A. and B.S. degrees in chemistry and in physics from the University of Texas-Austin, in 1989. From MIT, he received S.M. degrees in physics and in chemistry in 1992 and his Ph.D. degree in physical chemistry in 1995. From 1995 to 1997, Rogers was a Junior Fellow in the Harvard University Society of Fellows. He joined Bell Laboratories as a member of technical staff in the Condensed Matter Physics Research Department in 1997 and served as director of this department from the end of 2000 to 2002. He then spent 13 years on the faculty at University of Illinois, most recently as the Swanlund Chair Professor and Director of the Seitz Materials Research Laboratory. In 2016, he joined Northwestern University as the Louis Simpson and Kimberly Querrey Professor of Materials Science and Engineering, Biomedical Engineering, and Medicine, with affiliate appointments in Mechanical Engineering, Electrical and Computer Engineering, and Chemistry, where he is also Director of the Querrey Simpson Institute for Bioelectronics.

ACKNOWLEDGMENTS

This work was supported by the Querrey Simpson Institute for Bioelectronics at Northwestern University. Y.Z. thanks Jihye Kim for discussions on triboelectric nanogenerators. We thank Xinyue Lu and Jin Wang for assistance with modifications of figures and references. We gratefully acknowledge Jung Gil Kook and Eun Bi Lee for their efforts on artwork in Figure 22.

REFERENCES

(1) Ryu, H.; Seo, M.; Rogers, J. A. Bioresorbable Metals for Biomedical Applications: From Mechanical Components to Electronic Devices. *Adv. Healthc Mater.* **2021**, *10*, 2002236.

(2) Kang, S.-K.; Koo, J.; Lee, Y. K.; Rogers, J. A. Advanced Materials and Devices for Bioresorbable Electronics. *Acc. Chem. Res.* **2018**, *51*, 988−998.

(3) Shim, J.-S.; Rogers, J. A.; Kang, S.-K. Physically Transient Electronic Materials and Devices. *Materials Science and Engineering: R: Reports* **2021**, *145*, 100624.

(4) Gao, Y.; Zhang, Y.; Wang, X.; Sim, K.; Liu, J.; Chen, J.; Feng, X.; Xu, H.; Yu, C. Moisture-Triggered Physically Transient Electronics. *Sci. Adv.* **2017**, *3*, e1701222.

(5) Yang, Q.; Liu, T.-L.; Xue, Y.; Wang, H.; Xu, Y.; Emon, B.; Wu, M.; Rountree, C.; Wei, T.; Kandela, I.; et al. Ecoresorbable and Bioresorbable Microelectromechanical Systems. *Nat. Electron* **2022**, *5*, 526−538.

(6) Singh, R.; Bathaei, M. J.; Istif, E.; Beker, L. A Review of Bioresorbable Implantable Medical Devices: Materials, Fabrication, and Implementation. *Adv. Healthc Mater.* **2020**, *9*, 2000790.

(7) Chatterjee, S.; Saxena, M.; Padmanabhan, D.; Jayachandra, M.; Pandya, H. J. Futuristic Medical Implants Using Bioresorbable Materials and Devices. *Biosens Bioelectron* **2019**, *142*, 111489.

(8) Hwang, S.-W.; Kim, D.-H.; Tao, H.; Kim, T.; Kim, S.; Yu, K. J.; Panilaitis, B.; Jeong, J.-W.; Song, J.-K.; Omenetto, F. G.; et al. Materials

and Fabrication Processes for Transient and Bioresorbable High-Performance Electronics. *Adv. Funct Mater.* **2013**, *23*, 4087−4093.
(9) Kang, S.-K.; Murphy, R. K. J.; Hwang, S.-W.; Lee, S. M.; Harburg, D. V.; Krueger, N. A.; Shin, J.; Gamble, P.; Cheng, H.; Yu, S.; et al. Bioresorbable Silicon Electronic Sensors for the Brain. *Nature* **2016**, *530*, 71−76.
(10) Kim, D.-H.; Kim, Y.-S.; Amsden, J.; Panilaitis, B.; Kaplan, D. L.; Omenetto, F. G.; Zakin, M. R.; Rogers, J. A. Silicon Electronics on Silk as a Path to Bioresorbable, Implantable Devices. *Appl. Phys. Lett.* **2009**, *95*, 133701.
(11) Reeder, J. T.; Xie, Z.; Yang, Q.; Seo, M.-H.; Yan, Y.; Deng, Y.; Jinkins, K. R.; Krishnan, S. R.; Liu, C.; McKay, S.; et al. Soft, Bioresorbable Coolers for Reversible Conduction Block of Peripheral Nerves. *Science* **2022**, *377*, 109−115.
(12) Visscher, L. E.; Jeffery, C.; Gilmour, T.; Anderson, L.; Couzens, G. The History of Suture Anchors in Orthopaedic Surgery. *Clinical Biomechanics* **2019**, *61*, 70−78.
(13) Ang, H. Y.; Bulluck, H.; Wong, P.; Venkatraman, S. S.; Huang, Y.; Foin, N. Bioresorbable Stents: Current and Upcoming Bioresorbable Technologies. *Int. J. Cardiol* **2017**, *228*, 931−939.
(14) Witte, F.; Reifenrath, J.; Müller, P. P.; Crostack, H.-A.; Nellesen, J.; Bach, F. W.; Bormann, D.; Rudert, M. Cartilage Repair on Magnesium Scaffolds Used as a Subchondral Bone Replacement. *Materwiss Werksttech* **2006**, *37*, 504−508.
(15) Macdonald, M. L.; Samuel, R. E.; Shah, N. J.; Padera, R. F.; Beben, Y. M.; Hammond, P. T. Tissue Integration of Growth Factor-Eluting Layer-by-Layer Polyelectrolyte Multilayer Coated Implants. *Biomaterials* **2011**, *32*, 1446−1453.
(16) Lee, G.; Kang, S.-K.; Won, S. M.; Gutruf, P.; Jeong, Y. R.; Koo, J.; Lee, S.-S.; Rogers, J. A.; Ha, J. S. Fully Biodegradable Micro-supercapacitor for Power Storage in Transient Electronics. *Adv. Energy Mater.* **2017**, *7*, 1700157.
(17) Lu, D.; Liu, T.; Chang, J.; Peng, D.; Zhang, Y.; Shin, J.; Hang, T.; Bai, W.; Yang, Q.; Rogers, J. A. Transient Light-Emitting Diodes Constructed from Semiconductors and Transparent Conductors That Biodegrade Under Physiological Conditions. *Adv. Mater.* **2019**, *31*, 1902739.
(18) Kang, S.-K.; Park, G.; Kim, K.; Hwang, S.-W.; Cheng, H.; Shin, J.; Chung, S.; Kim, M.; Yin, L.; Lee, J. C.; et al. Dissolution Chemistry and Biocompatibility of Silicon- and Germanium-Based Semiconductors for Transient Electronics. *ACS Appl. Mater. Interfaces* **2015**, *7*, 9297−9305.
(19) Zhao, H.; Xue, Z.; Wu, X.; Wei, Z.; Guo, Q.; Xu, M.; Qu, C.; You, C.; Mei, Y.; Zhang, M.; et al. Biodegradable Germanium Electronics for Integrated Biosensing of Physiological Signals. *npj Flexible Electronics* **2022**, *6*, 63.
(20) Lee, Y. K.; Yu, K. J.; Song, E.; Barati Farimani, A.; Vitale, F.; Xie, Z.; Yoon, Y.; Kim, Y.; Richardson, A.; Luan, H.; et al. Dissolution of Monocrystalline Silicon Nanomembranes and Their Use as Encapsulation Layers and Electrical Interfaces in Water-Soluble Electronics. *ACS Nano* **2017**, *11*, 12562−12572.
(21) Yang, Q.; Lee, S.; Xue, Y.; Yan, Y.; Liu, T.; Kang, S.; Lee, Y. J.; Lee, S. H.; Seo, M.; Lu, D.; et al. Materials, Mechanics Designs, and Bioresorbable Multisensor Platforms for Pressure Monitoring in the Intracranial Space. *Adv. Funct Mater.* **2020**, *30*, 1910718.
(22) Choi, Y. S.; Yin, R. T.; Pfenniger, A.; Koo, J.; Avila, R.; Benjamin Lee, K.; Chen, S. W.; Lee, G.; Li, G.; Qiao, Y.; et al. Fully Implantable and Bioresorbable Cardiac Pacemakers without Leads or Batteries. *Nat. Biotechnol.* **2021**, *39*, 1228−1238.
(23) Lee, G.; Ray, E.; Yoon, H.-J.; Genovese, S.; Choi, Y. S.; Lee, M.-K.; Şahin, S.; Yan, Y.; Ahn, H.-Y.; Bandodkar, A. J. A Bioresorbable Peripheral Nerve Stimulator for Electronic Pain Block. *Sci. Adv.* **2022**, *8*, eabp9169.
(24) Koo, J.; MacEwan, M. R.; Kang, S.-K.; Won, S. M.; Stephen, M.; Gamble, P.; Xie, Z.; Yan, Y.; Chen, Y.-Y.; Shin, J.; et al. Wireless Bioresorbable Electronic System Enables Sustained Nonpharmacological Neuroregenerative Therapy. *Nat. Med.* **2018**, *24*, 1830−1836.
(25) Choi, Y. S.; Jeong, H.; Yin, R. T.; Avila, R.; Pfenniger, A.; Yoo, J.; Lee, J. Y.; Tzavelis, A.; Lee, Y. J.; Chen, S. W.; et al. A Transient, Closed-Loop Network of Wireless, Body-Integrated Devices for Autonomous Electrotherapy. *Science* **2022**, *376*, 1006−1012.
(26) Boutry, C. M.; Beker, L.; Kaizawa, Y.; Vassos, C.; Tran, H.; Hinckley, A. C.; Pfattner, R.; Niu, S.; Li, J.; Claverie, J.; et al. Biodegradable and Flexible Arterial-Pulse Sensor for the Wireless Monitoring of Blood Flow. *Nat. Biomed Eng.* **2019**, *3*, 47−57.
(27) Liu, Z.; Wen, B.; Cao, L.; Zhang, S.; Lei, Y.; Zhao, G.; Chen, L.; Wang, J.; Shi, Y.; Xu, J.; et al. Photoelectric Cardiac Pacing by Flexible and Degradable Amorphous Si Radial Junction Stimulators. *Adv. Healthc Mater.* **2020**, *9*, 1901342.
(28) Wang, L.; Lu, C.; Yang, S.; Sun, P.; Wang, Y.; Guan, Y.; Liu, S.; Cheng, D.; Meng, H.; Wang, Q. A Fully Biodegradable and Self-Electrified Device for Neuroregenerative Medicine. *Sci. Adv.* **2020**, *6*, eabc6686.
(29) Koo, J.; Kim, S. B.; Choi, Y. S.; Xie, Z.; Bandodkar, A. J.; Khalifeh, J.; Yan, Y.; Kim, H.; Pezhouh, M. K.; Doty, K. Wirelessly Controlled, Bioresorbable Drug Delivery Device with Active Valves That Exploit Electrochemically Triggered Crevice Corrosion. *Sci. Adv.* **2020**, *6*, eabb1093.
(30) Zhang, Y.; Liu, F.; Zhang, Y.; Wang, J.; D'Andrea, D.; Walters, J. B.; Li, S.; Yoon, H.-J.; Wu, M.; Li, S. Self-Powered, Light-Controlled, Bioresorbable Platforms for Programmed Drug Delivery. *Proc. Natl. Acad. Sci. U. S. A.* **2023**, *120*, e2217734120.
(31) Han, H.-S.; Loffredo, S.; Jun, I.; Edwards, J.; Kim, Y.-C.; Seok, H.-K.; Witte, F.; Mantovani, D.; Glyn-Jones, S. Current Status and Outlook on the Clinical Translation of Biodegradable Metals. *Mater. Today* **2019**, *23*, 57−71.
(32) Li, C.; Guo, C.; Fitzpatrick, V.; Ibrahim, A.; Zwierstra, M. J.; Hanna, P.; Lechtig, A.; Nazarian, A.; Lin, S. J.; Kaplan, D. L. Design of Biodegradable, Implantable Devices towards Clinical Translation. *Nat. Rev. Mater.* **2020**, *5*, 61−81.
(33) Zheng, Y. F.; Gu, X. N.; Witte, F. Biodegradable Metals. *Materials Science and Engineering: R: Reports* **2014**, *77*, 1−34.
(34) Yin, L.; Cheng, H.; Mao, S.; Haasch, R.; Liu, Y.; Xie, X.; Hwang, S.; Jain, H.; Kang, S.; Su, Y.; et al. Dissolvable Metals for Transient Electronics. *Adv. Funct Mater.* **2014**, *24*, 645−658.
(35) Son, D.; Lee, J.; Lee, D. J.; Ghaffari, R.; Yun, S.; Kim, S. J.; Lee, J. E.; Cho, H. R.; Yoon, S.; Yang, S.; et al. Bioresorbable Electronic Stent Integrated with Therapeutic Nanoparticles for Endovascular Diseases. *ACS Nano* **2015**, *9*, 5937−5946.
(36) Bai, W.; Shin, J.; Fu, R.; Kandela, I.; Lu, D.; Ni, X.; Park, Y.; Liu, Z.; Hang, T.; Wu, D.; et al. Bioresorbable Photonic Devices for the Spectroscopic Characterization of Physiological Status and Neural Activity. *Nat. Biomed Eng.* **2019**, *3*, 644−654.
(37) Choi, Y.; Koo, J.; Rogers, J. A. Inorganic Materials for Transient Electronics in Biomedical Applications. *MRS Bull.* **2020**, *45*, 103−112.
(38) Kang, S.-K.; Hwang, S.-W.; Yu, S.; Seo, J.-H.; Corbin, E. A.; Shin, J.; Wie, D. S.; Bashir, R.; Ma, Z.; Rogers, J. A. Biodegradable Thin Metal Foils and Spin-On Glass Materials for Transient Electronics. *Adv. Funct Mater.* **2015**, *25*, 1789−1797.
(39) Tsakiris, V.; Tardei, C.; Clicinschi, F. M. Biodegradable Mg Alloys for Orthopedic Implants - A Review. *Journal of Magnesium and Alloys* **2021**, *9*, 1884−1905.
(40) Lee, J.-W.; Han, H.-S.; Han, K.-J.; Park, J.; Jeon, H.; Ok, M.-R.; Seok, H.-K.; Ahn, J.-P.; Lee, K. E.; Lee, D.-H.; et al. Long-Term Clinical Study and Multiscale Analysis of in Vivo Biodegradation Mechanism of Mg Alloy. *Proc. Natl. Acad. Sci. U. S. A.* **2016**, *113*, 716−721.
(41) Huang, X.; Liu, Y.; Hwang, S.-W.; Kang, S.-K.; Patnaik, D.; Cortes, J. F.; Rogers, J. A. Biodegradable Materials for Multilayer Transient Printed Circuit Boards. *Adv. Mater.* **2014**, *26*, 7371−7377.
(42) Zhang, T.; Tsang, M.; Du, L.; Kim, M.; Allen, M. G. Electrical Interconnects Fabricated From Biodegradable Conductive Polymer Composites. *IEEE Trans Compon Packaging Manuf Technol.* **2019**, *9*, 822−829.
(43) Ferrandez-Montero, A.; Lieblich, M.; Benavente, R.; González-Carrasco, J. L.; Ferrari, B. New Approach to Improve Polymer-Mg Interface in Biodegradable PLA/Mg Composites through Particle Surface Modification. *Surf. Coat. Technol.* **2020**, *383*, 125285.

https://doi.org/10.1021/acs.chemrev.3c00408
Chem. Rev. XXXX, XXX, XXX−XXX

(44) Lee, S.; Koo, J.; Kang, S.-K.; Park, G.; Lee, Y. J.; Chen, Y.-Y.; Lim, S. A.; Lee, K.-M.; Rogers, J. A. Metal Microparticle - Polymer Composites as Printable, Bio/Ecoresorbable Conductive Inks. *Mater. Today* **2018**, *21*, 207−215.
(45) Kim, K. S.; Maeng, W.-Y.; Kim, S.; Lee, G.; Hong, M.; Kim, G.; Kim, J.; Kim, S.; Han, S.; Yoo, J.; et al. Isotropic Conductive Paste for Bioresorbable Electronics. *Mater. Today Bio* **2023**, *18*, 100541.
(46) Won, S. M.; Koo, J.; Crawford, K. E.; Mickle, A. D.; Xue, Y.; Min, S.; McIlvried, L. A.; Yan, Y.; Kim, S. B.; Lee, S. M.; et al. Natural Wax for Transient Electronics. *Adv. Funct Mater.* **2018**, *28*, 1801819.
(47) Feng, S.; Tian, Z.; Wang, J.; Cao, S.; Kong, D. Laser Sintering of Zn Microparticles and Its Application in Printable Biodegradable Electronics. *Adv. Electron Mater.* **2019**, *5*, 1800693.
(48) Feng, S.; Cao, S.; Tian, Z.; Zhu, H.; Kong, D. Maskless Patterning of Biodegradable Conductors by Selective Laser Sintering of Microparticle Inks and Its Application in Flexible Transient Electronics. *ACS Appl. Mater. Interfaces* **2019**, *11*, 45844−45852.
(49) Mahajan, B. K.; Yu, X.; Shou, W.; Pan, H.; Huang, X. Mechanically Milled Irregular Zinc Nanoparticles for Printable Bioresorbable Electronics. *Small* **2017**, *13*, 1700065.
(50) Lee, Y. K.; Kim, J.; Kim, Y.; Kwak, J. W.; Yoon, Y.; Rogers, J. A. Room Temperature Electrochemical Sintering of Zn Microparticles and Its Use in Printable Conducting Inks for Bioresorbable Electronics. *Adv. Mater.* **2017**, *29*, 1702665.
(51) Pang, A. L.; Arsad, A.; Ahmadipour, M. Synthesis and Factor Affecting on the Conductivity of Polypyrrole: A Short Review. *Polym. Adv. Technol.* **2021**, *32*, 1428−1454.
(52) Bednarczyk, K.; Matysiak, W.; Tański, T.; Janeczek, H.; Schab-Balcerzak, E.; Libera, M. Effect of Polyaniline Content and Protonating Dopants on Electroconductive Composites. *Sci. Rep* **2021**, *11*, 7487.
(53) Machado, J. M.; Karasz, F. E.; Lenz, R. W. Electrically Conducting Polymer Blends. *Polymer (Guildf)* **1988**, *29*, 1412−1417.
(54) Shi, G.; Rouabhia, M.; Wang, Z.; Dao, L. H.; Zhang, Z. A Novel Electrically Conductive and Biodegradable Composite Made of Polypyrrole Nanoparticles and Polylactide. *Biomaterials* **2004**, *25*, 2477−2488.
(55) Lee, J. Y.; Bashur, C. A.; Goldstein, A. S.; Schmidt, C. E. Polypyrrole-Coated Electrospun PLGA Nanofibers for Neural Tissue Applications. *Biomaterials* **2009**, *30*, 4325−4335.
(56) Zhou, J.; Wang, Y.; Cheng, L.; Wu, Z.; Sun, X.; Peng, J. Preparation of Polypyrrole-Embedded Electrospun Poly(Lactic Acid) Nanofibrous Scaffolds for Nerve Tissue Engineering. *Neural Regen Res.* **2016**, *11*, 1644.
(57) Jia, X.; Wang, C.; Zhao, C.; Ge, Y.; Wallace, G. G. Toward Biodegradable Mg-Air Bioelectric Batteries Composed of Silk Fibroin-Polypyrrole Film. *Adv. Funct Mater.* **2016**, *26*, 1454−1462.
(58) Wang, S.; Guan, S.; Wang, J.; Liu, H.; Liu, T.; Ma, X.; Cui, Z. Fabrication and Characterization of Conductive Poly (3,4-Ethylenedioxythiophene) Doped with Hyaluronic Acid/Poly (l-Lactic Acid) Composite Film for Biomedical Application. *J. Biosci Bioeng* **2017**, *123*, 116−125.
(59) Feng, Z.-Q.; Wu, J.; Cho, W.; Leach, M. K.; Franz, E. W.; Naim, Y. I.; Gu, Z.-Z.; Corey, J. M.; Martin, D. C. Highly Aligned Poly(3,4-Ethylene Dioxythiophene) (PEDOT) Nano- and Microscale Fibers and Tubes. *Polymer (Guildf)* **2013**, *54*, 702−708.
(60) LI, M.; GUO, Y.; WEI, Y.; MACDIARMID, A.; LELKES, P. Electrospinning Polyaniline-Contained Gelatin Nanofibers for Tissue Engineering Applications. *Biomaterials* **2006**, *27*, 2705−2715.
(61) Jeong, S. I.; Jun, I. D.; Choi, M. J.; Nho, Y. C.; Lee, Y. M.; Shin, H. Development of Electroactive and Elastic Nanofibers That Contain Polyaniline and Poly(L-Lactide-Co-ε-Caprolactone) for the Control of Cell Adhesion. *Macromol. Biosci* **2008**, *8*, 627−637.
(62) Zelikin, A. N.; Lynn, D. M.; Farhadi, J.; Martin, I.; Shastri, V.; Langer, R. Erodible Conducting Polymers for Potential Biomedical Applications. *Angew. Chem., Int. Ed.* **2002**, *41*, 141−144.
(63) Mawad, D.; Gilmore, K.; Molino, P.; Wagner, K.; Wagner, P.; Officer, D. L.; Wallace, G. G. An Erodible Polythiophene-Based Composite for Biomedical Applications. *J. Mater. Chem.* **2011**, *21*, 5555.
(64) Guo, B.; Finne-Wistrand, A.; Albertsson, A.-C. Facile Synthesis of Degradable and Electrically Conductive Polysaccharide Hydrogels. *Biomacromolecules* **2011**, *12*, 2601−2609.
(65) Xie, M.; Wang, L.; Ge, J.; Guo, B.; Ma, P. X. Strong Electroactive Biodegradable Shape Memory Polymer Networks Based on Star-Shaped Polylactide and Aniline Trimer for Bone Tissue Engineering. *ACS Appl. Mater. Interfaces* **2015**, *7*, 6772−6781.
(66) Chen, J.; Dong, R.; Ge, J.; Guo, B.; Ma, P. X. Biocompatible, Biodegradable, and Electroactive Polyurethane-Urea Elastomers with Tunable Hydrophilicity for Skeletal Muscle Tissue Engineering. *ACS Appl. Mater. Interfaces* **2015**, *7*, 28273−28285.
(67) Guo, B.; Finne-Wistrand, A.; Albertsson, A.-C. Enhanced Electrical Conductivity by Macromolecular Architecture: Hyperbranched Electroactive and Degradable Block Copolymers Based on Poly(ε-Caprolactone) and Aniline Pentamer. *Macromolecules* **2010**, *43*, 4472−4480.
(68) Xie, M.; Wang, L.; Guo, B.; Wang, Z.; Chen, Y. E.; Ma, P. X. Ductile Electroactive Biodegradable Hyperbranched Polylactide Copolymers Enhancing Myoblast Differentiation. *Biomaterials* **2015**, *71*, 158−167.
(69) Zhang, Q.; Yan, Y.; Li, S.; Feng, T. The Synthesis and Characterization of a Novel Biodegradable and Electroactive Polyphosphazene for Nerve Regeneration. *Materials Science and Engineering: C* **2010**, *30*, 160−166.
(70) Xu, C.; Huang, Y.; Yepez, G.; Wei, Z.; Liu, F.; Bugarin, A.; Tang, L.; Hong, Y. Development of Dopant-Free Conductive Bioelastomers. *Sci. Rep* **2016**, *6*, 34451.
(71) Pal, R. K.; Farghaly, A. A.; Wang, C.; Collinson, M. M.; Kundu, S. C.; Yadavalli, V. K. Conducting Polymer-Silk Biocomposites for Flexible and Biodegradable Electrochemical Sensors. *Biosens Bioelectron* **2016**, *81*, 294−302.
(72) Li, L.; Ge, J.; Guo, B.; Ma, P. X. In Situ Forming Biodegradable Electroactive Hydrogels. *Polym. Chem.* **2014**, *5*, 2880−2890.
(73) Bettinger, C. J.; Bruggeman, J. P.; Misra, A.; Borenstein, J. T.; Langer, R. Biocompatibility of Biodegradable Semiconducting Melanin Films for Nerve Tissue Engineering. *Biomaterials* **2009**, *30*, 3050−3057.
(74) Lei, T.; Guan, M.; Liu, J.; Lin, H.-C.; Pfattner, R.; Shaw, L.; McGuire, A. F.; Huang, T.-C.; Shao, L.; Cheng, K.-T.; et al. Biocompatible and Totally Disintegrable Semiconducting Polymer for Ultrathin and Ultralightweight Transient Electronics. *Proc. Natl. Acad. Sci. U. S. A.* **2017**, *114*, 5107−5112.
(75) Bettinger, C. J.; Bao, Z. Organic Thin-Film Transistors Fabricated on Resorbable Biomaterial Substrates. *Adv. Mater.* **2010**, *22*, 651−655.
(76) Xu, K.; Li, S.; Dong, S.; Zhang, S.; Pan, G.; Wang, G.; Shi, L.; Guo, W.; Yu, C.; Luo, J. Bioresorbable Electrode Array for Electrophysiological and Pressure Signal Recording in the Brain. *Adv. Healthc Mater.* **2019**, *8*, 1801649.
(77) Chen, P.; Xu, C.; Wu, P.; Liu, K.; Chen, F.; Chen, Y.; Dai, H.; Luo, Z. Wirelessly Powered Electrical-Stimulation Based on Biodegradable 3D Piezoelectric Scaffolds Promotes the Spinal Cord Injury Repair. *ACS Nano* **2022**, *16*, 16513−16528.
(78) Goonoo, N.; Bhaw-Luximon, A.; Rodriguez, I. A.; Wesner, D.; Schönherr, H.; Bowlin, G. L.; Jhurry, D. Poly(Ester-Ether) s: III. Assessment of Cell Behaviour on Nanofibrous Scaffolds of PCL, PLLA and PDX Blended with Amorphous PMeDX. *J. Mater. Chem. B* **2015**, *3*, 673−687.
(79) Guo, H.; D'Andrea, D.; Zhao, J.; Xu, Y.; Qiao, Z.; Janes, L. E.; Murthy, N. K.; Li, R.; Xie, Z.; Song, Z.; et al. Advanced Materials in Wireless, Implantable Electrical Stimulators That Offer Rapid Rates of Bioresorption for Peripheral Axon Regeneration. *Adv. Funct Mater.* **2021**, *31*, 2102724.
(80) Choi, Y. S.; Koo, J.; Lee, Y. J.; Lee, G.; Avila, R.; Ying, H.; Reeder, J.; Hambitzer, L.; Im, K.; Kim, J.; et al. Biodegradable Polyanhydrides as Encapsulation Layers for Transient Electronics. *Adv. Funct Mater.* **2020**, *30*, 2000941.
(81) Vey, E.; Roger, C.; Meehan, L.; Booth, J.; Claybourn, M.; Miller, A. F.; Saiani, A. Degradation Mechanism of Poly(Lactic-Co-Glycolic)

https://doi.org/10.1021/acs.chemrev.3c00408
Chem. Rev. XXXX, XXX, XXX−XXX

Acid Block Copolymer Cast Films in Phosphate Buffer Solution. *Polym. Degrad. Stab.* **2008**, *93*, 1869−1876.
(82) La Mattina, A. A.; Mariani, S.; Barillaro, G. Bioresorbable Materials on the Rise: From Electronic Components and Physical Sensors to In Vivo Monitoring Systems. *Advanced Science* **2020**, *7*, 1902872.
(83) Zheng, Q.; Zou, Y.; Zhang, Y.; Liu, Z.; Shi, B.; Wang, X.; Jin, Y.; Ouyang, H.; Li, Z.; Wang, Z. L. Biodegradable Triboelectric Nanogenerator as a Life-Time Designed Implantable Power Source. *Sci. Adv.* **2016**, *2*, e1501478.
(84) Tran, R. T.; Thevenot, P.; Gyawali, D.; Chiao, J.-C.; Tang, L.; Yang, J. Synthesis and Characterization of a Biodegradable Elastomer Featuring a Dual Crosslinking Mechanism. *Soft Matter* **2010**, *6*, 2449.
(85) Sharma, A. K.; Hota, P. V.; Matoka, D. J.; Fuller, N. J.; Jandali, D.; Thaker, H.; Ameer, G. A.; Cheng, E. Y. Urinary Bladder Smooth Muscle Regeneration Utilizing Bone Marrow Derived Mesenchymal Stem Cell Seeded Elastomeric Poly(1,8-Octanediol-Co-Citrate) Based Thin Films. *Biomaterials* **2010**, *31*, 6207−6217.
(86) Hwang, S.-W.; Tao, H.; Kim, D.-H.; Cheng, H.; Song, J.-K.; Rill, E.; Brenckle, M. A.; Panilaitis, B.; Won, S. M.; Kim, Y.-S.; et al. A Physically Transient Form of Silicon Electronics. *Science* **2012**, *337*, 1640−1644.
(87) Chang, J.-K.; Emon, M. A. B.; Li, C.-S.; Yang, Q.; Chang, H.-P.; Yang, Z.; Wu, C.-I.; Saif, M. T.; Rogers, J. A. Cytotoxicity and in Vitro Degradation Kinetics of Foundry-Compatible Semiconductor Nanomembranes and Electronic Microcomponents. *ACS Nano* **2018**, *12*, 9721−9732.
(88) Hwang, S.-W.; Park, G.; Edwards, C.; Corbin, E. A.; Kang, S.-K.; Cheng, H.; Song, J.-K.; Kim, J.-H.; Yu, S.; Ng, J.; et al. Dissolution Chemistry and Biocompatibility of Single-Crystalline Silicon Nanomembranes and Associated Materials for Transient Electronics. *ACS Nano* **2014**, *8*, 5843−5851.
(89) Seidel, H.; Csepregi, L.; Heuberger, A.; Baumgärtel, H. Anisotropic Etching of Crystalline Silicon in Alkaline Solutions: II. Influence of Dopants. *J. Electrochem. Soc.* **1990**, *137*, 3626−3632.
(90) Palik, E. D.; Bermudez, V. M.; Glembocki, O. J. Ellipsometric Study of the Etch-Stop Mechanism in Heavily Doped Silicon. *J. Electrochem. Soc.* **1985**, *132*, 135−141.
(91) Morita, M.; Ohmi, T.; Hasegawa, E.; Kawakami, M.; Ohwada, M. Growth of Native Oxide on a Silicon Surface. *J. Appl. Phys.* **1990**, *68*, 1272−1281.
(92) Yin, L.; Farimani, A. B.; Min, K.; Vishal, N.; Lam, J.; Lee, Y. K.; Aluru, N. R.; Rogers, J. A. Mechanisms for Hydrolysis of Silicon Nanomembranes as Used in Bioresorbable Electronics. *Adv. Mater.* **2015**, *27*, 1857−1864.
(93) Wang, L.; Gao, Y.; Dai, F.; Kong, D.; Wang, H.; Sun, P.; Shi, Z.; Sheng, X.; Xu, B.; Yin, L. Geometrical and Chemical-Dependent Hydrolysis Mechanisms of Silicon Nanomembranes for Biodegradable Electronics. *ACS Appl. Mater. Interfaces* **2019**, *11*, 18013−18023.
(94) Chiappini, C.; De Rosa, E.; Martinez, J. O.; Liu, X.; Steele, J.; Stevens, M. M.; Tasciotti, E. Biodegradable Silicon Nanoneedles Delivering Nucleic Acids Intracellularly Induce Localized in Vivo Neovascularization. *Nat. Mater.* **2015**, *14*, 532−539.
(95) Gopal, S.; Chiappini, C.; Penders, J.; Leonardo, V.; Seong, H.; Rothery, S.; Korchev, Y.; Shevchuk, A.; Stevens, M. M. Porous Silicon Nanoneedles Modulate Endocytosis to Deliver Biological Payloads. *Adv. Mater.* **2019**, *31*, 1806788.
(96) Park, W.; Nguyen, V. P.; Jeon, Y.; Kim, B.; Li, Y.; Yi, J.; Kim, H.; Leem, J. W.; Kim, Y. L.; Kim, D. R. Biodegradable Silicon Nanoneedles for Ocular Drug Delivery. *Sci. Adv.* **2022**, *8*, eabn1772.
(97) Zhou, W.; Dai, X.; Fu, T.-M.; Xie, C.; Liu, J.; Lieber, C. M. Long Term Stability of Nanowire Nanoelectronics in Physiological Environments. *Nano Lett.* **2014**, *14*, 1614−1619.
(98) Dagdeviren, C.; Hwang, S.-W.; Su, Y.; Kim, S.; Cheng, H.; Gur, O.; Haney, R.; Omenetto, F. G.; Huang, Y.; Rogers, J. A. Transient, Biocompatible Electronics and Energy Harvesters Based on ZnO. *Small* **2013**, *9*, 3398−3404.
(99) Jin, S. H.; Kang, S.-K.; Cho, I.-T.; Han, S. Y.; Chung, H. U.; Lee, D. J.; Shin, J.; Baek, G. W.; Kim, T.; Lee, J.-H.; et al. Water-Soluble Thin Film Transistors and Circuits Based on Amorphous Indium-Gallium-Zinc Oxide. *ACS Appl. Mater. Interfaces* **2015**, *7*, 8268−8274.
(100) Horasawa, N.; Nakajima, H.; Takahashi, S.; Okabe, T. Behavior of Pure Gallium in Water and Various Saline Solutions. *Dent Mater. J.* **1997**, *16*, 200−208 226.
(101) Gusakova, J.; Wang, X.; Shiau, L. L.; Krivosheeva, A.; Shaposhnikov, V.; Borisenko, V.; Gusakov, V.; Tay, B. K. Electronic Properties of Bulk and Monolayer TMDs: Theoretical Study Within DFT Framework (GVJ-2e Method). *physica status solidi (a)* **2017**, *214*, 1700218.
(102) Manzeli, S.; Ovchinnikov, D.; Pasquier, D.; Yazyev, O. V.; Kis, A. 2D Transition Metal Dichalcogenides. *Nat. Rev. Mater.* **2017**, *2*, 17033.
(103) Appel, J. H.; Li, D. O.; Podlevsky, J. D.; Debnath, A.; Green, A. A.; Wang, Q. H.; Chae, J. Low Cytotoxicity and Genotoxicity of Two-Dimensional MoS2 and WS2. *ACS Biomater Sci. Eng.* **2016**, *2*, 361−367.
(104) Chen, X.; Park, Y. J.; Kang, M.; Kang, S.-K.; Koo, J.; Shinde, S. M.; Shin, J.; Jeon, S.; Park, G.; Yan, Y.; et al. CVD-Grown Monolayer MoS2 in Bioabsorbable Electronics and Biosensors. *Nat. Commun.* **2018**, *9*, 1690.
(105) Guan, G.; Zhang, S.; Liu, S.; Cai, Y.; Low, M.; Teng, C. P.; Phang, I. Y.; Cheng, Y.; Duei, K. L.; Srinivasan, B. M.; et al. Protein Induces Layer-by-Layer Exfoliation of Transition Metal Dichalcogenides. *J. Am. Chem. Soc.* **2015**, *137*, 6152−6155.
(106) Li, X.; Shan, J.; Zhang, W.; Su, S.; Yuwen, L.; Wang, L. Recent Advances in Synthesis and Biomedical Applications of Two-Dimensional Transition Metal Dichalcogenide Nanosheets. *Small* **2017**, *13*, 1602660.
(107) Irimia-Vladu, M.; Głowacki, E. D.; Troshin, P. A.; Schwabegger, G.; Leonat, L.; Susarova, D. K.; Krystal, O.; Ullah, M.; Kanbur, Y.; Bodea, M. A.; et al. Indigo - A Natural Pigment for High Performance Ambipolar Organic Field Effect Transistors and Circuits. *Adv. Mater.* **2012**, *24*, 375−380.
(108) Zhou, W.; Liu, G.; Yang, B.; Ji, Q.; Xiang, W.; He, H.; Xu, Z.; Qi, C.; Li, S.; Yang, S.; et al. Review on Application of Perylene Diimide (PDI)-Based Materials in Environment: Pollutant Detection and Degradation. *Science of The Total Environment* **2021**, *780*, 146483.
(109) Adepu, V.; Tathacharya, M.; Fernandes, R. S.; Tiwari, A.; Siraj, S.; Kanungo, S.; Dey, N.; Sahatiya, P. Perylene Diimide (PDI) Based Flexible Multifunctional Sensor Design for Personal Healthcare Monitoring- A Complementary Approach Involving Experimental and Theoretical Investigations. *Adv. Mater. Technol.* **2023**, *8*, 2201633.
(110) Kulkarni, B.; Malhotra, M.; Jayakannan, M. Perylene-Tagged Polycaprolactone Block Copolymers and Their Enzyme-Biodegradable Fluorescent Nanoassemblies for Intracellular Bio-Imaging in Cancer Cells. *ACS Appl. Polym. Mater.* **2019**, *1*, 3375−3388.
(111) Trofymchuk, K.; Reisch, A.; Shulov, I.; Mély, Y.; Klymchenko, A. S. Tuning the Color and Photostability of Perylene Diimides inside Polymer Nanoparticles: Towards Biodegradable Substitutes of Quantum Dots. *Nanoscale* **2014**, *6*, 12934−12942.
(112) Capelli, R.; Amsden, J. J.; Generali, G.; Toffanin, S.; Benfenati, V.; Muccini, M.; Kaplan, D. L.; Omenetto, F. G.; Zamboni, R. Integration of Silk Protein in Organic and Light-Emitting Transistors. *Org. Electron* **2011**, *12*, 1146−1151.
(113) Chang, T.-H.; Liao, C.-P.; Tsai, J.-C.; Lee, C.-Y.; Hwang, J.-C.; Tso, I.-M.; Chueh, Y.-L.; Lyu, P.-C.; Gan, J.-Y. Natural Polyelectrolyte: Major Ampullate Spider Silk for Electrolyte Organic Field-Effect Transistors. *Org. Electron* **2014**, *15*, 954−960.
(114) Bonacchini, G. E.; Bossio, C.; Greco, F.; Mattoli, V.; Kim, Y.-H.; Lanzani, G.; Caironi, M. Tattoo-Paper Transfer as a Versatile Platform for All-Printed Organic Edible Electronics. *Adv. Mater.* **2018**, *30*, 1706091.
(115) Ko, J.; Nguyen, L. T. H.; Surendran, A.; Tan, B. Y.; Ng, K. W.; Leong, W. L. Human Hair Keratin for Biocompatible Flexible and Transient Electronic Devices. *ACS Appl. Mater. Interfaces* **2017**, *9*, 43004−43012.
(116) Goodwin, D. G.; Boyer, I.; Devahif, T.; Gao, C.; Frank, B. P.; Lu, X.; Kuwama, L.; Gordon, T. B.; Wang, J.; Ranville, J. F.; et al.

https://doi.org/10.1021/acs.chemrev.3c00408
Chem. Rev. XXXX, XXX, XXX−XXX

Biodegradation of Carbon Nanotube/Polymer Nanocomposites Using a Monoculture. *Environ. Sci. Technol.* **2018**, *52*, 40−51.
(117) Zare, Y.; Rhee, K. Y. Following the Morphological and Thermal Properties of PLA/PEO Blends Containing Carbon Nanotubes (CNTs) during Hydrolytic Degradation. *Compos B Eng.* **2019**, *175*, 107132.
(118) Yeh, J.-T.; Yang, M.-C.; Wu, C.-J.; Wu, C.-S. Preparation and Characterization of Biodegradable Polycaprolactone/Multiwalled Carbon Nanotubes Nanocomposites. *J. Appl. Polym. Sci.* **2009**, *112*, 660−668.
(119) Shih, Y. F.; Chen, L. S.; Jeng, R. J. Preparation and Properties of Biodegradable PBS/Multi-Walled Carbon Nanotube Nanocomposites. *Polymer (Guildf)* **2008**, *49*, 4602−4611.
(120) Thi, Q. V.; Ko, J.; Jo, Y.; Joo, Y. Ion-Incorporative, Degradable Nanocellulose Crystal Substrate for Sustainable Carbon-Based Electronics. *ACS Appl. Mater. Interfaces* **2022**, *14*, 43538−43546.
(121) Jin, S. H.; Shin, J.; Cho, I.-T.; Han, S. Y.; Lee, D. J.; Lee, C. H.; Lee, J.-H.; Rogers, J. A. Solution-Processed Single-Walled Carbon Nanotube Field Effect Transistors and Bootstrapped Inverters for Disintegratable, Transient Electronics. *Appl. Phys. Lett.* **2014**, *105*, 013506.
(122) Amirian, M.; Chakoli, A. N.; Cai, W.; Sui, J. Effect of Functionalized Multiwalled Carbon Nanotubes on Thermal Stability of Poly (L-LACTIDE) Biodegradable Polymer. *Scientia Iranica* **2013**, *20*, 1023−1027.
(123) Chakoli, A. N.; Wan, J.; Feng, J. T.; Amirian, M.; Sui, J. H.; Cai, W. Functionalization of Multiwalled Carbon Nanotubes for Reinforcing of Poly(l-Lactide-Co-ε-Caprolactone) Biodegradable Copolymers. *Appl. Surf. Sci.* **2009**, *256*, 170−177.
(124) Walther, S.; Polster, S.; Meyer, B.; Jank, M. P. M.; Ryssel, H.; Frey, L. Properties of SiO2 and Si3N4 as Gate Dielectrics for Printed ZnO Transistors. *Journal of Vacuum Science & Technology B, Nanotechnology and Microelectronics: Materials, Processing, Measurement, and Phenomena* **2011**, *29*, 01A601.
(125) Yu, K. J.; Kuzum, D.; Hwang, S.-W.; Kim, B. H.; Juul, H.; Kim, N. H.; Won, S. M.; Chiang, K.; Trumpis, M.; Richardson, A. G.; et al. Bioresorbable Silicon Electronics for Transient Spatiotemporal Mapping of Electrical Activity from the Cerebral Cortex. *Nat. Mater.* **2016**, *15*, 782−791.
(126) Hwang, S.-W.; Huang, X.; Seo, J.-H.; Song, J.-K.; Kim, S.; Hage-Ali, S.; Chung, H.-J.; Tao, H.; Omenetto, F. G.; Ma, Z.; et al. Materials for Bioresorbable Radio Frequency Electronics. *Adv. Mater.* **2013**, *25*, 3526−3531.
(127) Kang, S.-K.; Hwang, S.-W.; Cheng, H.; Yu, S.; Kim, B. H.; Kim, J.-H.; Huang, Y.; Rogers, J. A. Dissolution Behaviors and Applications of Silicon Oxides and Nitrides in Transient Electronics. *Adv. Funct Mater.* **2014**, *24*, 4427−4434.
(128) Lee, Y. K.; Yu, K. J.; Kim, Y.; Yoon, Y.; Xie, Z.; Song, E.; Luan, H.; Feng, X.; Huang, Y.; Rogers, J. A. Kinetics and Chemistry of Hydrolysis of Ultrathin, Thermally Grown Layers of Silicon Oxide as Biofluid Barriers in Flexible Electronic Systems. *ACS Appl. Mater. Interfaces* **2017**, *9*, 42633−42638.
(129) Fang, H.; Zhao, J.; Yu, K. J.; Song, E.; Farimani, A. B.; Chiang, C.-H.; Jin, X.; Xue, Y.; Xu, D.; Du, W.; et al. Ultrathin, Transferred Layers of Thermally Grown Silicon Dioxide as Biofluid Barriers for Biointegrated Flexible Electronic Systems. *Proc. Natl. Acad. Sci. U. S. A.* **2016**, *113*, 11682−11687.
(130) Li, S.; Yu, D.; Ji, H.; Zhao, B.; Ji, L.; Leng, X. In Vivo Degradation and Neovascularization of Silk Fibroin Implants Monitored by Multiple Modes Ultrasound for Surgical Applications. *Biomed Eng. Online* **2018**, *17*, 87.
(131) Huang, Y.; Li, H.; Hu, T.; Li, J.; Yiu, C. K.; Zhou, J.; Li, J.; Huang, X.; Yao, K.; Qiu, X.; et al. Implantable Electronic Medicine Enabled by Bioresorbable Microneedles for Wireless Electrotherapy and Drug Delivery. *Nano Lett.* **2022**, *22*, 5944−5953.
(132) Kim, H.; Lee, H. S.; Jeon, Y.; Park, W.; Zhang, Y.; Kim, B.; Jang, H.; Xu, B.; Yeo, Y.; Kim, D. R.; et al. Bioresorbable, Miniaturized Porous Silicon Needles on a Flexible Water-Soluble Backing for Unobtrusive, Sustained Delivery of Chemotherapy. *ACS Nano* **2020**, *14*, 7227−7236.
(133) Wetteland, C. L.; de Jesus Sanchez, J.; Silken, C. A.; Nguyen, N.-Y. T.; Mahmood, O.; Liu, H. Dissociation of Magnesium Oxide and Magnesium Hydroxide Nanoparticles in Physiologically Relevant Fluids. *J. Nanopart. Res.* **2018**, *20*, 215.
(134) Lendlein, A.; Langer, R. Biodegradable, Elastic Shape-Memory Polymers for Potential Biomedical Applications. *Science* **2002**, *296*, 1673−1676.
(135) George, A.; Shah, P. A.; Shrivastav, P. S. Natural Biodegradable Polymers Based Nano-Formulations for Drug Delivery: A Review. *Int. J. Pharm.* **2019**, *561*, 244−264.
(136) Kirillova, A.; Yeazel, T. R.; Asheghali, D.; Petersen, S. R.; Dort, S.; Gall, K.; Becker, M. L. Fabrication of Biomedical Scaffolds Using Biodegradable Polymers. *Chem. Rev.* **2021**, *121*, 11238−11304.
(137) Middleton, J. C.; Tipton, A. J. Synthetic Biodegradable Polymers as Orthopedic Devices. *Biomaterials* **2000**, *21*, 2335−2346.
(138) Kim, D.-H.; Viventi, J.; Amsden, J. J.; Xiao, J.; Vigeland, L.; Kim, Y.-S.; Blanco, J. A.; Panilaitis, B.; Frechette, E. S.; Contreras, D.; et al. Dissolvable Films of Silk Fibroin for Ultrathin Conformal Bio-Integrated Electronics. *Nat. Mater.* **2010**, *9*, 511−517.
(139) Tao, H.; Hwang, S.-W.; Marelli, B.; An, B.; Moreau, J. E.; Yang, M.; Brenckle, M. A.; Kim, S.; Kaplan, D. L.; Rogers, J. A.; et al. Silk-Based Resorbable Electronic Devices for Remotely Controlled Therapy and in Vivo Infection Abatement. *Proc. Natl. Acad. Sci. U. S. A.* **2014**, *111*, 17385−17389.
(140) Guo, C.; Li, C.; Kaplan, D. L. Enzymatic Degradation of Bombyx Mori Silk Materials: A Review. *Biomacromolecules* **2020**, *21*, 1678−1686.
(141) Brannigan, R. P.; Dove, A. P. Synthesis, Properties and Biomedical Applications of Hydrolytically Degradable Materials Based on Aliphatic Polyesters and Polycarbonates. *Biomater Sci.* **2017**, *5*, 9−21.
(142) von Burkersroda, F.; Schedl, L.; Göpferich, A. Why Degradable Polymers Undergo Surface Erosion or Bulk Erosion. *Biomaterials* **2002**, *23*, 4221−4231.
(143) Papanu, J. S.; Soane Soong, D. S.; Bell, A. T.; Hess, D. W. Transport Models for Swelling and Dissolution of Thin Polymer Films. *J. Appl. Polym. Sci.* **1989**, *38*, 859−885.
(144) Bouklas, N.; Huang, R. Swelling Kinetics of Polymer Gels: Comparison of Linear and Nonlinear Theories. *Soft Matter* **2012**, *8*, 8194.
(145) Hwang, S.-W.; Song, J.-K.; Huang, X.; Cheng, H.; Kang, S.-K.; Kim, B. H.; Kim, J.-H.; Yu, S.; Huang, Y.; Rogers, J. A. High-Performance Biodegradable/Transient Electronics on Biodegradable Polymers. *Adv. Mater.* **2014**, *26*, 3905−3911.
(146) Nair, L. S.; Laurencin, C. T. Biodegradable Polymers as Biomaterials. *Prog. Polym. Sci.* **2007**, *32*, 762−798.
(147) Hwang, S.-W.; Lee, C. H.; Cheng, H.; Jeong, J.-W.; Kang, S.-K.; Kim, J.-H.; Shin, J.; Yang, J.; Liu, Z.; Ameer, G. A.; et al. Biodegradable Elastomers and Silicon Nanomembranes/Nanoribbons for Stretchable, Transient Electronics, and Biosensors. *Nano Lett.* **2015**, *15*, 2801−2808.
(148) Feig, V. R.; Tran, H.; Bao, Z. Biodegradable Polymeric Materials in Degradable Electronic Devices. *ACS Cent Sci.* **2018**, *4*, 337−348.
(149) Horan, R. L.; Antle, K.; Collette, A. L.; Wang, Y.; Huang, J.; Moreau, J. E.; Volloch, V.; Kaplan, D. L.; Altman, G. H. In Vitro Degradation of Silk Fibroin. *Biomaterials* **2005**, *26*, 3385−3393.
(150) Hwang, S.-W.; Kang, S.-K.; Huang, X.; Brenckle, M. A.; Omenetto, F. G.; Rogers, J. A. Materials for Programmed, Functional Transformation in Transient Electronic Systems. *Adv. Mater.* **2015**, *27*, 47−52.
(151) Guo, J.; Liu, J.; Yang, B.; Zhan, G.; Kang, X.; Tian, H.; Tang, L.; Chen, X.; Yang, C. Low-Voltage Transient/Biodegradable Transistors Based on Free-Standing Sodium Alginate Membranes. *IEEE Electron Device Lett.* **2015**, *36*, 576−578.
(152) Kwon, K. Y.; Lee, J. S.; Ko, G.-J.; Sunwoo, S. H.; Lee, S.; Jo, Y. J.; Choi, C. H.; Hwang, S.-W.; Kim, T. Biosafe, Eco-Friendly Levan Polysaccharide toward Transient Electronics. *Small* **2018**, *14*, 1801332.

https://doi.org/10.1021/acs.chemrev.3c00408
Chem. Rev. XXXX, XXX, XXX−XXX

(153) Jung, Y. H.; Chang, T.-H.; Zhang, H.; Yao, C.; Zheng, Q.; Yang, V. W.; Mi, H.; Kim, M.; Cho, S. J.; Park, D.-W.; et al. High-Performance Green Flexible Electronics Based on Biodegradable Cellulose Nanofibril Paper. *Nat. Commun.* **2015**, *6*, 7170.
(154) Chang, J.-K.; Fang, H.; Bower, C. A.; Song, E.; Yu, X.; Rogers, J. A. Materials and Processing Approaches for Foundry-Compatible Transient Electronics. *Proc. Natl. Acad. Sci. U. S. A.* **2017**, *114*, E5522−E5529.
(155) Oh, J. Y.; Rondeau-Gagné, S.; Chiu, Y.-C.; Chortos, A.; Lissel, F.; Wang, G.-J. N.; Schroeder, B. C.; Kurosawa, T.; Lopez, J.; Katsumata, T.; et al. Intrinsically Stretchable and Healable Semiconducting Polymer for Organic Transistors. *Nature* **2016**, *539*, 411−415.
(156) Irimia-Vladu, M.; Troshin, P. A.; Reisinger, M.; Shmygleva, L.; Kanbur, Y.; Schwabegger, G.; Bodea, M.; Schwödiauer, R.; Mumyatov, A.; Fergus, J. W.; et al. Biocompatible and Biodegradable Materials for Organic Field-Effect Transistors. *Adv. Funct Mater.* **2010**, *20*, 4069−4076.
(157) Yang, Q.; Hu, Z.; Seo, M.-H.; Xu, Y.; Yan, Y.; Hsu, Y.-H.; Berkovich, J.; Lee, K.; Liu, T.-L.; McDonald, S.; et al. High-Speed, Scanned Laser Structuring of Multi-Layered Eco/Bioresorbable Materials for Advanced Electronic Systems. *Nat. Commun.* **2022**, *13*, 6518.
(158) Nyamayaro, K.; Keyvani, P.; D'Acierno, F.; Poisson, J.; Hudson, Z. M.; Michal, C. A.; Madden, J. D. W.; Hatzikiriakos, S. G.; Mehrkhodavandi, P. Toward Biodegradable Electronics: Ionic Diodes Based on a Cellulose Nanocrystal-Agarose Hydrogel. *ACS Appl. Mater. Interfaces* **2020**, *12*, 52182−52191.
(159) Huang, Y.; Cui, Y.; Deng, H.; Wang, J.; Hong, R.; Hu, S.; Hou, H.; Dong, Y.; Wang, H.; Chen, J.; et al. Bioresorbable Thin-Film Silicon Diodes for the Optoelectronic Excitation and Inhibition of Neural Activities. *Nat. Biomed Eng.* **2023**, *7*, 486−498.
(160) Jürgensen, N.; Ackermann, M.; Marszalek, T.; Zimmermann, J.; Morfa, A. J.; Pisula, W.; Bunz, U. H. F.; Hinkel, F.; Hernandez-Sosa, G. Solution-Processed Bio-OLEDs with a Vitamin-Derived Riboflavin Tetrabutyrate Emission Layer. *ACS Sustain Chem. Eng.* **2017**, *5*, 5368−5372.
(161) Lee, C. H.; Kim, H.; Harburg, D. V.; Park, G.; Ma, Y.; Pan, T.; Kim, J. S.; Lee, N. Y.; Kim, B. H.; Jang, K.-I.; et al. Biological Lipid Membranes for On-Demand, Wireless Drug Delivery from Thin, Bioresorbable Electronic Implants. *NPG Asia Mater.* **2015**, *7*, No. e227-e227.
(162) Xu, W.; Yang, H.; Zeng, W.; Houghton, T.; Wang, X.; Murthy, R.; Kim, H.; Lin, Y.; Mignolet, M.; Duan, H.; et al. Food-Based Edible and Nutritive Electronics. *Adv. Mater. Technol.* **2017**, *2*, 1700181.
(163) Choi, Y. S.; Hsueh, Y.-Y.; Koo, J.; Yang, Q.; Avila, R.; Hu, B.; Xie, Z.; Lee, G.; Ning, Z.; Liu, C.; et al. Stretchable, Dynamic Covalent Polymers for Soft, Long-Lived Bioresorbable Electronic Stimulators Designed to Facilitate Neuromuscular Regeneration. *Nat. Commun.* **2020**, *11*, 5990.
(164) Boutry, C. M.; Chandrahalim, H.; Streit, P.; Schinhammer, M.; Hänzi, A. C.; Hierold, C. Characterization of Miniaturized RLC Resonators Made of Biodegradable Materials for Wireless Implant Applications. *Sens Actuators A Phys.* **2013**, *189*, 344−355.
(165) Luo, M.; Shen, W.; Allen, M. G. Microfabricated PLGA/PVA-Based Completely Biodegradable Passive RF Pressure Sensors. In *2015 Transducers—2015 18th International Conference on Solid-State Sensors, Actuators and Microsystems (TRANSDUCERS)*; IEEE, 2015; pp 101−104.
(166) Luo, M.; Martinez, A. W.; Song, C.; Herrault, F.; Allen, M. G. A Microfabricated Wireless RF Pressure Sensor Made Completely of Biodegradable Materials. *Journal of Microelectromechanical Systems* **2014**, *23*, 4−13.
(167) Palmroth, A.; Salpavaara, T.; Vuoristo, P.; Karjalainen, S.; Kääriäinen, T.; Miettinen, S.; Massera, J.; Lekkala, J.; Kellomäki, M. Materials and Orthopedic Applications for Bioresorbable Inductively Coupled Resonance Sensors. *ACS Appl. Mater. Interfaces* **2020**, *12*, 31148−31161.
(168) Lu, D.; Yan, Y.; Avila, R.; Kandela, I.; Stepien, I.; Seo, M.; Bai, W.; Yang, Q.; Li, C.; Haney, C. R.; et al. Bioresorbable, Wireless, Passive Sensors as Temporary Implants for Monitoring Regional Body Temperature. *Adv. Healthc Mater.* **2020**, *9*, 2000942.
(169) Lu, D.; Yan, Y.; Deng, Y.; Yang, Q.; Zhao, J.; Seo, M.; Bai, W.; MacEwan, M. R.; Huang, Y.; Ray, W. Z.; et al. Bioresorbable Wireless Sensors as Temporary Implants for In Vivo Measurements of Pressure. *Adv. Funct Mater.* **2020**, *30*, 2003754.
(170) Shou, W.; Mahajan, B. K.; Ludwig, B.; Yu, X.; Staggs, J.; Huang, X.; Pan, H. Low-Cost Manufacturing of Bioresorbable Conductors by Evaporation-Condensation-Mediated Laser Printing and Sintering of Zn Nanoparticles. *Adv. Mater.* **2017**, *29*, 1700172.
(171) Shin, J.; Yan, Y.; Bai, W.; Xue, Y.; Gamble, P.; Tian, L.; Kandela, I.; Haney, C. R.; Spees, W.; Lee, Y.; et al. Bioresorbable Pressure Sensors Protected with Thermally Grown Silicon Dioxide for the Monitoring of Chronic Diseases and Healing Processes. *Nat. Biomed Eng.* **2019**, *3*, 37−46.
(172) Ando, M.; Kawamura, H.; Kitada, H.; Sekimoto, Y.; Inoue, T.; Tajitsu, Y. Pressure-Sensitive Touch Panel Based on Piezoelectric Poly(L-Lactic Acid) Film. *Jpn. J. Appl. Phys.* **2013**, *52*, 09KD17.
(173) Yoshida, M.; Onogi, T.; Onishi, K.; Inagaki, T.; Tajitsu, Y. High Piezoelectric Performance of Poly(Lactic Acid) Film Manufactured by Solid-State Extrusion. *Jpn. J. Appl. Phys.* **2014**, *53*, 09PC02.
(174) Curry, E. J.; Ke, K.; Chorsi, M. T.; Wrobel, K. S.; Miller, A. N.; Patel, A.; Kim, I.; Feng, J.; Yue, L.; Wu, Q.; et al. Biodegradable Piezoelectric Force Sensor. *Proc. Natl. Acad. Sci. U. S. A.* **2018**, *115*, 909−914.
(175) Curry, E. J.; Le, T. T.; Das, R.; Ke, K.; Santorella, E. M.; Paul, D.; Chorsi, M. T.; Tran, K. T. M.; Baroody, J.; Borges, E. R.; et al. Biodegradable Nanofiber-Based Piezoelectric Transducer. *Proc. Natl. Acad. Sci. U. S. A.* **2020**, *117*, 214−220.
(176) Hosseini, E. S.; Manjakkal, L.; Shakthivel, D.; Dahiya, R. Glycine-Chitosan-Based Flexible Biodegradable Piezoelectric Pressure Sensor. *ACS Appl. Mater. Interfaces* **2020**, *12*, 9008−9016.
(177) Li, Z.; Li, C.; Deng, Y. Bioresorbable Pressure Sensor and Its Applications in Abnormal Respiratory Event Identification. *ACS Appl. Electron Mater.* **2023**, *5*, 1761−1769.
(178) Ouyang, H.; Li, Z.; Gu, M.; Hu, Y.; Xu, L.; Jiang, D.; Cheng, S.; Zou, Y.; Deng, Y.; Shi, B.; et al. A Bioresorbable Dynamic Pressure Sensor for Cardiovascular Postoperative Care. *Adv. Mater.* **2021**, *33*, 2102302.
(179) Boutry, C. M.; Nguyen, A.; Lawal, Q. O.; Chortos, A.; Rondeau-Gagné, S.; Bao, Z. A Sensitive and Biodegradable Pressure Sensor Array for Cardiovascular Monitoring. *Adv. Mater.* **2015**, *27*, 6954−6961.
(180) Tee, B. C.-K.; Chortos, A.; Dunn, R. R.; Schwartz, G.; Eason, E.; Bao, Z. Tunable Flexible Pressure Sensors Using Microstructured Elastomer Geometries for Intuitive Electronics. *Adv. Funct Mater.* **2014**, *24*, 5427−5434.
(181) Boutry, C. M.; Kaizawa, Y.; Schroeder, B. C.; Chortos, A.; Legrand, A.; Wang, Z.; Chang, J.; Fox, P.; Bao, Z. A Stretchable and Biodegradable Strain and Pressure Sensor for Orthopaedic Application. *Nat. Electron* **2018**, *1*, 314−321.
(182) Salvatore, G. A.; Sülzle, J.; Dalla Valle, F.; Cantarella, G.; Robotti, F.; Jokic, P.; Knobelspies, S.; Daus, A.; Büthe, L.; Petti, L.; et al. Biodegradable and Highly Deformable Temperature Sensors for the Internet of Things. *Adv. Funct Mater.* **2017**, *27*, 1702390.
(183) Fan, J. A.; Yeo, W.-H.; Su, Y.; Hattori, Y.; Lee, W.; Jung, S.-Y.; Zhang, Y.; Liu, Z.; Cheng, H.; Falgout, L.; et al. Fractal Design Concepts for Stretchable Electronics. *Nat. Commun.* **2014**, *5*, 3266.
(184) Yi, N.; Cheng, Z.; Yang, L.; Edelman, G.; Xue, C.; Ma, Y.; Zhu, H.; Cheng, H. Fully Water-Soluble, High-Performance Transient Sensors on a Versatile Galactomannan Substrate Derived from the Endosperm. *ACS Appl. Mater. Interfaces* **2018**, *10*, 36664−36674.
(185) Santra, S.; Guha, P. K.; Ali, S. Z.; Haneef, I.; Udrea, F. Silicon on Insulator Diode Temperature Sensor- A Detailed Analysis for Ultra-High Temperature Operation. *IEEE Sens J.* **2010**, *10*, 997−1003.
(186) Dautta, M.; Alshetaiwi, M.; Escobar, A.; Torres, F.; Bernardo, N.; Tseng, P. Multi-Functional Hydrogel-Interlayer RF/NFC Reso-

https://doi.org/10.1021/acs.chemrev.3c00408
Chem. Rev. XXXX, XXX, XXX−XXX

nators as a Versatile Platform for Passive and Wireless Biosensing. *Adv. Electron Mater.* **2020**, *6*, 1901311.
(187) Karim, H.; Delfin, D.; Chavez, L. A.; Delfin, L.; Martinez, R.; Avila, J.; Rodriguez, C.; Rumpf, R. C.; Love, N.; Lin, Y. Metamaterial Based Passive Wireless Temperature Sensor. *Adv. Eng. Mater.* **2017**, *19*, 1600741.
(188) Tseng, P.; Napier, B.; Garbarini, L.; Kaplan, D. L.; Omenetto, F. G. Functional, RF-Trilayer Sensors for Tooth-Mounted, Wireless Monitoring of the Oral Cavity and Food Consumption. *Adv. Mater.* **2018**, *30*, 1703257.
(189) Webb, R. C.; Bonifas, A. P.; Behnaz, A.; Zhang, Y.; Yu, K. J.; Cheng, H.; Shi, M.; Bian, Z.; Liu, Z.; Kim, Y.-S.; et al. Ultrathin Conformal Devices for Precise and Continuous Thermal Characterization of Human Skin. *Nat. Mater.* **2013**, *12*, 938−944.
(190) King-Stephens, D.; Mirro, E.; Weber, P. B.; Laxer, K. D.; Van Ness, P. C.; Salanova, V.; Spencer, D. C.; Heck, C. N.; Goldman, A.; Jobst, B.; et al. Lateralization of Mesial Temporal Lobe Epilepsy with Chronic Ambulatory Electrocorticography. *Epilepsia* **2015**, *56*, 959−967.
(191) Corsi, M.; Paghi, A.; Mariani, S.; Golinelli, G.; Debrassi, A.; Egri, G.; Leo, G.; Vandini, E.; Vilella, A.; Dähne, L.; et al. Bioresorbable Nanostructured Chemical Sensor for Monitoring of PH Level In Vivo. *Advanced Science* **2022**, *9*, 2202062.
(192) Aeby, X.; Bourely, J.; Poulin, A.; Siqueira, G.; Nyström, G.; Briand, D. Printed Humidity Sensors from Renewable and Biodegradable Materials. *Adv. Mater. Technol.* **2023**, *8*, 2201302.
(193) Kim, H.-S.; Yang, S. M.; Jang, T.-M.; Oh, N.; Kim, H.-S.; Hwang, S.-W. Bioresorbable Silicon Nanomembranes and Iron Catalyst Nanoparticles for Flexible, Transient Electrochemical Dopamine Monitors. *Adv. Healthc Mater.* **2018**, *7*, 1801071.
(194) Li, J.; Liu, J.; Wu, Z.; Shang, X.; Li, Y.; Huo, W.; Huang, X. Fully Printed and Self-Compensated Bioresorbable Electrochemical Devices Based on Galvanic Coupling for Continuous Glucose Monitoring. *Sci. Adv.* **2023**, *9*, eadi3839.
(195) Li, R.; Qi, H.; Ma, Y.; Deng, Y.; Liu, S.; Jie, Y.; Jing, J.; He, J.; Zhang, X.; Wheatley, L.; et al. A Flexible and Physically Transient Electrochemical Sensor for Real-Time Wireless Nitric Oxide Monitoring. *Nat. Commun.* **2020**, *11*, 3207.
(196) Ko, G.-J.; Han, S. D.; Kim, J.-K.; Zhu, J.; Han, W. B.; Chung, J.; Yang, S. M.; Cheng, H.; Kim, D.-H.; Kang, C.-Y.; et al. Biodegradable, Flexible Silicon Nanomembrane-Based NOx Gas Sensor System with Record-High Performance for Transient Environmental Monitors and Medical Implants. *NPG Asia Mater.* **2020**, *12*, 71.
(197) Applegate, M. B.; Perotto, G.; Kaplan, D. L.; Omenetto, F. G. Biocompatible Silk Step-Index Optical Waveguides. *Biomed Opt Express* **2015**, *6*, 4221.
(198) Nizamoglu, S.; Gather, M. C.; Humar, M.; Choi, M.; Kim, S.; Kim, K. S.; Hahn, S. K.; Scarcelli, G.; Randolph, M.; Redmond, R. W.; et al. Bioabsorbable Polymer Optical Waveguides for Deep-Tissue Photomedicine. *Nat. Commun.* **2016**, *7*, 10374.
(199) Fu, R.; Luo, W.; Nazempour, R.; Tan, D.; Ding, H.; Zhang, K.; Yin, L.; Guan, J.; Sheng, X. Implantable and Biodegradable Poly(l-Lactic Acid) Fibers for Optical Neural Interfaces. *Adv. Opt Mater.* **2018**, *6*, 1700941.
(200) Feng, J.; Zheng, Y.; Bhusari, S.; Villiou, M.; Pearson, S.; del Campo, A. Printed Degradable Optical Waveguides for Guiding Light into Tissue. *Adv. Funct Mater.* **2020**, *30*, 2004327.
(201) Bai, W.; Yang, H.; Ma, Y.; Chen, H.; Shin, J.; Liu, Y.; Yang, Q.; Kandela, I.; Liu, Z.; Kang, S.; et al. Flexible Transient Optical Waveguides and Surface-Wave Biosensors Constructed from Monocrystalline Silicon. *Adv. Mater.* **2018**, *30*, 1801584.
(202) Bai, W.; Irie, M.; Liu, Z.; Luan, H.; Franklin, D.; Nandoliya, K.; Guo, H.; Zang, H.; Weng, Y.; Lu, D. Bioresorbable Multilayer Photonic Cavities as Temporary Implants for Tether-Free Measurements of Regional Tissue Temperatures. *BME Front* **2021**, *2021*, 8653218.
(203) Shin, J.; Liu, Z.; Bai, W.; Liu, Y.; Yan, Y.; Xue, Y.; Kandela, I.; Pezhouh, M.; MacEwan, M. R.; Huang, Y. Bioresorbable Optical Sensor Systems for Monitoring of Intracranial Pressure and Temperature. *Sci. Adv.* **2019**, *5*, eaaw1899.
(204) Franklin, D.; Ueltschi, T.; Carlini, A.; Yao, S.; Reeder, J.; Richards, B.; Van Duyne, R. P.; Rogers, J. A. Bioresorbable Microdroplet Lasers as Injectable Systems for Transient Thermal Sensing and Modulation. *ACS Nano* **2021**, *15*, 2327−2339.
(205) Amsden, J. J.; Domachuk, P.; Gopinath, A.; White, R. D.; Negro, L. D.; Kaplan, D. L.; Omenetto, F. G. Rapid Nanoimprinting of Silk Fibroin Films for Biophotonic Applications. *Adv. Mater.* **2010**, *22*, 1746−1749.
(206) Lawrence, B. D.; Cronin-Golomb, M.; Georgakoudi, I.; Kaplan, D. L.; Omenetto, F. G. Bioactive Silk Protein Biomaterial Systems for Optical Devices. *Biomacromolecules* **2008**, *9*, 1214−1220.
(207) Perry, H.; Gopinath, A.; Kaplan, D. L.; Dal Negro, L.; Omenetto, F. G. Nano- and Micropatterning of Optically Transparent, Mechanically Robust, Biocompatible Silk Fibroin Films. *Adv. Mater.* **2008**, *20*, 3070−3072.
(208) Domachuk, P.; Perry, H.; Amsden, J. J.; Kaplan, D. L.; Omenetto, F. G. Bioactive "Self-Sensing" Optical Systems. *Appl. Phys. Lett.* **2009**, *95*, 253702.
(209) Li, R.; Xie, S.; Zhang, L.; Li, L.; Kong, D.; Wang, Q.; Xin, R.; Sheng, X.; Yin, L.; Yu, C.; et al. Soft and Transient Magnesium Plasmonics for Environmental and Biomedical Sensing. *Nano Res.* **2018**, *11*, 4390−4400.
(210) Shim, J.-S.; Rogers, J. A.; Kang, S.-K. Physically Transient Electronic Materials and Devices. *Materials Science and Engineering: R: Reports* **2021**, *145*, 100624.
(211) Lyu, Y.; Wang, Y. Output Optimization of Biodegradable Triboelectric Nanogenerators. *Nano Energy* **2022**, *103*, 107811.
(212) Hosseini, E. S.; Dervin, S.; Ganguly, P.; Dahiya, R. Biodegradable Materials for Sustainable Health Monitoring Devices. *ACS Appl. Bio Mater.* **2021**, *4*, 163−194.
(213) Singh, R.; Bathaei, M. J.; Istif, E.; Beker, L. A Review of Bioresorbable Implantable Medical Devices: Materials, Fabrication, and Implementation. *Adv. Healthc Mater.* **2020**, *9*, 2000790.
(214) Rajaram, K.; Yang, S. M.; Hwang, S.-W. Transient, Biodegradable Energy Systems as a Promising Power Solution for Ecofriendly and Implantable Electronics. *Adv. Energy Sustain. Res.* **2022**, *3*, 2100223.
(215) Chatterjee, S.; Saxena, M.; Padmanabhan, D.; Jayachandra, M.; Pandya, H. J. Futuristic Medical Implants Using Bioresorbable Materials and Devices. *Biosens Bioelectron* **2019**, *142*, 111489.
(216) Liu, T.; Feng, X.; Jin, X.; Shao, M.; Su, Y.; Zhang, Y.; Zhang, X. Protecting the Lithium Metal Anode for a Safe Flexible Lithium-Air Battery in Ambient Air. *Angew. Chem.* **2019**, *131*, 18408−18413.
(217) Lei, X.; Liu, X.; Ma, W.; Cao, Z.; Wang, Y.; Ding, Y. Flexible Lithium-Air Battery in Ambient Air with an In Situ Formed Gel Electrolyte. *Angew. Chem.* **2018**, *130*, 16363−16367.
(218) Zhou, J.; Li, Y.; Xie, L.; Xu, R.; Zhang, R.; Gao, M.; Tian, W.; Li, D.; Qiao, L.; Wang, T.; et al. Humidity-Sensitive, Shape-Controllable, and Transient Zinc-Ion Batteries Based on Plasticizing Gelatin-Silk Protein Electrolytes. *Mater. Today Energy* **2021**, *21*, 100712.
(219) Wang, P.; Hu, M.; Wang, H.; Chen, Z.; Feng, Y.; Wang, J.; Ling, W.; Huang, Y. The Evolution of Flexible Electronics: From Nature, Beyond Nature, and To Nature. *Advanced Science* **2020**, *7*, 2001116.
(220) Yang, P.; Li, J.; Lee, S. W.; Fan, H. J. Printed Zinc Paper Batteries. *Advanced Science* **2022**, *9*, 2103894.
(221) Hawkins, B. E.; Turney, D. E.; Messinger, R. J.; Kiss, A. M.; Yadav, G. G.; Banerjee, S.; Lambert, T. N. Electroactive ZnO: Mechanisms, Conductivity, and Advances in Zn Alkaline Battery Cycling. *Adv. Energy Mater.* **2022**, *12*, 2103294.
(222) Nguyen, T. P.; Easley, A. D.; Kang, N.; Khan, S.; Lim, S.-M.; Rezenom, Y. H.; Wang, S.; Tran, D. K.; Fan, J.; Letteri, R. A.; et al. Polypeptide Organic Radical Batteries. *Nature* **2021**, *593*, 61−66.
(223) Huang, X.; Hou, H.; Yu, B.; Bai, J.; Guan, Y.; Wang, L.; Chen, K.; Wang, X.; Sun, P.; Deng, Y.; et al. Fully Biodegradable and Long-Term Operational Primary Zinc Batteries as Power Sources for Electronic Medicine. *ACS Nano* **2023**, *17*, 5727−5739.
(224) Yin, L.; Huang, X.; Xu, H.; Zhang, Y.; Lam, J.; Cheng, J.; Rogers, J. A. Materials, Designs, and Operational Characteristics for Fully Biodegradable Primary Batteries. *Adv. Mater.* **2014**, *26*, 3879−3884.

https://doi.org/10.1021/acs.chemrev.3c00408
Chem. Rev. XXXX, XXX, XXX−XXX

(225) Tsang, M.; Armutlulu, A.; Martinez, A. W.; Allen, S. A. B.; Allen, M. G. Biodegradable Magnesium/Iron Batteries with Polycaprolactone Encapsulation: A Microfabricated Power Source for Transient Implantable Devices. *Microsyst Nanoeng* **2015**, *1*, 15024.
(226) Khan, M. M.; Rahman, Z. U.; Deen, K. M.; Shabib, I.; Haider, W. Sputtered Mg100-XZnx ($0 \leq x \leq 100$) Systems as Anode Materials for a Biodegradable Battery Aimed for Transient Bioelectronics. *Electrochim. Acta* **2020**, *329*, 135129.
(227) Huang, X.; Wang, D.; Yuan, Z.; Xie, W.; Wu, Y.; Li, R.; Zhao, Y.; Luo, D.; Cen, L.; Chen, B.; et al. A Fully Biodegradable Battery for Self-Powered Transient Implants. *Small* **2018**, *14*, 1800994.
(228) Huang, I.; Zhang, Y.; Arafa, H. M.; Li, S.; Vazquez-Guardado, A.; Ouyang, W.; Liu, F.; Madhvapathy, S.; Song, J. W.; Tzavelis, A.; et al. High Performance Dual-Electrolyte Magnesium-Iodine Batteries That Can Harmlessly Resorb in the Environment or in the Body. *Energy Environ. Sci.* **2022**, *15*, 4095−4108.
(229) Karami-Mosammam, M.; Danninger, D.; Schiller, D.; Kaltenbrunner, M. Stretchable and Biodegradable Batteries with High Energy and Power Density. *Adv. Mater.* **2022**, *34*, 2204457.
(230) Dong, Y.; Li, J.; Yang, F.; Wang, Y.; Zhang, Z.; Wang, J.; Long, Y.; Wang, X. Bioresorbable Primary Battery Anodes Built on Core-Double-Shell Zinc Microparticle Networks. *ACS Appl. Mater. Interfaces* **2021**, *13*, 14275−14282.
(231) Mei, T.; Wang, C.; Liao, M.; Li, J.; Wang, L.; Tang, C.; Sun, X.; Wang, B.; Peng, H. A Biodegradable and Rechargeable Fiber Battery. *J. Mater. Chem. A Mater.* **2021**, *9*, 10104−10109.
(232) Jia, X.; Ma, X.; Zhao, L.; Xin, M.; Hao, Y.; Sun, P.; Wang, C.; Chao, D.; Liu, F.; Wang, C.; et al. A Biocompatible and Fully Erodible Conducting Polymer Enables Implanted Rechargeable Zn Batteries. *Chem. Sci.* **2023**, *14*, 2123−2130.
(233) Lee, M. H.; Lee, J.; Jung, S.; Kang, D.; Park, M. S.; Cha, G. D.; Cho, K. W.; Song, J.; Moon, S.; Yun, Y. S.; et al. A Biodegradable Secondary Battery and Its Biodegradation Mechanism for Eco-Friendly Energy-Storage Systems. *Adv. Mater.* **2021**, *33*, 2004902.
(234) Jia, X.; Wang, C.; Ranganathan, V.; Napier, B.; Yu, C.; Chao, Y.; Forsyth, M.; Omenetto, F. G.; MacFarlane, D. R.; Wallace, G. G. A Biodegradable Thin-Film Magnesium Primary Battery Using Silk Fibroin-Ionic Liquid Polymer Electrolyte. *ACS Energy Lett.* **2017**, *2*, 831−836.
(235) Zhu, M.; Huang, Y.; Huang, Y.; Pei, Z.; Xue, Q.; Li, H.; Geng, H.; Zhi, C. Capacitance Enhancement in a Semiconductor Nanostructure-Based Supercapacitor by Solar Light and a Self-Powered Supercapacitor-Photodetector System. *Adv. Funct Mater.* **2016**, *26*, 4481−4490.
(236) Yang, L.; Song, L.; Feng, Y.; Cao, M.; Zhang, P.; Zhang, X.-F.; Yao, J. Zinc Ion Trapping in a Cellulose Hydrogel as a Solid Electrolyte for a Safe and Flexible Supercapacitor. *J. Mater. Chem. A Mater.* **2020**, *8*, 12314−12318.
(237) Shao, M.; Sheng, H.; Lin, L.; Ma, H.; Wang, Q.; Yuan, J.; Zhang, X.; Chen, G.; Li, W.; Su, Q.; et al. High-Performance Biodegradable Energy Storage Devices Enabled by Heterostructured MoO 3 -MoS 2 Composites. *Small* **2023**, *19*, 2205529.
(238) Li, H.; Zhao, C.; Wang, X.; Meng, J.; Zou, Y.; Noreen, S.; Zhao, L.; Liu, Z.; Ouyang, H.; Tan, P.; et al. Fully Bioabsorbable Capacitor as an Energy Storage Unit for Implantable Medical Electronics. *Advanced Science* **2019**, *6*, 1801625.
(239) Zhang, Z.; Deng, J.; Li, X.; Yang, Z.; He, S.; Chen, X.; Guan, G.; Ren, J.; Peng, H. Superelastic Supercapacitors with High Performances during Stretching. *Adv. Mater.* **2015**, *27*, 356−362.
(240) Choi, C.; Kim, S. H.; Sim, H. J.; Lee, J. A.; Choi, A. Y.; Kim, Y. T.; Lepró, X.; Spinks, G. M.; Baughman, R. H.; Kim, S. J. Stretchable, Weavable Coiled Carbon Nanotube/MnO2/Polymer Fiber Solid-State Supercapacitors. *Sci. Rep* **2015**, *5*, 9387.
(241) Meng, Y.; Zhao, Y.; Hu, C.; Cheng, H.; Hu, Y.; Zhang, Z.; Shi, G.; Qu, L. All-Graphene Core-Sheath Microfibers for All-Solid-State, Stretchable Fibriform Supercapacitors and Wearable Electronic Textiles. *Adv. Mater.* **2013**, *25*, 2326−2331.
(242) Lee, H.; Lee, G.; Yun, J.; Keum, K.; Hong, S. Y.; Song, C.; Kim, J. W.; Lee, J. H.; Oh, S. Y.; Kim, D. S.; et al. Facile Fabrication of a Fully Biodegradable and Stretchable Serpentine-Shaped Wire Supercapacitor. *Chemical Engineering Journal* **2019**, *366*, 62−71.
(243) Tian, W.; Li, Y.; Zhou, J.; Wang, T.; Zhang, R.; Cao, J.; Luo, M.; Li, N.; Zhang, N.; Gong, H.; et al. Implantable and Biodegradable Micro-Supercapacitor Based on a Superassembled Three-Dimensional Network Zn@PPy Hybrid Electrode. *ACS Appl. Mater. Interfaces* **2021**, *13*, 8285−8293.
(244) Sheng, H.; Zhou, J.; Li, B.; He, Y.; Zhang, X.; Liang, J.; Zhou, J.; Su, Q.; Xie, E.; Lan, W. A Thin, Deformable, High-Performance Supercapacitor Implant That Can Be Biodegraded and Bioabsorbed within an Animal Body. *Sci. Adv.* **2021**, *7*, eabe3097.
(245) Wang, X.; Xu, W.; Chatterjee, P.; Lv, C.; Popovich, J.; Song, Z.; Dai, L.; Kalani, M. Y. S.; Haydel, S. E.; Jiang, H. Food-Materials-Based Edible Supercapacitors. *Adv. Mater. Technol.* **2016**, *1*, 1600059.
(246) Chen, K.; Yan, L.; Sheng, Y.; Ma, Y.; Qu, L.; Zhao, Y. An Edible and Nutritive Zinc-Ion Micro-Supercapacitor in the Stomach with Ultrahigh Energy Density. *ACS Nano* **2022**, *16*, 15261−15272.
(247) Beardslee, L. A.; Banis, G. E.; Chu, S.; Liu, S.; Chapin, A. A.; Stine, J. M.; Pasricha, P. J.; Ghodssi, R. Ingestible Sensors and Sensing Systems for Minimally Invasive Diagnosis and Monitoring: The Next Frontier in Minimally Invasive Screening. *ACS Sens* **2020**, *5*, 891−910.
(248) Huang, X.; Wang, L.; Wang, H.; Zhang, B.; Wang, X.; Stening, R. Y. Z.; Sheng, X.; Yin, L. Materials Strategies and Device Architectures of Emerging Power Supply Devices for Implantable Bioelectronics. *Small* **2020**, *16*, 1902827.
(249) Li, T.; Lee, P. S. Piezoelectric Energy Harvesting Technology: From Materials, Structures, to Applications. *Small Struct* **2022**, *3*, 2100128.
(250) Tao, Z.; Yuan, H.; Ding, S.; Wang, Y.; Hu, W.; Yang, R. Diphenylalanine-Based Degradable Piezoelectric Nanogenerators Enabled by Polylactic Acid Polymer-Assisted Transfer. *Nano Energy* **2021**, *88*, 106229.
(251) Sarıipek, F. B.; Özaytekin, İ.; Erci, F. Effect of Ultrasound Treatment on Bacteriostatic Activity of Piezoelectric PHB-TiO2 Hybrid Biodegradable Scaffolds Prepared by Electrospinning Technique. *J. Appl. Polym. Sci.* **2023**, *140*, e53437.
(252) Sohn, C.; Kim, H.; Han, J.; Lee, K.-T.; Šutka, A.; Jeong, C. K. Generating Electricity from Molecular Bonding-Correlated Piezoresponse of Biodegradable Silk Nanofibers. *Nano Energy* **2022**, *103*, 107844.
(253) Wang, Z. L.; Song, J. Piezoelectric Nanogenerators Based on Zinc Oxide Nanowire Arrays. *Science* **2006**, *312*, 242−246.
(254) Wu, P.; Chen, P.; Xu, C.; Wang, Q.; Zhang, F.; Yang, K.; Jiang, W.; Feng, J.; Luo, Z. Ultrasound-Driven in Vivo Electrical Stimulation Based on Biodegradable Piezoelectric Nanogenerators for Enhancing and Monitoring the Nerve Tissue Repair. *Nano Energy* **2022**, *102*, 107707.
(255) Das, R.; Curry, E. J.; Le, T. T.; Awale, G.; Liu, Y.; Li, S.; Contreras, J.; Bednarz, C.; Millender, J.; Xin, X.; et al. Biodegradable Nanofiber Bone-Tissue Scaffold as Remotely-Controlled and Self-Powering Electrical Stimulator. *Nano Energy* **2020**, *76*, 105028.
(256) Liu, Y.; Dzidotor, G.; Le, T. T.; Vinikoor, T.; Morgan, K.; Curry, E. J.; Das, R.; McClinton, A.; Eisenberg, E.; Apuzzo, L. N. Exercise-Induced Piezoelectric Stimulation for Cartilage Regeneration in Rabbits. *Sci. Transl Med.* **2022**, *14*, eabi7282.
(257) Karanth, D.; Puleo, D.; Dawson, D.; Holliday, L. S.; Sharab, L. Characterization of 3D Printed Biodegradable Piezoelectric Scaffolds for Bone Regeneration. *Clin Exp Dent Res.* **2023**, *9*, 398−408.
(258) Chernozem, R. V.; Romanyuk, K. N.; Grubova, I.; Chernozem, P. V.; Surmeneva, M. A.; Mukhortova, Y. R.; Wilhelm, M.; Ludwig, T.; Mathur, S.; Kholkin, A. L.; et al. Enhanced Piezoresponse and Surface Electric Potential of Hybrid Biodegradable Polyhydroxybutyrate Scaffolds Functionalized with Reduced Graphene Oxide for Tissue Engineering. *Nano Energy* **2021**, *89*, 106473.
(259) Peng, J.; Kang, S. D.; Snyder, G. J. Optimization Principles and the Figure of Merit for Triboelectric Generators. *Sci. Adv.* **2017**, *3*, eaap8576.
(260) Zhao, Z.; Zhou, L.; Li, S.; Liu, D.; Li, Y.; Gao, Y.; Liu, Y.; Dai, Y.; Wang, J.; Wang, Z. L. Selection Rules of Triboelectric Materials for

https://doi.org/10.1021/acs.chemrev.3c00408
Chem. Rev. XXXX, XXX, XXX−XXX

Direct-Current Triboelectric Nanogenerator. *Nat. Commun.* **2021**, *12*, 4686.
(261) Jiao, J.; Lu, Q.; Wang, Z.; Qin, Y.; Cao, X. Sandwich as a Triboelectric Nanogenerator. *Nano Energy* **2021**, *79*, 105411.
(262) Wang, R.; Gao, S.; Yang, Z.; Li, Y.; Chen, W.; Wu, B.; Wu, W. Engineered and Laser-Processed Chitosan Biopolymers for Sustainable and Biodegradable Triboelectric Power Generation. *Adv. Mater.* **2018**, *30*, 1706267.
(263) Wang, J.; Chen, Y.; Xu, Y.; Mu, J.; Li, J.; Nie, S.; Chen, S.; Xu, F. Sustainable Lignin-Based Electrospun Nanofibers for Enhanced Triboelectric Nanogenerators. *Sustain Energy Fuels* **2022**, *6*, 1974−1982.
(264) Wang, T.; Li, S.; Tao, X.; Yan, Q.; Wang, X.; Chen, Y.; Huang, F.; Li, H.; Chen, X.; Bian, Z. Fully Biodegradable Water-Soluble Triboelectric Nanogenerator for Human Physiological Monitoring. *Nano Energy* **2022**, *93*, 106787.
(265) Fan, F.-R.; Lin, L.; Zhu, G.; Wu, W.; Zhang, R.; Wang, Z. L. Transparent Triboelectric Nanogenerators and Self-Powered Pressure Sensors Based on Micropatterned Plastic Films. *Nano Lett.* **2012**, *12*, 3109−3114.
(266) Pu, X.; Liu, M.; Chen, X.; Sun, J.; Du, C.; Zhang, Y.; Zhai, J.; Hu, W.; Wang, Z. L. Ultrastretchable, Transparent Triboelectric Nanogenerator as Electronic Skin for Biomechanical Energy Harvesting and Tactile Sensing. *Sci. Adv.* **2017**, *3*, e1700015.
(267) Fan, F.-R.; Tian, Z.-Q.; Lin Wang, Z. Flexible Triboelectric Generator. *Nano Energy* **2012**, *1*, 328−334.
(268) Wang, Y.; Yang, Y.; Wang, Z. L. Triboelectric Nanogenerators as Flexible Power Sources. *npj Flexible Electronics* **2017**, *1*, 10.
(269) Xiao, X.; Meng, X.; Kim, D.; Jeon, S.; Park, B.; Cho, D. S.; Lee, D.; Kim, S. Ultrasound-Driven Injectable and Fully Biodegradable Triboelectric Nanogenerators. *Small Methods* **2023**, *7*, 2201350.
(270) Wang, Z. L. Triboelectric Nanogenerators as New Energy Technology for Self-Powered Systems and as Active Mechanical and Chemical Sensors. *ACS Nano* **2013**, *7*, 9533−9557.
(271) Wang, J.; Wu, C.; Dai, Y.; Zhao, Z.; Wang, A.; Zhang, T.; Wang, Z. L. Achieving Ultrahigh Triboelectric Charge Density for Efficient Energy Harvesting. *Nat. Commun.* **2017**, *8*, 88.
(272) Pan, R.; Xuan, W.; Chen, J.; Dong, S.; Jin, H.; Wang, X.; Li, H.; Luo, J. Fully Biodegradable Triboelectric Nanogenerators Based on Electrospun Polylactic Acid and Nanostructured Gelatin Films. *Nano Energy* **2018**, *45*, 193−202.
(273) Kang, M.; Bin Mohammed Khusrin, M. S.; Kim, Y.-J.; Kim, B.; Park, B. J.; Hyun, I.; Imani, I. M.; Choi, B.-O.; Kim, S.-W. Nature-Derived Highly Tribopositive κ-Carrageenan-Agar Composite-Based Fully Biodegradable Triboelectric Nanogenerators. *Nano Energy* **2022**, *100*, 107480.
(274) Kim, H.; Choi, S.; Hong, Y.; Chung, J.; Choi, J.; Choi, W.-K.; Park, I. W.; Park, S. H.; Park, H.; Chung, W.-J.; et al. Biocompatible and Biodegradable Triboelectric Nanogenerators Based on Hyaluronic Acid Hydrogel Film. *Appl. Mater. Today* **2021**, *22*, 100920.
(275) Yao, G.; Kang, L.; Li, C.; Chen, S.; Wang, Q.; Yang, J.; Long, Y.; Li, J.; Zhao, K.; Xu, W. A Self-Powered Implantable and Bioresorbable Electrostimulation Device for Biofeedback Bone Fracture Healing. *Proc. Natl. Acad. Sci. U. S. A.* **2021**, *118*, e2100772118.
(276) Lee, D.-M.; Rubab, N.; Hyun, I.; Kang, W.; Kim, Y.-J.; Kang, M.; Choi, B. O.; Kim, S.-W. Ultrasound-Mediated Triboelectric Nanogenerator for Powering on-Demand Transient Electronics. *Sci. Adv.* **2022**, *8*, eabl8423.
(277) Li, Z.; Feng, H.; Zheng, Q.; Li, H.; Zhao, C.; Ouyang, H.; Noreen, S.; Yu, M.; Su, F.; Liu, R.; et al. Photothermally Tunable Biodegradation of Implantable Triboelectric Nanogenerators for Tissue Repairing. *Nano Energy* **2018**, *54*, 390−399.
(278) Lee, J.; Cho, H. R.; Cha, G. D.; Seo, H.; Lee, S.; Park, C.-K.; Kim, J. W.; Qiao, S.; Wang, L.; Kang, D.; et al. Flexible, Sticky, and Biodegradable Wireless Device for Drug Delivery to Brain Tumors. *Nat. Commun.* **2019**, *10*, 5205.
(279) Rüegg, M.; Blum, R.; Boero, G.; Brugger, J. Biodegradable Frequency-Selective Magnesium Radio-Frequency Microresonators for Transient Biomedical Implants. *Adv. Funct Mater.* **2019**, *29*, 1903051.
(280) Guo, Q.; Koo, J.; Xie, Z.; Avila, R.; Yu, X.; Ning, X.; Zhang, H.; Liang, X.; Kim, S. B.; Yan, Y.; et al. A Bioresorbable Magnetically Coupled System for Low-Frequency Wireless Power Transfer. *Adv. Funct Mater.* **2019**, *29*, 1905451.
(281) Lu, L.; Yang, Z.; Meacham, K.; Cvetkovic, C.; Corbin, E. A.; Vázquez-Guardado, A.; Xue, M.; Yin, L.; Boroumand, J.; Pakeltis, G.; et al. Biodegradable Monocrystalline Silicon Photovoltaic Microcells as Power Supplies for Transient Biomedical Implants. *Adv. Energy Mater.* **2018**, *8*, 1703035.
(282) Dong, Q.; Chen, M.; Liu, Y.; Eickemeyer, F. T.; Zhao, W.; Dai, Z.; Yin, Y.; Jiang, C.; Feng, J.; Jin, S.; et al. Flexible Perovskite Solar Cells with Simultaneously Improved Efficiency, Operational Stability, and Mechanical Reliability. *Joule* **2021**, *5*, 1587−1601.
(283) Wu, W.; Han, X.; Li, J.; Wang, X.; Zhang, Y.; Huo, Z.; Chen, Q.; Sun, X.; Xu, Z.; Tan, Y.; et al. Ultrathin and Conformable Lead Halide Perovskite Photodetector Arrays for Potential Application in Retina-Like Vision Sensing. *Adv. Mater.* **2021**, *33*, 2006006.
(284) Hashemi, S. A.; Ramakrishna, S.; Aberle, A. G. Recent Progress in Flexible-Wearable Solar Cells for Self-Powered Electronic Devices. *Energy Environ. Sci.* **2020**, *13*, 685−743.
(285) Hwang, S.-W.; Park, G.; Cheng, H.; Song, J.-K.; Kang, S.-K.; Yin, L.; Kim, J.-H.; Omenetto, F. G.; Huang, Y.; Lee, K.-M.; et al. 25th Anniversary Article: Materials for High-Performance Biodegradable Semiconductor Devices. *Adv. Mater.* **2014**, *26*, 1992−2000.
(286) Chang, J.-K.; Chang, H.-P.; Guo, Q.; Koo, J.; Wu, C.-I.; Rogers, J. A. Biodegradable Electronic Systems in 3D, Heterogeneously Integrated Formats. *Adv. Mater.* **2018**, *30*, 1704955.
(287) Liu, Z.; Shin, J.; Bai, W.; Rogers, J. A.; Zhou, W. Integrated Bioresorbable Optical Sensor Systems for Biomedical Pressure and Temperature Monitoring. In *2019 IEEE Photonics Conference (IPC)*; IEEE, 2019; pp 1−2.
(288) Yang, S. M.; Shim, J. H.; Cho, H.; Jang, T.; Ko, G.; Shim, J.; Kim, T. H.; Zhu, J.; Park, S.; Kim, Y. S.; et al. Hetero-Integration of Silicon Nanomembranes with 2D Materials for Bioresorbable, Wireless Neurochemical System. *Adv. Mater.* **2022**, *34*, 2108203.
(289) Song, M.-K.; Namgung, S. D.; Sung, T.; Cho, A.-J.; Lee, J.; Ju, M.; Nam, K. T.; Lee, Y.-S.; Kwon, J.-Y. Physically Transient Field-Effect Transistors Based on Black Phosphorus. *ACS Appl. Mater. Interfaces* **2018**, *10*, 42630−42636.
(290) Zhang, Y.; Zhou, Z.; Fan, Z.; Zhang, S.; Zheng, F.; Liu, K.; Zhang, Y.; Shi, Z.; Chen, L.; Li, X.; et al. Self-Powered Multifunctional Transient Bioelectronics. *Small* **2018**, *14*, 1802050.
(291) Palmroth, A.; Salpavaara, T.; Lekkala, J.; Kellomäki, M. Fabrication and Characterization of a Wireless Bioresorbable Pressure Sensor. *Adv. Mater. Technol.* **2019**, *4*, 1900428.
(292) Zareei, A.; Selvamani, V.; Gopalakrishnan, S.; Kadian, S.; Maruthamuthu, M. K.; He, Z.; Nguyen, J.; Wang, H.; Rahimi, R. A Biodegradable Hybrid Micro/Nano Conductive Zinc Paste for Paper-Based Flexible Bioelectronics. *Adv. Mater. Technol.* **2022**, *7*, 2101722.
(293) Mahajan, B. K.; Ludwig, B.; Shou, W.; Yu, X.; Fregene, E.; Xu, H.; Pan, H.; Huang, X. Aerosol Printing and Photonic Sintering of Bioresorbable Zinc Nanoparticle Ink for Transient Electronics Manufacturing. *Sci. China Inform. Sci.* **2018**, *61*, 60412.
(294) Li, J.; Xu, H.; Zhang, Z.; Hao, Y.; Wang, H.; Huang, X. Anhydride-Assisted Spontaneous Room Temperature Sintering of Printed Bioresorbable Electronics. *Adv. Funct Mater.* **2020**, *30*, 1905024.
(295) Fumeaux, N.; Briand, D. Zinc Hybrid Sintering for Printed Transient Sensors and Wireless Electronics. *npj Flexible Electronics* **2023**, *7*, 14.
(296) Rivadeneyra, A.; Marín-Sánchez, A.; Wicklein, B.; Salmerón, J. F.; Castillo, E.; Bobinger, M.; Salinas-Castillo, A. Cellulose Nanofibers as Substrate for Flexible and Biodegradable Moisture Sensors. *Compos. Sci. Technol.* **2021**, *208*, 108738.
(297) Huo, W.; Li, J.; Ren, M.; Ling, W.; Xu, H.; Tee, C. A. T. H.; Huang, X. Recent Development of Bioresorbable Electronics Using Additive Manufacturing. *Curr. Opin Chem. Eng.* **2020**, *28*, 118−126.
(298) *U.S. Food and Drug Administration. Use of International Standard ISO 10993-1, "Biological Evaluation of Medical Devices, Part 1:*

https://doi.org/10.1021/acs.chemrev.3c00408
Chem. Rev. XXXX, XXX, XXX−XXX

Evaluation and Testing within a Risk Management Process; U.S. Food and Drug Administration, 2016.
(299) Wang, H.; Tian, J.; Jiang, Y.; Liu, S.; Zheng, J.; Li, N.; Wang, G.; Dong, F.; Chen, J.; Xie, Y. A 3D Biomimetic Optoelectronic Scaffold Repairs Cranial Defects. *Sci. Adv.* **2023**, *9*, eabq7750.
(300) Song, J. W.; Ryu, H.; Bai, W.; Xie, Z.; Vázquez-Guardado, A.; Nandoliya, K.; Avila, R.; Lee, G.; Song, Z.; Kim, J. Bioresorbable, Wireless, and Battery-Free System for Electrotherapy and Impedance Sensing at Wound Sites. *Sci. Adv.* **2023**, *9*, eade4687.
(301) Chin, S. Y.; Poh, Y. C.; Kohler, A.-C.; Compton, J. T.; Hsu, L. L.; Lau, K. M.; Kim, S.; Lee, B. W.; Lee, F. Y.; Sia, S. K. Additive Manufacturing of Hydrogel-Based Materials for next-Generation Implantable Medical Devices. *Sci. Robot* **2017**, *2*, eaah6451.
(302) Zhao, X.; Kim, J.; Cezar, C. A.; Huebsch, N.; Lee, K.; Bouhadir, K.; Mooney, D. J. Active Scaffolds for On-Demand Drug and Cell Delivery. *Proc. Natl. Acad. Sci. U. S. A.* **2011**, *108*, 67−72.
(303) Li, H.; Gao, F.; Wang, P.; Yin, L.; Ji, N.; Zhang, L.; Zhao, L.; Hou, G.; Lu, B.; Chen, Y.; et al. Biodegradable Flexible Electronic Device with Controlled Drug Release for Cancer Treatment. *ACS Appl. Mater. Interfaces* **2021**, *13*, 21067−21075.
(304) Park, J.; Jin, C.; Lee, S.; Kim, J.; Choi, H. Magnetically Actuated Degradable Microrobots for Actively Controlled Drug Release and Hyperthermia Therapy. *Adv. Healthc Mater.* **2019**, *8*, 1900213.
(305) Li, G.; Song, E.; Huang, G.; Guo, Q.; Ma, F.; Zhou, B.; Mei, Y. High-Temperature-Triggered Thermally Degradable Electronics Based on Flexible Silicon Nanomembranes. *Adv. Funct Mater.* **2018**, *28*, 1801448.
(306) Lee, C. H.; Jeong, J.-W.; Liu, Y.; Zhang, Y.; Shi, Y.; Kang, S.-K.; Kim, J.; Kim, J. S.; Lee, N. Y.; Kim, B. H.; et al. Materials and Wireless Microfluidic Systems for Electronics Capable of Chemical Dissolution on Demand. *Adv. Funct Mater.* **2015**, *25*, 1338−1343.
(307) Pandey, S. S.; Banerjee, N.; Xie, Y.; Mastrangelo, C. H. Self-Destructing Secured Microchips by On-Chip Triggered Energetic and Corrosive Attacks for Transient Electronics. *Adv. Mater. Technol.* **2018**, *3*, 1800044.
(308) Sim, K.; Wang, X.; Li, Y.; Linghu, C.; Gao, Y.; Song, J.; Yu, C. Destructive Electronics from Electrochemical-Mechanically Triggered Chemical Dissolution. *Journal of Micromechanics and Microengineering* **2017**, *27*, 065010.
(309) Stuart, M. A. C.; Huck, W. T. S.; Genzer, J.; Müller, M.; Ober, C.; Stamm, M.; Sukhorukov, G. B.; Szleifer, I.; Tsukruk, V. V.; Urban, M.; et al. Emerging Applications of Stimuli-Responsive Polymer Materials. *Nat. Mater.* **2010**, *9*, 101−113.
(310) Shen, Y.; Fu, X.; Fu, W.; Li, Z. Biodegradable Stimuli-Responsive Polypeptide Materials Prepared by Ring Opening Polymerization. *Chem. Soc. Rev.* **2015**, *44*, 612−622.
(311) Wang, X.; Wang, X.; Jin, S.; Muhammad, N.; Guo, Z. Stimuli-Responsive Therapeutic Metallodrugs. *Chem. Rev.* **2019**, *119*, 1138−1192.
(312) Gogurla, N.; Kim, Y.; Cho, S.; Kim, J.; Kim, S. Multifunctional and Ultrathin Electronic Tattoo for On-Skin Diagnostic and Therapeutic Applications. *Adv. Mater.* **2021**, *33*, 2008308.
(313) Zarei, M.; Lee, G.; Lee, S. G.; Cho, K. Advances in Biodegradable Electronic Skin: Material Progress and Recent Applications in Sensing, Robotics, and Human-Machine Interfaces. *Adv. Mater.* **2023**, *35*, 2203193.
(314) Elsayes, A.; Sharma, V.; Yiannacou, K.; Koivikko, A.; Rasheed, A.; Sariola, V. Plant-Based Biodegradable Capacitive Tactile Pressure Sensor Using Flexible and Transparent Leaf Skeletons as Electrodes and Flower Petal as Dielectric Layer. *Adv. Sustain Syst* **2020**, *4*, 2000056.
(315) Khalid, M. A. U.; Ali, M.; Soomro, A. M.; Kim, S. W.; Kim, H. B.; Lee, B.-G.; Choi, K. H. A Highly Sensitive Biodegradable Pressure Sensor Based on Nanofibrous Dielectric. *Sens Actuators A Phys.* **2019**, *294*, 140−147.
(316) Peng, X.; Dong, K.; Ye, C.; Jiang, Y.; Zhai, S.; Cheng, R.; Liu, D.; Gao, X.; Wang, J.; Wang, Z. L. A Breathable, Biodegradable, Antibacterial, and Self-Powered Electronic Skin Based on All-Nanofiber Triboelectric Nanogenerators. *Sci. Adv.* **2020**, *6*, eaba9624.
(317) Sun, C.; Bu, N.; Hu, X. Recent Trends in Electronic Skin for Transdermal Drug Delivery. *Intelligent Pharmacy* **2023**. DOI: 10.1016/j.ipha.2023.08.001

https://doi.org/10.1021/acs.chemrev.3c00408
Chem. Rev. XXXX, XXX, XXX−XXX